BESSY G.m.b.H. und Institut für Physik, Universität Potsdam
Arbeitsgruppe Prof. Dr. W. Gudat

Quantum-size effects in the electronic structure of novel self-organized systems with reduced dimensionality

Dissertation
zur Erlangung des akademischen Grades
"doctor rerum naturalium" (Dr. rer. nat.)
in der Wissenschaftsdisziplin Experimentalphysik

eingereicht an der
Mathematisch-Naturwissenschaftlichen Fakultät
der Universität Potsdam

von
Andrei Varykhalov

Universität Potsdam, 16 Juni, 2005

Abbreviations

ARPES angle-resolved photoelectron spectroscopy
BZ Brillouin zone
b.c.c. bulk centered cubic (crystal structure)
DOS density of states
f.c.c. face centered cubic (crystal structure)
HOMO highest occupied molecular orbital
KKR Korringa-Kohn-Rostoker approach
LCGO linear combination of Gaussian orbitals
LDOS local density of states
LDA local density approximation
LUMO lowest unoccupied molecular orbital
LEED low-energy electron diffraction
ML monolayer
PES photoelectron spectroscopy
QWS quantum-well state
RAPW relativistic augmented plane-wave
STM scanning tunneling microscopy
UHV ultra-high vacuum
XPS x-ray photoelectron spectroscopy

Symbols, units, definitions

Å Ångström = 10^{-10} m, length unit
nm nanometer = 10^{-9} m, length unit
nA nanoampere = 10^{-9} A, current unit
eV electron-volt $\sim 1.6 \cdot 10^{-19}$ J, energy unit
a (or a_0) [Å] lattice constant of a cubic crystal
$\mathbf{k}$ wave vector of the electron in the crystal
$\mathbf{k}_\parallel$, $\mathbf{k}_\perp$ components of $\mathbf{k}$ relative to the crystal surface
k, $k_\parallel$, $k_\perp$ [Å^{-1}] scalar (absolute) values of wave-vectors
$m_e \sim 9.1 \cdot 10^{-31}$ kg, mass of the free electron
m^* effective mass of the electron is the lattice
$m_\parallel^*$ in-plane effective mass of the electron
E($\mathbf{k}$) energy-momentum dispersion, band structure
E_{kin} [eV] kinetic energy of the electron
E_i [eV] electron energy in the initial state of photoemission
E_f [eV] electron energy in the final state of photoemission
E_F Fermi level, Fermi energy
V_t [V] bias voltage in STM
I_t [nA] tunneling current in STM
λ [nm] wave-length
hν ($\hbar\omega$) [eV] energy of photon
Φ [eV] work function of a solid surface
ρ(E) density of states (DOS)
ψ wave function of an electron
$M_{\nu,\mu}$ matrix element of electron transition
T(E) transition tunneling coefficient
$f(E) = \dfrac{1}{e^{\frac{E-E_F}{kT}}+1}$ Fermi-Dirac distribution

Contents

Chapter 1

Introduction

1.1 Motivation

When single atoms of one or more chemical elements assemble to form a solid, the electrons of outer shells become delocalized and may propagate over the whole lattice of the crystal. A very important characteristics is their energy-momentum dispersion $E(\mathbf{k})$ [1, 2], which defines fundamental electrical, mechanical and optical properties of a solid [3]. The typical situation in solids is that the valence band electrons form Bloch waves of sp- and d-type. In metals they are weakly bound to the lattice and can be well described in terms of the nearly free electron [1] approximation, where the function $E(\mathbf{k})$ possesses the form of a simple parabola at high-symmetry points of the Brillouin zone (Fig. 1.2(b)). The coefficient of parabolic dispersion is inversely proportional to the effective mass of the electron m^*, which reflects a moderate perturbation introduced into the Hamiltonian of the free electron by the periodic potential of the lattice. The crystal potential is also responsible for diffraction of propagating electron waves, which leads to the appearance of forbidden energy regions which separate the electron bands [4]. What makes the band structure of real solids appear considerably more complicated than Fig. 1.2(b) is the three-dimensional crystal lattice (in reciprocal space) and the non-degenerate orbitals of p- and d-electrons which contribute individual bands. This hold also for each constituent of a compound. The description of localized states requires computational approaches like the tight-binding formalism or density functional methods. Additional atomic and molecular phenomena, like spin-orbit splitting [5] as well as effects of hybridization [6] can lead to the lifting of degeneracies and in this way affect the electronic structure of the real solid.

So far the electronic properties of infinitely extended crystals are well understood experimentally and also theoretically [7], and another effect related to ultra-small crystals attracted the attention of the scientific community about three decades ago [9]. Most generally this phenomenon can be described as quantization of the spectrum of trapped electrons into discrete energy levels, when the dimensions of the potential well are comparable with the wave-length of the electron. Concerning the novelty of the effects, one has to admit that the theoretical

background has already been developed at the early ages of quantum physics. For instance, the classical solution of the particle-in-a-box problem can be found in any textbook on wave mechanics. A sketch is shown in Fig. 1.1. If an electron is placed into a one-dimensional potential box with infinitely high walls, boundary conditions define the allowed wave vectors as $k = \frac{n\pi}{d}$, where n and d are the quantum number and the width of the well, respectively, the solution of the stationary Schrödinger equation gives the wave-functions as $\psi \sim sin(\frac{\pi n z}{d})$, while allowed energy levels are $E_k = \frac{\hbar^2 k^2}{2m} = \frac{\hbar^2}{2m}(\frac{\pi n}{d})^2$. Such states are known as *quantum well states* (QWS). There is a certain analogy with electronic states of the inner atomic shells, since the electrons are confined there in the three-dimensional Coulomb well of the nucleus. However, we use the term QWS only for confinement and quantization of free electrons and weakly bound valence band electrons. The first theoretical work on QWS's in thin metal films was published in 1983 [10], while the experimental observation of QWS with photoemission was reported in 1985 for the first time [11].
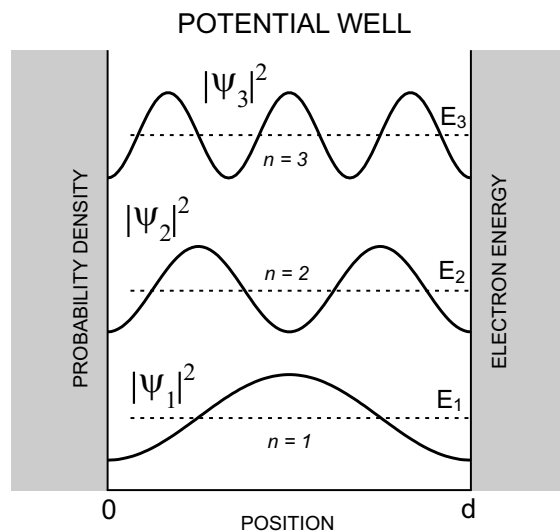
Figure 1.1: Solution of particle-in-a-box problem in one-dimensional potential box with infinitely high walls. Allowed electron energies (dashed lines, axis to the right) and the probability density $\mid \psi_m \mid^2$ (solid lines, axis to the left) are shown. ψ_m is the electron's wave-function.

In the last couple of years, physics of QWS's received renewed attention. The general tendency to miniaturization and acceleration of the speed of integrated circuits has pushed the design of microelectronic devices into the nm-range [14, 15, 16]. Such advance makes the consideration of quantum-size effect in the electronic components unavoidable. For instance, if one forms an ultra-thin film of nm-thickness (as shown in Fig. 1.2(a)) restricting the crystal in one coordinate, a standing electron wave can appear in the film leading to energy-momentum quantization in the electronic structure (Fig. 1.2(c)). The conductivity of such film should be strongly affected by the reduced dimension and will exhibit oscillatory behavior in the voltage-current characteristics [9]. Further restrictions of size lead to

nanostructures of even lower dimensionality, like nanowires or quantum dots (Fig. 1.2(a)). Since the electron in such structures will be confined by several coordinates, there appear additional boundary conditions for the Schrödinger equation and quantization effects become obviously more complicated.
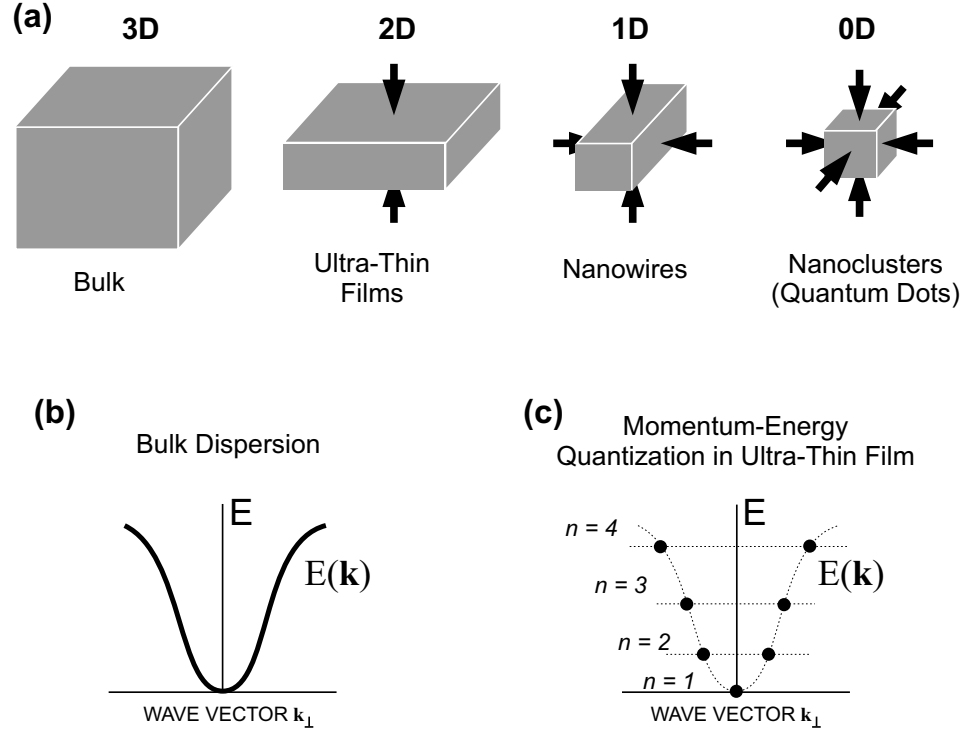
Figure 1.2: (a) nanostructures of different dimensionality; (b) energy-momentum dispersion $E(\mathbf{k})$ in nearly free electron solid (energy gaps are not shown for simplicity); (c) size restrictions lead to quantization of $E(\mathbf{k})$ which appears as a discrete set of allowed momentum-energy points.

One must admit that in experiments the ideal nanostructures shown in Fig. 1.2(a) can hardly be produced and investigated. Whichever it is, thin films, nanowires or quantum clusters, they are typically prepared and measured on a substrate. In turn, the substrate may significantly influence the electronic properties of nanostructures. One extremely important factor for quantization is the presence of appropriate energy gaps in the substrate. If no gap is provided the electron can extend more deeply through the interface into the solid with the result that reflection and confinement are weak or absent, as the space-energy diagram in Fig. 1.3(a) shows . That means that QWS's should particularly appear in the energy range covered by the substrate gap. In many studies wide gap semiconductors were considered as ideal templates for QWS systems [11]. The situation with metallic substrates is less obvious since in metals conductance and valence bands are overlapping. The impression that quantization in metal-on-metal systems is not possible is, however, wrong. Metallic substrates can exhibit so called *relative* gaps [77], which can appear in the band structure projected on a particular crys-

tallographic surface, as illustrated in Fig. 1.3(b). Such relative gaps may even derive face-specific surface states. A particular case is the hybridization gap [78]: if two bands of the substrate have the same energy and symmetry, they hybridize causing the development of an additional energy gap. In these gaps the interfacial electron reflectivity can increase which can lead to electron confinement as shown in Fig. 1.3(a).
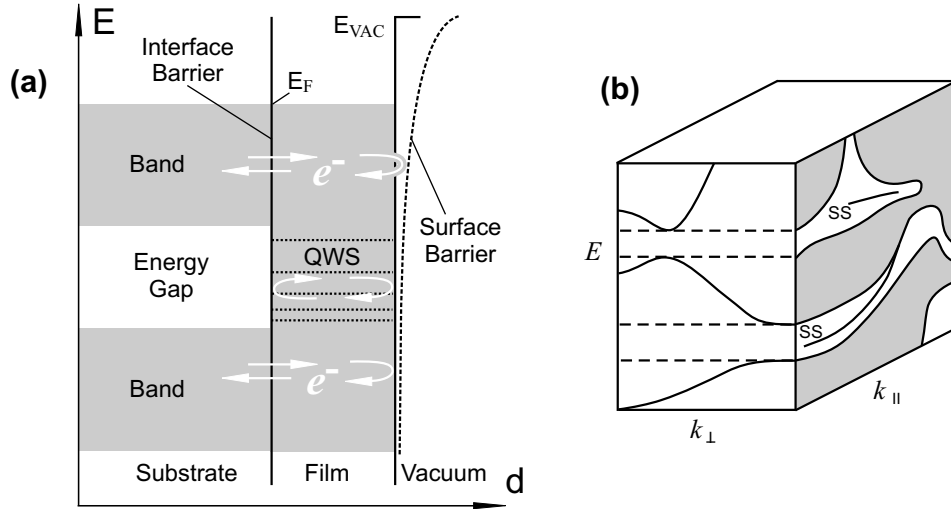
Figure 1.3: (a) The space-energy diagram illustrates the formation of quantum well states in thin film; (b) projection of the bulk band structure on the surface yields relative energy gaps. Dispersions of surface states SS are also shown. From Ref. [94]

Generally, the substrate is crucially important not only for supplying quantization conditions, but for the formation of nanostructures itself. It can serve as a template for preparation of regular arrays of nanowires, nanostripes or quantum dots employing effects of *self-organization*. In solid state physics the term "self-organization" can be defined as formation of atomic systems with periodic structural and electronic properties under the influence of thermodynamic factors and interatomic interactions. For example, vicinal to low-Miller-index face surfaces (stepped surfaces) has been used as templates for preparation of nanostripes with tailored electronic [129, 130] and magnetic [139] properties. Also surface reconstructions can be applied to control the formation of nanoclusters or quantum wires [17, 18, 19]. Since self-organization can provide periodic and almost infinite (the overall area is only limited by the dimensions of the sample) nanostructure, application of methods which measure a spatially averaged signal (as photoelectron spectroscopy does) becomes possible.

The present Thesis focuses on quantum size-effects in metallic nanostructures. All aforementioned aspects, including quantum-well states in thin films, self- or-

ganization and one-dimensional quantization at stepped surfaces and large-scale reconstructions are the topics covered by this work.

The Thesis has the following structure: after experimental aspects and methodical background (Chapter 1) QWS's in ultra-thin films of Ag on Ni(111) are reported (Chapter 2). Ag/Ni(111) is a complex case where electron confinement is achieved both due to a relative gap and because of the increased reflectivity due to reduced interfacial hybridization between the bands of Ag and Ni. It will also be demonstrated how the electronic structure of the substrate can be probed by quantum well states.

Chapter 3 is fully devoted to stepped W surfaces. Firstly, specific effects in the final state of photoemission are reported. Important implications for understanding self-organized nanostructures and their electronic properties are discussed. In the second part of Chapter 3 a report on novel effects of self-organization on the steps of vicinal W is presented. The described method produces nanostructures which involve Au-W surface alloying and demonstrate unique effects of lateral quantization in the valence band.

The last chapter, Chapter 4, deals with the large-scale carbon reconstruction R(15×3) on W(110) [224]. This template itself exhibits quantum-size effects in the surface electronic structure and also controls self-organization phenomena, like self-assembly of Au nanowires with distinct lateral quantum well states. In the last section it is shown that W(110)/C-R(15×3) can also support the arrangement of molecules, and the discovery of self-assembly of fullerene nanoclusters with magic numbers is reported.

The methods of choice in this work are photoelectron spectroscopy (PES) and scanning tunneling microscopy (STM). PES [20, 21] is a powerful and widely applied technique for studies of the electronic structure of solids. The photoemission process involves the excitation of an electron followed by its escape into vacuum and it becomes possible to study the electronic structure of solids by analyzing the energy distribution of photoemitted electrons. The application of synchrotron radiation, where the photon energy $h\nu$ can be continuously varied extends the method significantly. The combination of $h\nu$-dependent with angle resolved photoemission measurements makes it possible to achieve a complete characterization of the electronic structure and obtain energy band dispersions $E(\mathbf{k})$.

One shall keep in mind that electronic properties of crystals are related to their atomic structure. In particular, if one deals with low-dimensional systems, precise information on their geometry can be crucially important for understanding electronic effects. STM is perfectly suited for the investigation of the atomic geometry of surfaces. It is a local probe method, which achieves unprecedented spatial resolution down to one Å. All systems of reduced dimensionality studied in this work were verified with STM.

Since design, building, tuning and commissioning of the STM set-up used in the experiments required a considerable amount of time, experimental aspects of STM measurements will be described to greater detail.

The chapters of this Thesis are organized and written in such a way that they are self-contained to large extent. It is thus possible to read every individual Chapter

without the need to access the others (with the exception of the Experimental part which is useful for understanding technical aspects of this work). Although, a large amount of experimental results is presented, the author wants to apologize for not being able to present all aspects of the addressed subjects to greater detail due to strict requirements for the length of the Thesis at Universität Potsdam.

1.2 Methodical background

1.2.1 Technique of Photoemission

Phenomenologically, the description of the photoemission technique is rather simple. When a solid surface is irradiated by monochromatic light of energy $\hbar\omega$, photoexcitation of electrons in the crystal can occur. If the kinetic energy of excited electron is high enough, it can overcome a surface potential Φ and escape to vacuum. Φ is called work function. It depends on material and crystallographic face and has typically a value of several electronvolt (eV). The extended equation of the photoeffect provides the kinetic energy of the photoelectron

$$E_{kin} = \hbar\omega - \Phi - \mid E_B \mid \tag{1.1}$$

and can be used to determine its binding energy E_B in the solid. The photoemission process is sketched in Fig. 1.4(a), where excitation of electrons from the valence band and a core-level is shown. Binding energies of valence electrons are typically around several eV, those for core levels range from tens to thousands. It is evident from equation (1.1), that E_B can be measured by counting the energy distribution of the electrons emitted into vacuum, since this distribution corresponds loosely speaking to the density of occupied states in the solid [20].

Photoemission is generally considered in the framework of the so called *three step model* [20]. This model defines three stages which are treated independently. The first step i.e. the photoexcitation itself, should be considered in the framework of quantum mechanics. In terms of the single-particle approximation [20], the excitation of an electron is an optical transition from an occupied initial eigenstate $\mid \psi_i >$ to a final state $\mid \psi_f >$. The transition rate between the eigenstates is given by Fermi's golden rule:

$$P_{fi} = \frac{2\pi}{\hbar} \mid < \psi_i \mid H' \mid \psi_f >\mid^2 \delta(E_f - E_i - \hbar\omega) \tag{1.2}$$

Here the δ-function is responsible for the conservation of energy while H' denotes the Hamiltonian of the interaction between electron and vector potential $\mathbf{A}$ of the photon. Assuming $\mathbf{A}$ to be constant one gains in the dipole approximation:

$$H' = \frac{e}{2mc}\mathbf{A} \cdot \mathbf{p} \tag{1.3}$$

Inserting H' into eq. (1.2), and comparing the result with the ordinary Hamiltonian of the electron $H = \frac{p^2}{2m} + V(\mathbf{r})$ [22] one gains two forms of the matrix element:

$$< \psi_f \mid \mathbf{p} \mid \psi_i >= im\omega < \psi_f \mid \mathbf{r} \mid \psi_i >= \frac{i}{\omega} < \psi_f \mid \nabla V \mid \psi_i > \tag{1.4}$$
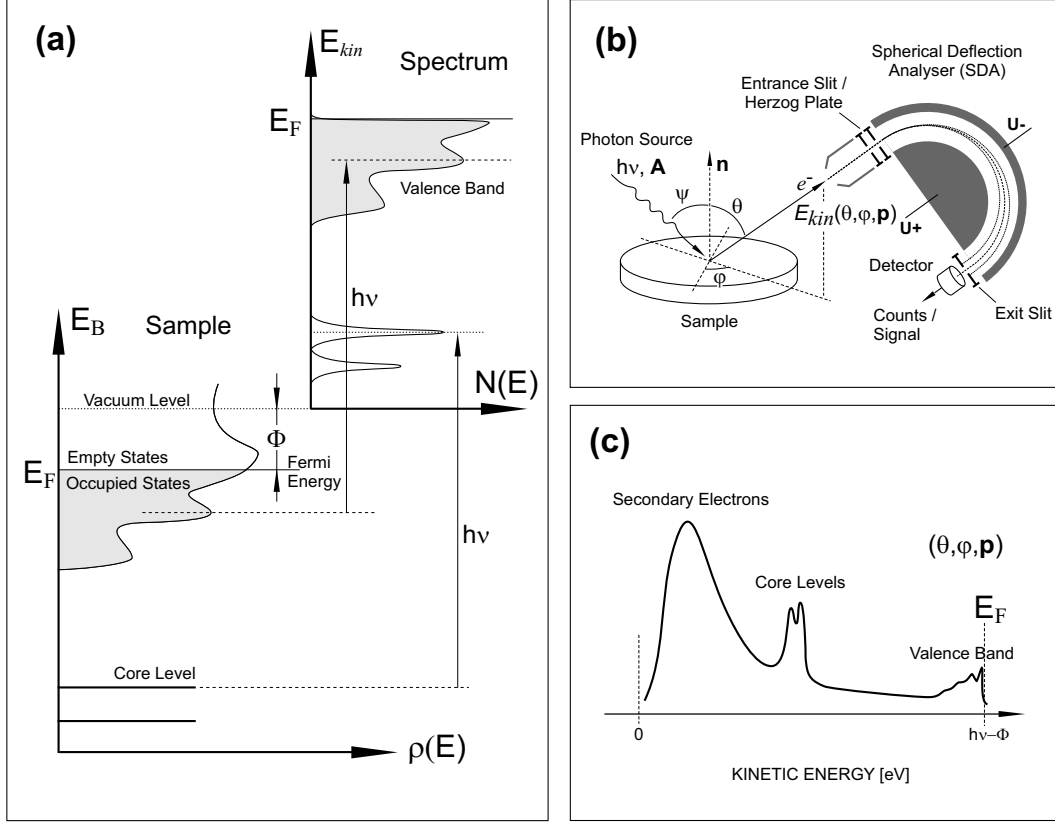
Figure 1.4: (a) energy diagram illustrating the photoexcitations with monochromatized light; (b) scheme of photoemission experiment; (c) shape of detected photoelectron spectrum.

Since the second expression includes the gradient of V it comes out that photoemission cannot take place when the potential $V(\mathbf{r})=0$. This is a particularly important point, which means that a free electron cannot perform photoemission and that the final state of photoemission is explicitly supplied by the potential of the lattice or atoms. In terms of momentum-energy dispersions, the final state of a photoexcited electron with low kinetic energy is defined by the band structure of the solid [78], while for relatively high energies, $E(\mathbf{k})$ can always be approximated by a free electron parabola [20].

The second stage of the three step model is electron transport to the surface. The probing depth of photoemission is limited by effects of inelastic electron scattering. The number of excited electrons which can traverse a film of thickness d and escape to vacuum depends exponentially on d:

$$(1.5) \qquad\qquad N = N_0 e^{-\frac{d}{\lambda}}$$

where λ is the inelastic mean free path which is given by the empirical formula [23]:

$$(1.6) \qquad\qquad\qquad \lambda = 0.41 a^{3/2} \sqrt{E_{kin}}$$

Here a is expressed in nm and denotes the lattice constant of the film. E_{kin} should be set in eV. Evaluating expression (1.6) shows that photoemission is a very surface sensitive technique. Even at kinetic energies of several hundred eV, the inelastic mean free path corresponds to the first few atomic layers. The same effect of inelastic scattering causes a huge tailed background of secondary electrons in the photoelectron spectra (Fig. 1.4(c)). Such background makes the detection of electrons with very low kinetic energies explicitly difficult.

The third stage in the three step model is the escape of the photoelectron through the surface barrier. The understanding of this process is crucial for the determination of the dispersions E($\mathbf{k}$). Since the photon has negligible momentum in the vacuum ultraviolet energy range, the simplest view of photoemission considers only direct (optical) transitions in the first stage of the three step model. It means that the photoexcited electron acquires kinetic energy but practically no extra momentum so that its wave vector $\mathbf{k}$ is conserved, as illustrated in Fig. 1.5(a) where transitions for two photon energies $h\nu_1$ and $h\nu_2$ are sketched in a momentum-energy diagram. The momentum vector of the electron which propagates inside the crystal can evidently be determined according to $\mathbf{k}^{int} = \mathbf{k}_{\parallel}^{int} + \mathbf{k}_{\perp}^{int}$, where $\mathbf{k}_{\parallel}^{int}$ denotes the projection parallel and $\mathbf{k}_{\perp}^{int}$ perpendicular to the surface (Fig. 1.5(b)). When the electron traverses a potential barrier at the surface it experiences refraction as shown in Fig. 1.5(b). Only the component $\mathbf{k}_{\parallel}^{int}$ is preserved, although it can be translated by a reciprocal surface lattice vector $\mathbf{G}$ i.e. $\mathbf{k}_{\parallel}^{ext} = \mathbf{k}_{\parallel}^{int} + \mathbf{G}$. Such refraction means that the emitted electron will propagate in a new direction described by the angle θ (Fig. 1.5(b)). Combining basic energy-momentum relation $E_{kin} = \frac{\mathbf{k}^2}{2m}$ and simple trigonometry $\mid \mathbf{k}_{\parallel} \mid = \mid \mathbf{k} \mid \cdot sin(\theta)$ one gains an expression for the parallel component of the wave vector:

$$(1.7) \qquad\qquad \mid \mathbf{k}_{\parallel}^{ext} \mid = \mid \mathbf{k}_{\parallel}^{int} \mid = \sqrt{\frac{2m}{\hbar^2} E_{kin}} \cdot sin(\theta)$$

This is important for the concept of *angle-resolved* photoemission. The scheme of the experiment is shown in Fig. 1.4(b). If one collects electrons photoemitted in a certain direction θ and measures their kinetic energy, then the $\mathbf{k}_{\parallel}^{int}$ component of the wave vector can easily be calculated from eq. (1.7). The electron energy distributions measured for each polar angle θ provide the band structure E($\mathbf{k}_{\parallel}$).

The situation with the perpendicular component of momentum is, however, more complicated. Upon refraction this vector is reduced due to the work function
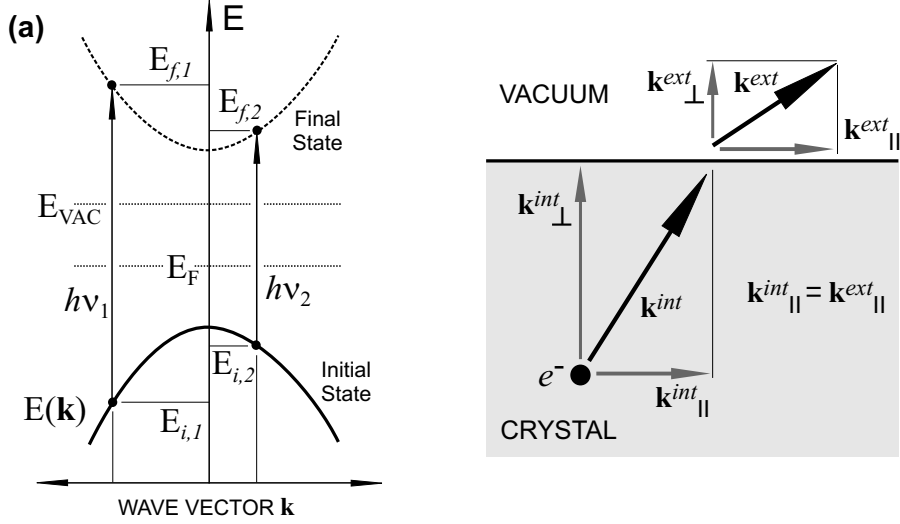
Figure 1.5: (a) momentum-energy diagram showing optical (direct) electron transitions for two different photon energies; (b) refraction of a photoelectron at the surface barrier upon escape from the crystal.

of the sample so that $\mathbf{k}_\perp^{ext}$ does not directly reflect the value of $\mathbf{k}_\perp^{int}$. It can be determined only approximately using the formula [12]:

$$(1.8) \qquad \mathbf{k}_\perp^{int} = \sqrt{(\mathbf{k}_\perp^{ext})^2 + \frac{2mV_0}{\hbar^2}}$$

where the inner potential V_0 is an empirically adjustable parameter.

To extend the description of the method, another aspect of photoelectron spectroscopy i.e. *photon-energy dependent* photoemission must be mentioned. This technique is illustrated in Fig. 1.5(a). Variation of the photon energy $h\nu$ will cause electron excitation in different $\mathbf{k}$-points of the Brillouin zone if $\mathbf{k}_\parallel$=0 is chosen. This happens due to the different dispersions of initial- and final-state bands with $\mathbf{k}_\perp$, and because of energy conservation (eq. (1.2)). If one measures $h\nu$-dependent photoemission normal to the surface direction (and knows the dispersion of the final-state), the dispersion $E(\mathbf{k}_\perp)$ in the initial state can easily be obtained along the surface normal.

It is necessary to note, that in photoemission phenomena occur which directly show that a single-particle picture is inappropriate. These are so called *correlation effects* which are caused by interaction between the excited electron and the remaining electrons. They require a more general consideration and cannot be described in the framework of the three-step model. Correlation phenomena include, in particular, plasmons and electron-hole pair excitations [24]. While the former phenomenon originates from collective oscillations in the gas of nearly free valence electrons, the latter is related to the finite lifetime of the photohole and its screening by other valence electrons. Such correlation effects cause a number of characteristic features in measured spectra (satellites, line broadening and asym-

16

metry, energy shifts) and must be considered in the interpretation of experimental data.

A possible description of the many body effects in photoemission is given in the framework of the *sudden approximation* [13]. It is assumed that a photoelectron is suddenly created and decoupled from the remaining (N-1) electrons. The (N-1) electron state created as a result can be described as $a_k \mid \psi_{N,0} >$, where a_k is an operator which annihilates an electron with wave vector k. $a_k \mid \psi_{N,0} >$ is not an eigenstate of the Hamiltonian $H_0^{(N-1)}$ of the (N-1) remaining electrons. The spectrum is then obtained as projection of this frozen state $a_k \mid \psi_{N,0} >$ onto the fully relaxed eigenstates $\mid \psi_{(N-1),0} >$.

The photoelectron spectrum can then be written in a useful form which allows to use in Fermi's golden rule the single particle spectral density function $A(\omega)$ instead of the δ-function: [13]:

$$(1.9) \qquad\qquad p_{i,f} = \frac{2\pi}{\hbar} \mid M_{i,f} \mid^2 \cdot A(\omega)$$

where $\omega = E_f - \hbar\omega$. The processes which are responsible for the line broadening and the energy shifts due to coupling between the photohole and the rest of the electron system are described in terms of the complex self-energy operator $\Sigma(\omega)$ [13]. In the solid $A(\omega)$ represents the spectral function of the hole state and can be expressed in terms of the self-energy operator:

$$(1.10) \qquad\qquad A(\omega) = \frac{1}{\pi} \frac{\mid Im\Sigma(\omega) \mid}{\mid \omega - E_i - Re\Sigma(\omega) \mid^2 + \mid Im\Sigma(\omega) \mid^2}$$

This function has a maximum for $\omega = E_i - Re\Sigma(\omega)$. If this equation has more than one solution, the solutions are divided up into main lines and satellites. Speaking more generally, there is no matter how complicated the physical system is; in the framework of the described model of sudden approximation the photoelectron spectrum can always be interpreted in terms of transitions from the initial state to all possible final states.

In this Thesis it is particularly important to mention many body effects in photoemission since this topic is of concern for Chapter 2, where we will discuss the determination of the electronic structure of Ni (Ni is $3d$ transition metal with a highly correlated system of d-electrons). If we leave correlation effects aside, another advantage over the three step model is that the sudden approximation also describes photoemission from surface states, which repeatedly appear in the experiments performed in the present Thesis. Moreover, this model accounts for effects of photoelectron diffraction in the final state of photoemission from surface resonances (see Chapter 3, Chapter 4).

Experimentally, electron energy spectra are measured with electrostatic analyzers [20]. A typical example of a hemispherical device is shown in Fig. 1.4(b). The electrons emitted into vacuum pass through the entrance slit (which provides angular resolution) and propagate further between two charged metallic hemispheres.

The electric field between the spheres refracts the electrons and only those with a particular kinetic energy pass. By changing the voltage on the spheres one can tune this pass energy, which defines the energy resolution together with exit slits at the end of the analyser. The electrons are counted by secondary electron amplifiers, known also as channeltron detectors [25]. A spectrum is measured by applying a ramp voltage to the Herzog plate (Fig. 1.4(b)) which decelerates the electrons to the constant pass energy. As a source of monochromatic light an X-ray tube, gas discharge lamp, laser, or synchrotron source are typically used. For $h\nu$-dependent photoemission the synchrotron radiation [8] is very important, since it is the most efficient source with a wide and continuous spectrum in the vacuum ultraviolet range.

1.2.2 Technique of STM

Let us consider two metallic electrodes which are brought sufficiently close to each other. When the separation is around several Å, a so called tunneling current appears. Tunneling is purely a quantum effect, related to the finite value of the electron wave function. In the case of a small distance between metallic electrodes an electron can overcome the potential barrier (even if its energy is not sufficient) and jump from one electrode directly to the other without being emitted into vacuum. When the electrodes are connected, the tunneling currents are negligible, since Fermi energies E_F are equalized and there are no empty states to which the electrons can be transferred. However, if one applies a voltage V_t between the electrodes, the situation changes. A bias V_t will shift E_F causing predominant tunneling from occupied states of one electrode to the empty states of the other. There appears a minor but detectable current I_t, which is typically in the nA range. The direction of the tunneling depends obviously on the polarity of the applied bias voltage. This effect is illustrated in Fig. 1.6(a), where the band structure of both electrodes is sketched for $V_t=0$ and for $V_t > 0$ as well.

The simplest theoretical description of tunneling phenomena is given in the framework of a model with one-dimensional rectangular barrier (solid lines in Fig. 1.6(a)). In this approach the electron transmission coefficient has a simple analytical form $T \sim e^{-\frac{2d}{\hbar} \cdot \sqrt{2m(U_0 - E)}}$ [5], where d denotes the barrier width, and the potential U_0 its height. When a low bias voltage V_t is assumed, the tunneling current is expressed by the formula [26]:

$$(1.11) \qquad I_t = (\frac{e}{\hbar})^2 \cdot \frac{V_t}{d} \cdot \sqrt{2m_e \overline{\Phi}} \cdot e^{-Ad\sqrt{\overline{\Phi}}}$$

Here $A \sim \frac{4\pi\sqrt{2m_e}}{\hbar}$, and $\overline{\Phi}$ is the average work function of both electrodes and has a typical value of several eV. Eq. (1.11) reveals that the tunneling current I_t will be altered by three orders of magnitude when d is changed by 2.5 Å (height of a monoatomic step). Such strong dependence of I_t from the width of barrier is at the core of the STM principle.

Scanning tunneling microscopy has been invented by Binnig and Rohrer [27, 29] in 1982 as a tool for recording the surface topography of conducting samples [30]. In the STM the first electrode is the sample and the second one a very sharp tip with apex radius of several hundred Å. The tip scans the sample at fixed bias V_t, while a feedback circuit holds the current I_t constant by adjusting the height of the tip (i.e. barrier d).

In this regime (regime of constant current) the tip "glides" over the surface at almost constant distance. The scheme of the experiment is shown in Fig. 1.6(b). The trajectory of tip apex (dashed contour) reflects the surface corrugation. As $x-, y-$ and $z-$ movers, piezo-ceramic elements are used. When an electric field is applied, polarized ceramics of high quality can provide retractions of several tenths of Å providing unprecedented precision of tip positioning. The correction voltage on the z-piezo (V_{Pz} in Fig. 1.6(b)) is supplied by a feedback circuit and
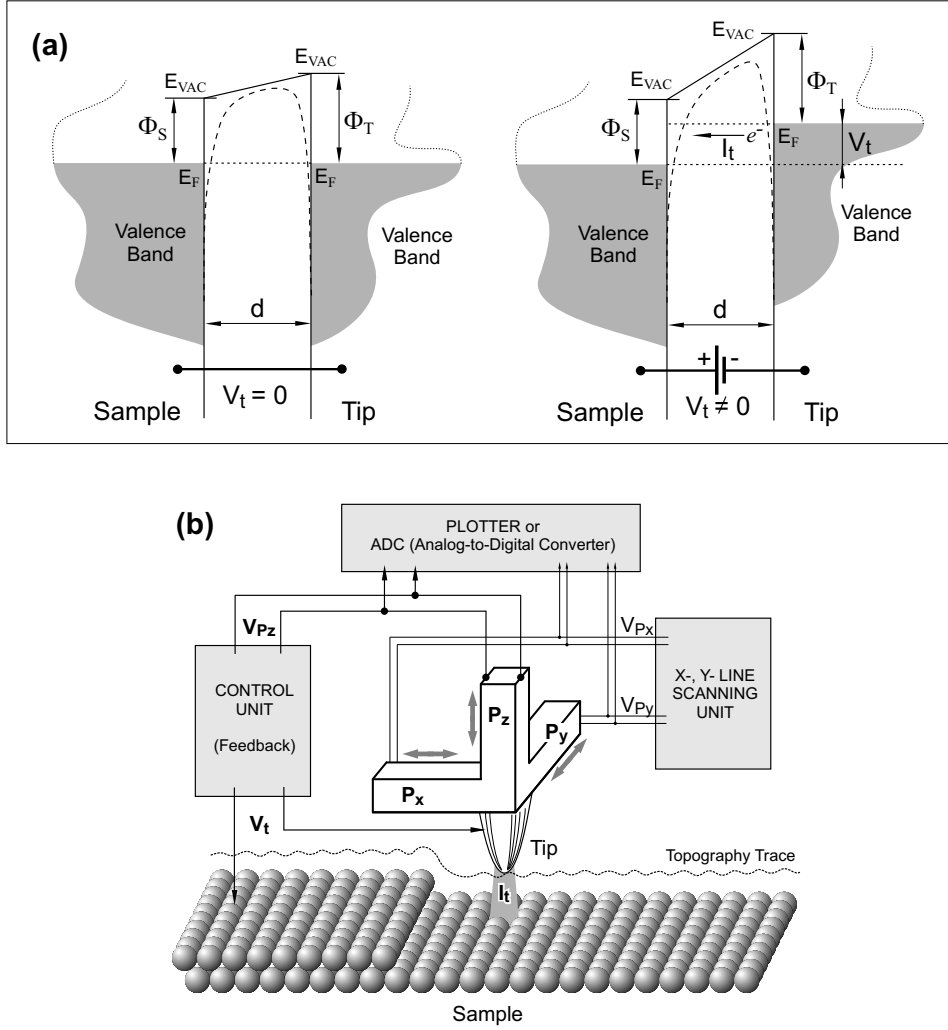
Figure 1.6: STM principle: (a) tunneling phenomena in the approach of a flat rectangular barrier (solid lines). A more realistic model should also consider mirror image potentials (dashed line); (b) functionality and block-scheme of STM.

repeats the corrugation of the sample surface. Therefore, this voltage is recorded as the desired topographic signal in combination with x- and y- voltages of scanning (V_{Px} and V_{Py} in Fig. 1.6(b)). The STM resolution in the direction normal to the surface depends only on the ability of the electronics to correctly measure the tunneling current and to control the z-position of the tip. Lateral resolution, however, depends on several other factors, like electronic structure of the sample, electronic properties and geometry of the tip [31, 32, 33, 34, 35].

Shortly after its invention, STM has demonstrated the ability to image surfaces with atomic resolution [28]. As to the interpretation, such images cannot be simply assigned to the topography, due to the evident importance of local electronic structure of sample and tip. They require a more accurate description in terms of quantum mechanics. The STM theory which explained the origin of atomic resolution was developed by Tersoff and Hamann [34, 35] with the approximation of a

spherical tip apex, and later advanced by Chen [32]. Since for typical conditions of tunneling the tip-surface interaction is small, perturbation theory can be applied leading to the following expression for the current [35]:

$$(1.12) \qquad I_t = \frac{2\pi e}{\hbar} \sum_{\mu,\nu} f(E_\mu) \cdot (1 - f(E_\nu + eV_t)) \cdot \mid M_{\mu,\nu} \mid^2 \delta(E_\mu - E_\nu)$$

where $f(E)$ is Fermi function and $M_{\mu,\nu} = \frac{\hbar^2}{2m} \int d\mathbf{S} \cdot (\psi_\mu^* \vec{\nabla} \psi_\nu - \psi_\nu^* \vec{\nabla} \psi_\mu)$ is the matrix element of the tunneling operator between eigenstates of tip $\mid \psi_\mu >$ and surface $\mid \psi_\nu >$ with energies E_μ and E_ν, respectively [36]. If the electronic structure of the tip is described using a basis of spherical functions, the bias voltage V_t is assumed to be low and room temperature is considered (so that eq. (1.12) gains no term for reverse tunneling) one gains [35]:

$$(1.13) \qquad I_t \sim V_t \cdot \phi^2 \cdot \rho_{tip}(E_f) \cdot R^2 \cdot k^{-4} \cdot e^{2kR} \sum_\nu \mid \psi_\nu(\mathbf{r_0}) \mid^2 \delta(E_\nu - E_f)$$

where $k = \frac{\sqrt{2m_e\phi}}{\hbar}$ and r_0 means the coordinate vector of the tip apex sphere. In expression (1.13) ϕ denotes the work function of the sample, R - radius of the spherical apex and $\rho_{tip}(E_f)$ - the density of states (DOS) at the Fermi level in the tip. As the density of states can be expressed in terms of the wave-functions as $\rho(\mathbf{r_0}, E_f) = \sum_\nu \mid \psi_\nu(\mathbf{r_0}) \mid^2 \delta(E_\nu - E_f)$ eq. (1.13) is transformed to:

$$(1.14) \qquad I_t \sim V_t \cdot R^2 \cdot \rho(\mathbf{r_0}, E_f)$$

This is a particularly important formula because it demonstrates that at fixed bias voltage and fixed current the STM tip traces a contour of constant density of states in front of the sample at the Fermi level. In other words, STM rather images the spatial distribution of DOS than a real topography. In the case of metals they are largely the same since electrons of the valence band are delocalized and the local DOS is equal to full charge density [35, 37, 38, 39].

With semiconductors the situation is much more complicated because the function $\rho(\mathbf{r_0}, E)$ has a strong dependence on energy and a more general formula must be used [40]:

$$(1.15) \qquad I_t \sim \int_{E_f}^{E_f+eV_t} \rho(r_0, E) \cdot T(E, V_t) dE$$

Here, $T(E, V_t)$ denotes the coefficient of electron transmission through the tunneling barrier. In semiconducting crystals some states may even be localized on particular atoms or bonds. In this case STM images can be very far from the real topography. One distinct example of such system is GaAs(110) [41]. Here, the

21

maxima of occupied DOS are localized on atomic sites of As, while unoccupied states are concentrated on Ga atoms. Thus, scanning with positive polarity, where tunneling takes place from the tip to empty states of the sample, reveals only the sublattice of Ga. At reverse voltage STM shows accordingly only atoms of As [41].

A final remark should be made on tip preparations. The geometry is very important and it is clear that a perfect tip is considered to have one (or few) atoms at the apex in order to provide extreme resolution. There is a variety of preparation techniques - they will be mentioned later in the description of experimental aspects. For the moment, some important comments on electronic properties of the tip should be given. Chen established theoretically the fundamental limit of STM resolution in 1990 [32]. In particular, he predicted that lateral atomic resolution can only be achieved if tip wave-functions which participate in tunneling are sufficiently localized. He has shown that the resolution of a tip which is made of a metal with large contribution of sp-states in the valence band is limited to 10-12 Å. In order to achieve an atomically resolved image the tip material should be either a d-band metal or certain semiconductor. The most standard tip materials used nowadays for high-resolution STM imaging are W and Pt.

1.2.3 LEED

LEED (low energy electron diffraction) is another powerful method of surface characterization. If a monoenergetic electron plane wave undergoes scattering at a periodic atomic structure (Fig. 1.7(a)), the conditions for constructive interference are given by the Bragg equation [42]:

$$(1.16) \qquad\qquad \Delta\lambda = a \cdot sin(\theta) = n \cdot \lambda$$

As the wave length of the electron λ is in the LEED energy range of the same order of magnitude as typical lattice constants a, diffraction maxima of elastically scattered electrons will be resolved easily because of significant angular separation (θ). Since LEED is a diffraction technique (an opposed to STM), it provides the surface geometry in reciprocal space and therefore is perfectly suited for verification of ordered periodic atomic structures.
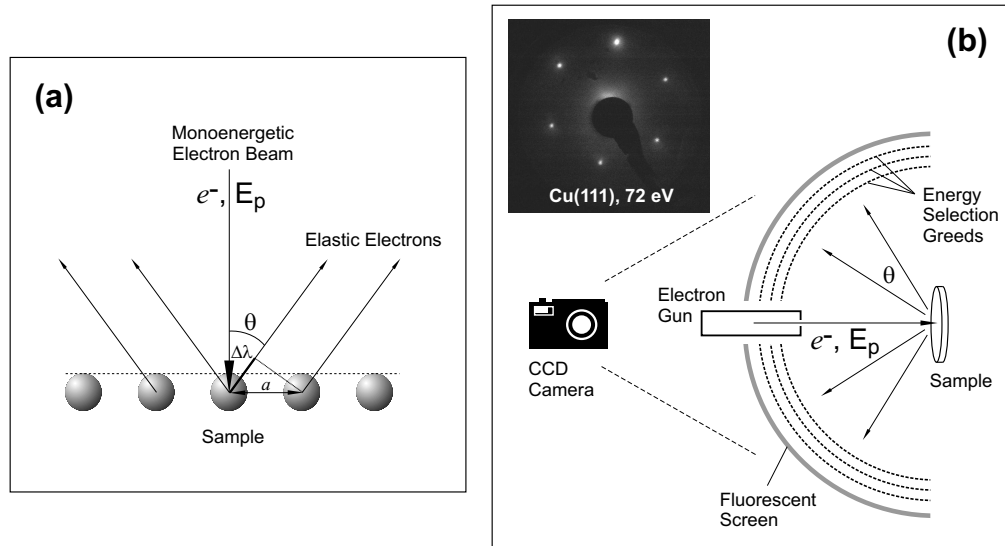
Figure 1.7: (a) low energy electron diffraction from atomic structures in Bragg formalism; (b) scheme of LEED analyzer and the LEED pattern obtained from Cu(111) with an electron beam of 72 eV.

The scheme of a LEED analyser is shown in Fig. 1.7(b). The electron gun irradiates the sample in normal incidence. Backscattered electrons are filtered by hemispherical retarding grids in order to cut the inelastic background. The elastic electrons are further accelerated towards the fluorescent screen and their angular distribution is photographically recorded. For example, the LEED pattern obtained from the Cu(111) surface is shown in the inset to Fig 1.7(b).

1.3 Experimental systems

1.3.1 Photoemission set-up

A scheme of the experimental set-up, where the PES measurements have been performed is presented in Fig. 1.8. This is an ultra-high vacuum (UHV) chamber equipped with a hemispherical electron analyzer VG ESCALab, the ultimate angle and energy resolutions of which are 1° and 10 meV, respectively. Typical base pressure in this chamber during experiments is 2×10^{-10} mbar, which is enough to keep even reactive sample surfaces clean for several hours. BESSY [44] synchrotron radiations from different beamlines was used as a source of monochromatic linearly polarized light with variable photon energy.
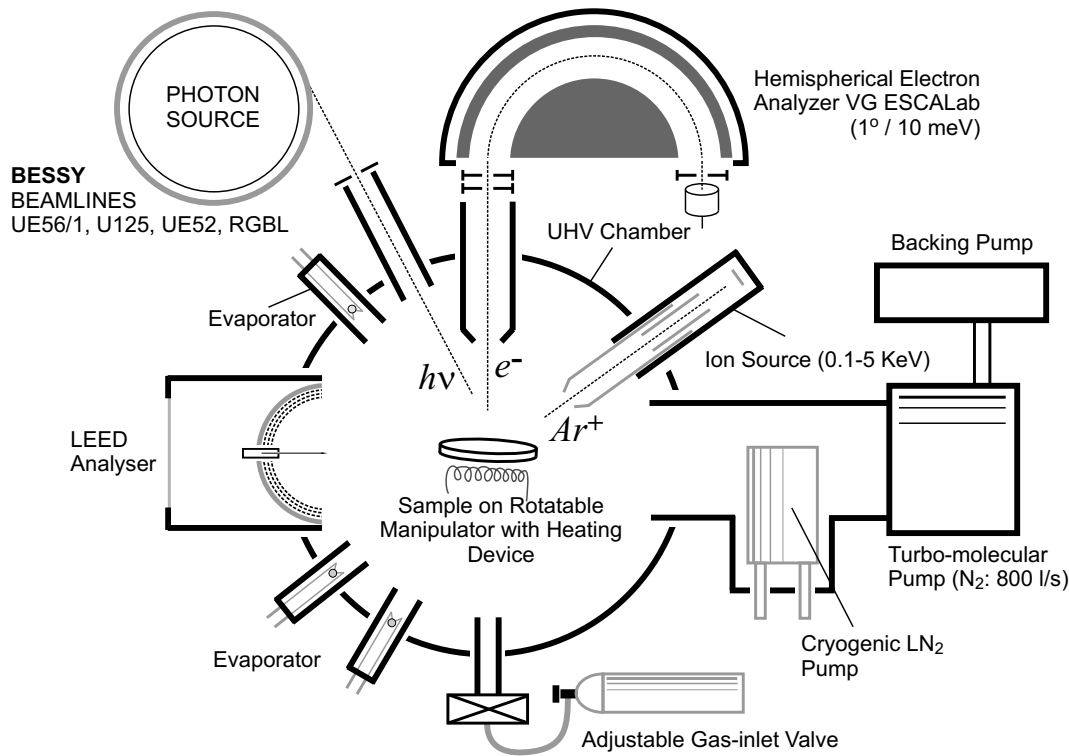
Figure 1.8: Scheme of photoemission chamber "HiRes" at BESSY.

The chamber is equipped with a LEED analyser which is used to prove surface cleanliness and its geometry. Since STM measurements are performed in a separate chamber, LEED patterns are also used as "fingerprints" which guarantee compliance between the samples measured by PES and by STM. The PES chamber is additionally equipped with an ion gun which can be used for sample sputtering for surface cleaning and a precision leak valve which allows the controlled inlet of noble sputter gases into the chamber. This set-up has also a number of evaporators, which are used for preparation of epitaxial metal overlayers. Materials were either evaporated form a melted drop on a tungsten filament or from a wire heated by

24

electron bombardment.

The sample is mounted on a rotatable manipulator which allows to change the angle of photoemission seen by the analyzer. There is also a heating device on a manipulator, which allows to heat the sample to highest temperature by electron bombardment. Measurements of photoelectron spectra were performed at room temperature.

1.3.2 STM set-up

An important part of this work was an implementation of the STM technique, which provided valuable information on the geometry of the nanostructures studied with PES. The scanning tunneling microscope used in the experiments was an Omicron VT SPM [46]. The work reported in this Thesis includes design and construction of the UHV chamber. A scheme of the developed set-up is presented in Fig. 1.9. The installation consists of two chambers (for sample preparation and for measurements, see photo in Fig. 1.10(a)). The preparation chamber can either be equipped with LEED for preliminary control of the surface geometry or with a cylindrical mirror analyzer which allows the analysis of surface chemistry with Auger spectroscopy. It has also a system of evaporators, including one which can be exchanged without breaking of vacuum conditions. In addition, there are a sputter gun which is used for the cleaning of samples and STM tips, and a high temperature heater stage for flashing them. In contrast to the PES installation, in the STM set-up the sample has always to be transferred between preparation devices and two chambers, therefore an efficient system of transfer is required. So called wobble-sticks or mechanical hands [47] adapted for Omicron sample holders were used. When *in situ* preparation is completed the sample is transferred into the measuring chamber through a rotatable carousel mounted between the chambers and accessible by both manipulators (Fig. 1.9).

Since the tip-surface separation in STM is only a few Å, a proper vibration isolation [43] is required for successful experiments. Although the Omicron VT SPM has an efficient internal eddy current damping stage (which is a ring of copper brackets in the field of permanent magnets) with a resonance frequency of about 2 Hz, an extra vibration control has been implemented. In particular, the whole set-up was installed on pneumatic dampers [48] (Fig. 1.10(b)). Coefficients of vertical and horizontal transmissibility [48] are presented in Fig. 1.10(c) and (d), respectively. As one can see, both resonance frequencies are less than 1 Hz, which provides reliable isolation from typical floor vibrations originated from surrounding pumps and industrial machines (4-20 Hz). In order to avoid internal vibrations a specific pumping system had to be implemented. Since typical turbo pumps vibrate at frequencies of about hundreds Hz and with an amplitude no less than 1 μm, no mechanical pumps should be running during the measurements. Therefore, the vacuum system of STM was developed in such a way that turbo pumps could be powered down and the chamber pumped only with ion-pump and cryogenic trap as shown in Fig. 1.9. The achieved working pressure of the STM chamber is below 1×10^{-10} mbar.
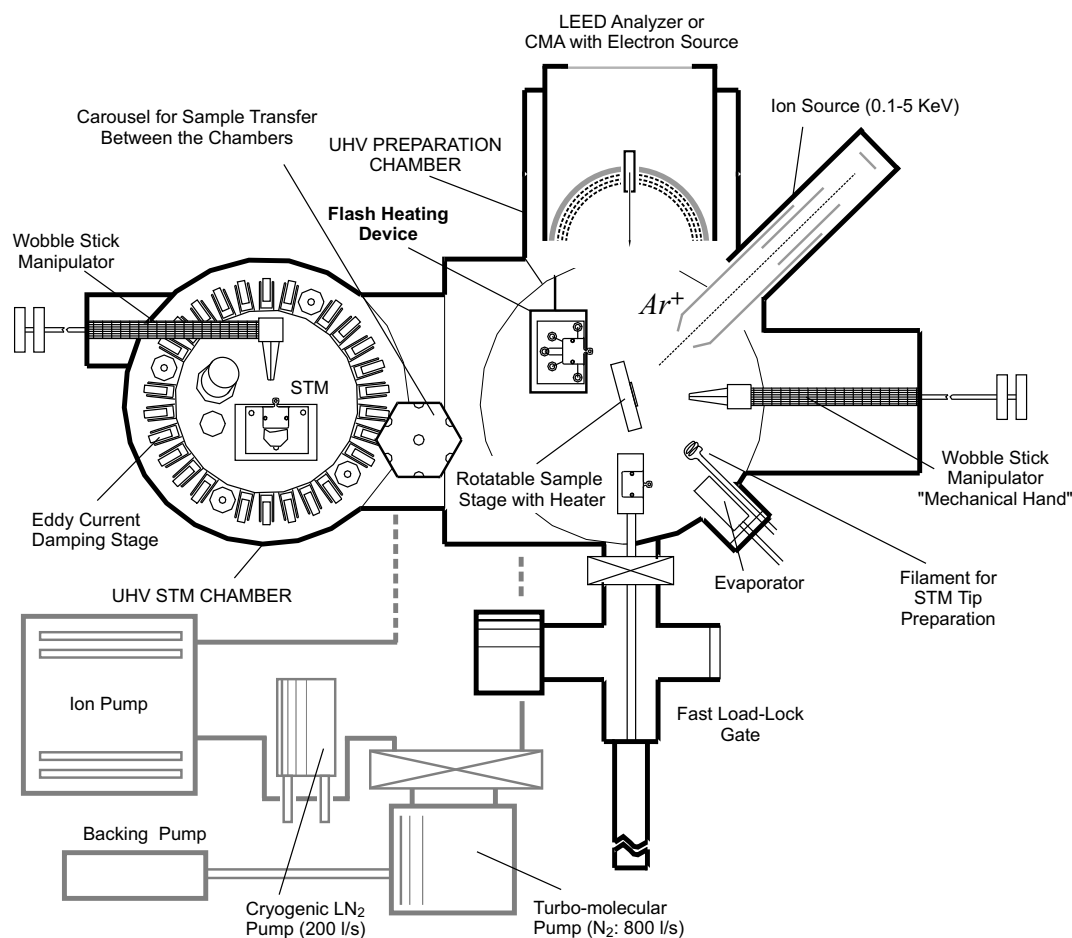
Figure 1.9: Vacuum scheme of STM set-up at BESSY.

Special attention has to be paid to the methods of tip preparation. Although general techniques are known [232], in every particular case it remains a challenging point to produce a high-resolution sharp tip with a stable signal. A multiple stage preparation procedure has been developed. Initially, W (99.995 %) wire was electrochemically etched in a 20% solution of NaOH. Since the wire diameter is only about 0.4 mm, surface tension drives the etching so that the end of a tip gains a pronounced V-shape (Fig. 1.11(a)). Although such tip is sharp (the apex diameter is about 100 Å) it is covered by a ~ 50Å thick layer of oxide and alkali residuals [232]. The successive stage of cleaning takes place *in situ* in the vacuum chamber. The tip is sputtered with high energy (4 keV) Ar^+ ions with a focusing negative voltage -800 V applied to the apex. Then it is shortly flashed up to 1600 °C by electron bombardment in order to remove residual oxygen and, afterwards, sharpened by autoemission at 3500 V.

The drastic improvement in the tip quality is confirmed by results presented in Fig. 1.11 where STM imaging of graphite with "as etched" (b) and *in situ* treated (c) tips is reported. Less noise and increased lateral resolution are evident in the
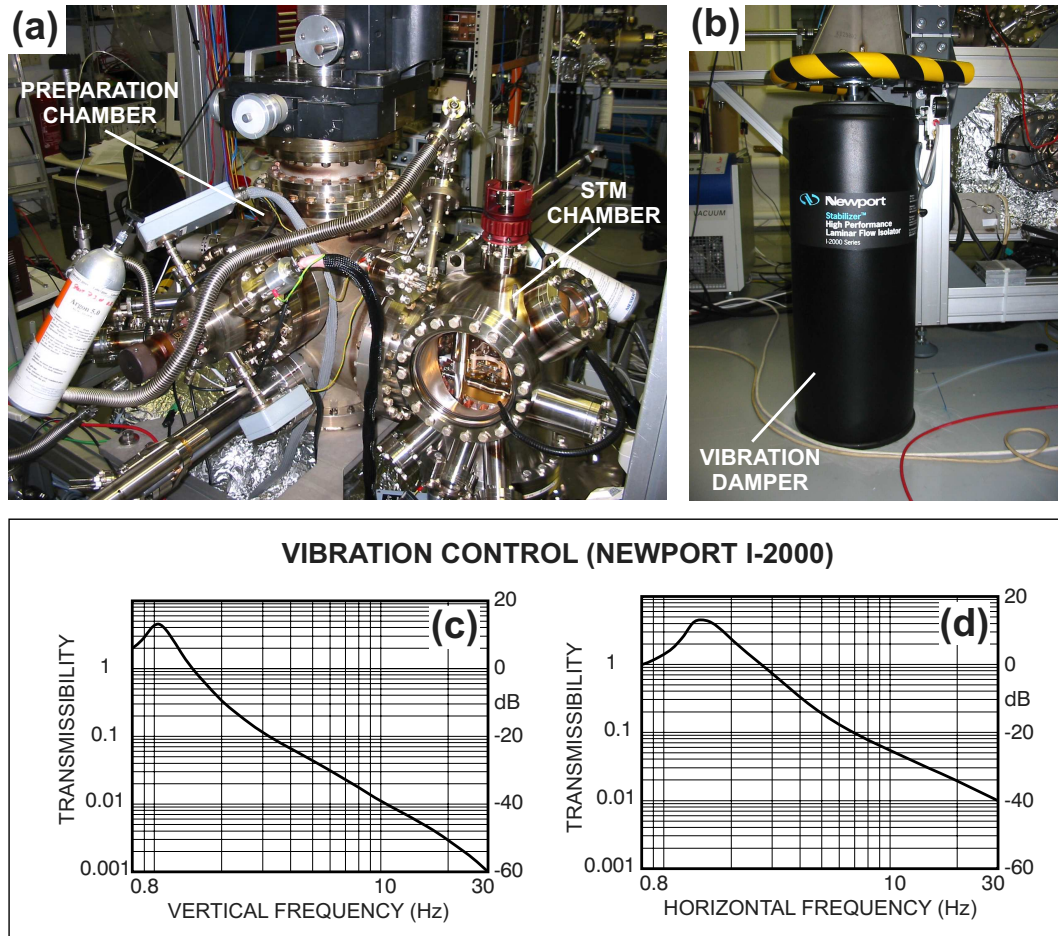
26

Figure 1.10: (a) photo of the STM installation developed at BESSY; (b) photo of pneumatic column Newport I-2000; (c) vertical and (d) horizontal transmission coefficients of I-2000 vibration dampers [48].

second case.

An important part of the STM chamber is the so called fast load-lock system (Fig. 1.9), which allows to introduce new samples into the chamber in less than 2 hours. This option is particularly significant with respect to STM functionality. Since preparation of a good tip is not always reproducible and tip crashes are quite common, an STM installation must have the possibility of fast tip exchange without venting the chamber.

Another interesting technical feature of the set-up is the "flash" heating device. From the very beginning of chamber design, it was considered to conduct experiments with W crystals. There is a number of experimental difficulties related to tungsten. The main point is that a W sample must be heated to 2000°C and above in order to achieve an atomically clean surface. This is hardly compatible with STM, where the sample should always be fixed on a transferable sample holder. Also, the mounting must be reliable in order to avoid mechanical instabilities. Reliable mounting, in turn, means proper thermal contact. So, if flashing
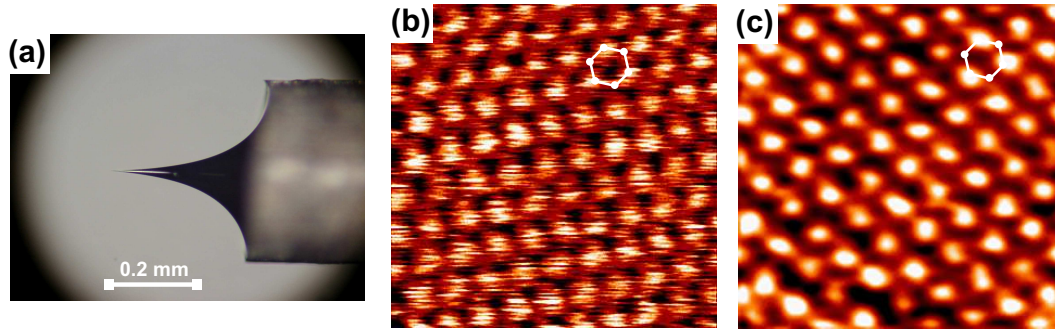
Figure 1.11: (a) tip prepared by electrochemical etching in alkali solution (the photo was made through an optical microscope); (b) STM commissioning: 25Å × 25Å atomically resolved image of graphite (HOPG), recorded with "as etched" W tip without *in situ* treatment; (c) STM image of graphite obtained with a sputtered and annealed tip.

is performed in the slot of any standard design, the vacuum conditions will be strongly affected at high temperatures because of a thermal desorption. With respect to this a new concept was introduced, which is illustrated in Fig. 1.12(a).
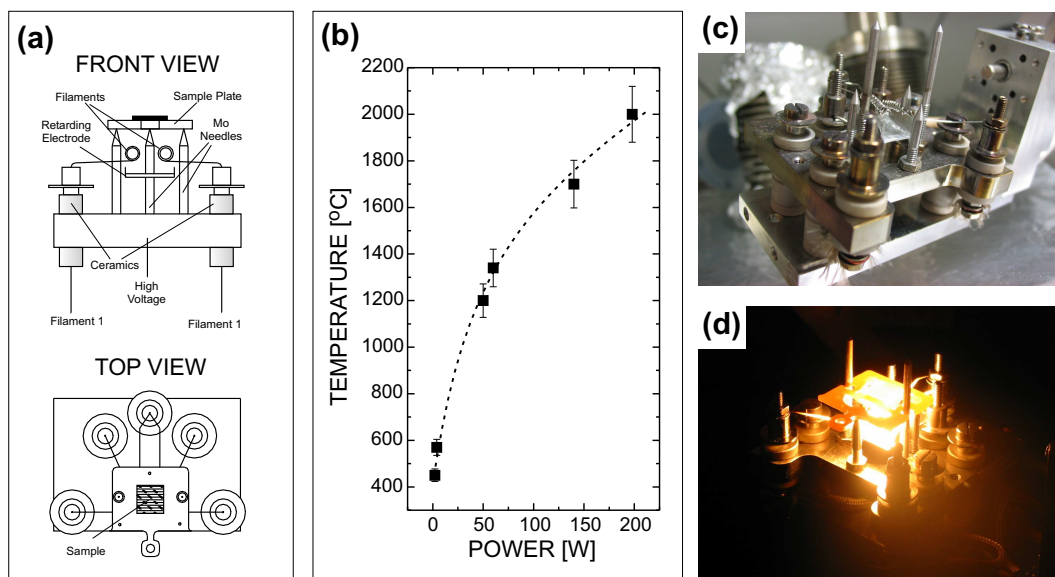
Figure 1.12: (a) technical design of "flash" heating device; (b) temperature-power calibration; (c) photo of heater stage; (d) heater stage in vacuum chamber used in the experiment.

It was decided to flash the sample together with the sample holder which is made of Mo or W. In order to minimize transmission of heat to surrounding parts, the sample plate is placed on three Mo needles (while another two [not shown] pass through the plate and insure it from accidental loss). The plate and the sample are maintained at high positive voltage (up to 1.2 kV) and heated by electron

28

bombardment from filaments underneath. The sample plate can easily be placed on such heater with standard wobble-stick manipulators. A temperature-power calibration of this device is given in Fig. 1.12(b), while photos of it are shown in Fig. 1.12(c) and (d). The heater has demonstrated excellent characteristics keeping the base pressure during the flash below 2×10^{-9} mbar. This device allows preparation of perfectly clean W surfaces and to study them with STM.

Finally, one more technical outcome of the present work can be mentioned. From the very beginning it was necessary to achieve compatibility between PES and STM experiments. Thus, when the STM chamber was under construction, the whole system of sample transfer and manipulation in the photoemission chamber "HiRes" was redesigned and one compatible with STM implemented. This work has supplied the possibility to transfer prepared samples between both chambers under UHV conditions using a permanently pumped "suitcase".

Chapter 2

Quantum-Well States in Ultra-Thin Metallic Films

Electron confinement by a potential well in low-dimensional structures has been a hot topic of research for the last twenty years. The following Chapter is devoted to the investigation of quantum-well states in two-dimensional films. In particular, the observation of energy levels of electrons confined in Ag overlayers prepared on Ni(111) are reported. Properties of this quantum-well system will be extensively studied as a function of thickness of the epitaxial film, while its band dispersions are investigated by angle-dependent photoemission. The phase accumulation model, which is an advanced tool for analysis of quantum-size effects, will be applied for description. It will also be shown how a careful analysis of the quantum-well electronic structure can reveal the ground state electronic properties of the substrate, which in this case were an intriguing point for many decades due to strong correlation effects in the valence electron system of Ni. Results of such indirect probing will be compared to the electronic structure of Ni obtained theoretically using LDA methods as well to the one measured directly in photoemission experiments. Conclusions lend credit to the simplest view of photoemission from Ni, assigning some early observed contradictions between theory and experiments to many electron effects in the final state of photoemission.

2.1 Ground state of a correlated electron system probed by quantum well states: Ag/Ni(111)

2.1.1 Introduction

As it was already mentioned, E(**k**) band dispersions are very important for the understanding of many fundamental properties of crystals. The application of density functional theory and the local density approximation (LDA) has contributed numerous calculations of band dispersions for solids, surfaces, and thin films. Experimentally, the dispersion relations of occupied electronic states have been measured by angle-resolved photoelectron spectroscopy [20, 21]. One of the first metals where a systematic comparison was undertaken between theory and experiment is Cu. The comparison revealed quantitative agreement between the predictions for the ground state and the dispersions obtained from the excitation spectra in the experiment [49, 50]. For other metals, the comparison resulted in at least fair agreement but Ni represents an exception to the rule in several respects. It shows features which are not described by LDA calculations, like photoemission satellites in core-level spectra [51] and in the valence band [52, 53]. Also, the experimentally measured width of the occupied d-band was found to be significantly smaller than predicted by theory [54, 55, 56, 57]. Meanwhile, theory has concentrated on incorporating correlation effects and reproduced the experimental findings including the satellite and the band narrowing [58, 59, 60, 61, 62]. Up to the present, the effects of electron correlation on photoemission spectra of Ni metal have remained an intriguing point and challenging subject for experiment [53, 63, 64, 65, 66, 67, 68] and theory [69, 60, 70, 71, 61, 62, 72]. However, it has never been attempted to determine the occupied Ni electronic structure in the ground state by experiment. It is indeed possible to probe the Ni electronic structure and *not excite* the Ni electrons if electrons scattered off a Ni crystal are analyzed. In this way, unoccupied states of Ni up to 30 eV above the Fermi level were determined in a low-energy electron reflection experiment [73].

In the following, a method for indirect experimental determination of the Ni(111) electronic structure in its ground state is reported. The problem is solved by analysis of quantum-well states in epitaxial overlayers on top of Ni. In order to be sensitive to electron correlation in occupied Ni d-states, two provisions have to be made: (i) Ni scattering conditions are probed in the coherent scattering regime. To this end, Ni forms the boundary of a metallic quantum-well where coherent scattering at the surface and the metal-metal interface leads to the formation of standing electron waves. The electronic structure of Ni determines then the phase shift of the electrons scattered at the interface, and the energy dependence of the phase shift determines, in turn, the quantum-well energies; (ii) the electrons occupying quantum-well states are probed by angle-resolved photoemission. The feasibility of this method has already been demonstrated for sp electrons in Ag and Al films probing the interfaces Ag/Cu(111) [74] and, in particular, Al/Si(111) [75], and Ag/Si(100) [76] for which the strong modification of the dispersions of quantum

well states with $\mathbf{k}_\parallel$ was demonstrated.

The quantum-well states of ultra-thin Ag layers on Ni(111) with thicknesses from 0 to 15 monoatomic layers (ML) are reported below. The electronic structure of Ag is perfectly suited for the formation of quantum-well states [77, 78] since it has only a simple Bloch-type sp-band dispersing along [111] from 0.3 eV down to 4 eV binding energy below which in addition Ag d-states contribute. This range fully covers the predicted Ni band gap along [111], the upper border of which is defined by the bottom (minimum energy $\Lambda_1^{\min}$) of the d band with Λ_1 symmetry. The dispersion of this band is precisely known from several independent photoemission experiments and LDA calculations. Λ_1 originates at Γ_{25}' for which energies as different as $\sim$2.15 eV or $\sim$1.2 eV were given (the average of majority and minority spin values is used here). The former value was obtained by Moruzzi et al. using the Korringa-Kohn-Rostoker approach (KKR)[7] and by Wang et al. using the method of linear combination of Gaussian orbitals (LCGO) [79]. The latter energy is measured experimentally by angle-resolved photoemission [57, 55]. For $\Lambda_1^{\min}$ the corresponding values are 2.69 eV from theory and 1.7 eV from experiment. The deviation by 1 eV is typical of the strongly correlated electronic structure of Ni [80] and allows for a clear statement to be expected from the present experiment: Is the ground state of Ni appropriately described by conventional LDA theory and the shift by 1 eV fully due to the final state of photoemission or needs strong electron correlation to be incorporated to describe the ground state?

2.1.2 Experimental details

Experiments were done at the VUV-beamline at Elettra [45], and the Russian-German beamline at BESSY [85, 84]. The geometry used in the angle resolved photoemission experiment was such that the light had mixed s- and p-polarization. Measurements at the VUV-beamline have been performed with an Omicron electron analyser with combined 50 meV energy and 1° angle resolutions. At BESSY the hemispherical analyzer VG ESCALab was used at similar parameters. The Ni(111) surface was prepared in a standard way by multiple cycles of sputtering with 1.2 keV Ar$^+$ followed by annealing at 550°C. The good structural quality of the surface has been controlled by the presence of a sharp p(1×1) pattern in the low energy electron diffraction (LEED) (Fig. 2.1(a)). Photoemission from the Ni valence band had also been used to verify the surface cleanliness (note the Ni satellite instead of O2p at 6 eV in Fig. 2.2(b)). Base pressure in the experiments was below 2×10^{-10} mbar.

Ag has been evaporated either from a ceramic crucible or from a drop, melted on a resistively heated tungsten filament. Ag used to be deposited on Ni(111) at 80K as well as at room temperature. It was found that well-ordered overlayers with pronounced confined electron states can be prepared either by deposition at 80K and successive annealing at 600K, or by deposition at 300K but at very low deposition rate ($\sim$0.05ML/min). One has to note that preparation of the monocrystalline epitaxial overlayers of Ag on Ni(111) is a rather complicated task. Ag has an f.c.c. (face centered cubic) crystal structure (the same as Ni) and

grows on Ni(111) also with the (111)-face. The LEED pattern in the monolayer range shows a reconstruction, because of the stress induced by the large mismatch ($\sim$16%) between the lattice constants of Ni ($a = 3.517$ Å) and Ag ($a = 4.078$ Å).

The LEED pattern of 14ML Ag grown on Ni(111) at room temperature (Fig. 2.1(b)) proves the high structural quality of the epitaxial film. In order to obtain the detailed thickness-dependent electronic structure of silver film, photoemission spectra of Ag/Ni(111) were taken continuously every 2 minutes during 5 hours of deposition.

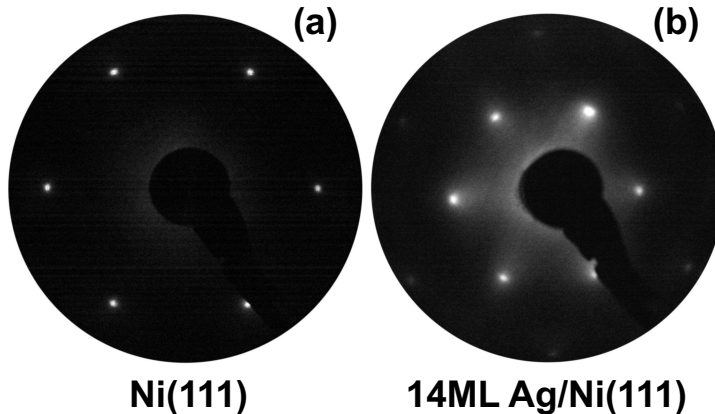**(a)**   **(b)**

Ni(111)   **14ML Ag/Ni(111)**

Figure 2.1: (a) LEED pattern of Ni(111) taken at an energy of the incident electron beam of 78 eV; (b) LEED pattern of 14ML Ag(111)/Ni(111) measured at 125 eV.

2.1.3   Results

Thickness-dependent electronic structure

In order to probe how the phase shifts of Ag electrons backscattered at the film-to-substrate interface affect the sequence of the QWS energy levels, thickness-dependent measurements have been performed. Wide-range PES spectra of the clean Ni(111) and of 14ML Ag on top, which were taken before and after the deposition series are given in Fig. 2.2(b). The intermediate spectra recorded during deposition are presented in Fig. 2.2(a). The curves are scaled in such a way as to pronounce the peaks of confined electronic states. Characteristic peaks of the QWS's are marked by thin solid lines. In Fig. 2.2(a) one can clearly see the development of the QWS electronic structure of the Ag $sp(\Lambda_6)$-band upon increasing the thickness of the overlayer (details of the band structure of Ag and Ni can be found in Fig. 2.5(b,c) where the bulk dispersions along the [111] (ΓL) direction of bulk Brillouin zone (BZ) are shown). A first, although not strongly pronounced QWS peak appears at a binding energy of $\sim$3.5 eV and corresponds to the completion of the first monolayer of Ag. Further, upon development of the second monolayer, the intensity of this peak vanishes with a QWS peak evolving at $\sim$2.7eV. Careful analysis of the peak intensity allows us to distinguish discrete levels of confined electron states up to 10 ML. This calibration can easily be extrapolated to higher

coverages providing an absolute scale for the thickness. An exact presentation of the data is given on the diagram in Fig. 2.3, where experimentally measured binding energies of quantum well states are plotted versus thickness of the Ag overlayer. Open circles denote experimental data; their diameters reflect the peak intensity. As one can see in Fig. 2.2(a), the first QWS peak evolves with increasing thickness towards the Fermi level developing a continuous branch marked as sp_1. At 14 ML it gains ∼0.5 eV binding energy almost reaching the top of the Ag sp-band. At 4 ML of Ag there appears a new QWS branch (sp_2) again at 3.5 eV which corresponds to a standing electron wave with the half wave length of sp_1. Upon expansion of the adlayer thickness this branch repeats the behavior of sp_1 shifting towards the Fermi level. All in all, it is possible to resolve the development of four similar QWS branches sp_{1-4}. Note that QWS's appear in a wide region of binding energies up to the very top of the Ag sp-band, and outside of the Ni(111)-surface-projected (relative) gap. Such behavior suggest that the electron reflectivity outside of the gap is substantial due to weak interfacial hybridization between the electronic states of Ag and Ni in a wide energy range [77].
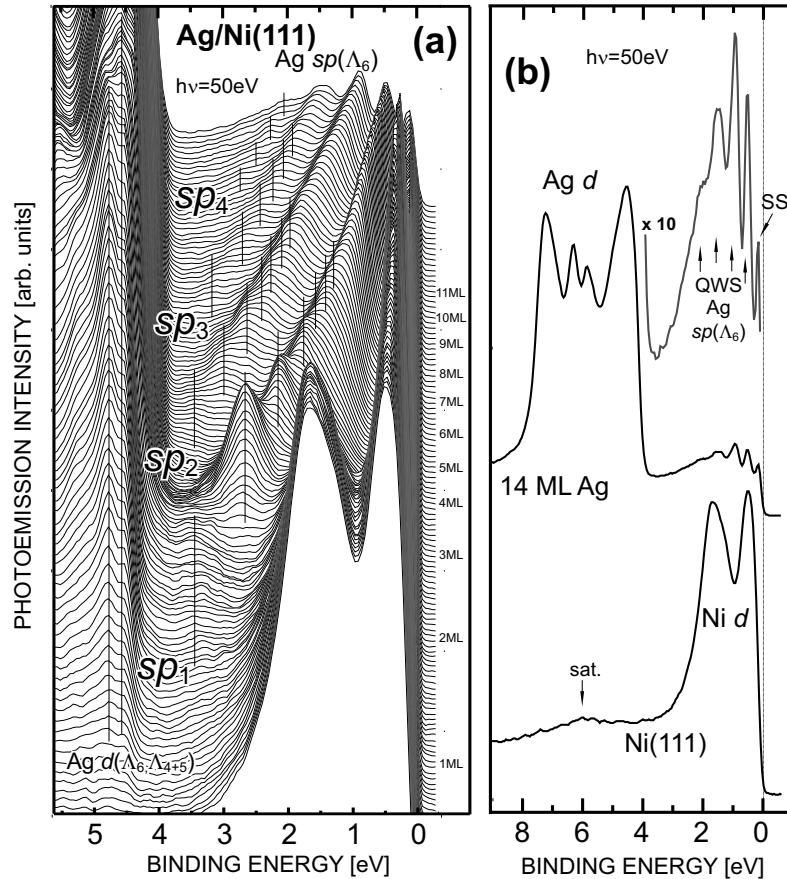

Figure 2.2: (a) development of sp- and d-QWS's in a Ag overlayer on Ni(111) measured by photoemission upon increasing the thickness of the Ag film up to 14 monolayers; (b) wide range reference photoelectron spectra of clean Ni(111) and of the 14ML-thick Ag film grown on top.

It is necessary to note the appearance of quantum well peaks at 4.0 – 5.0 eV, the binding energy of which does not change with the film thickness. They are detectable at low thickness (Figs. 2.2 and 2.3) and above 4ML are replaced by the bulk electronic structure of Ag (so that they are not observed any more). They are distinct QWS's of d-type and originate from the Λ_{4+5} bulk band of Ag.

Angle-dependent photoemission

In several works it was shown that electron reflection in the energy range of a relative gap of the substrate can lead to changes of the backscattered phase different from those for reflection outside the gap. In this case, QWS energy dispersions E(**k**) may show jumps at values of the **k**-vector which correspond to the gap edges. Such gap-related phase shifts have indeed been observed. For example, the jumps were detected in the dispersions of QWS in Ag and Al on semiconductor substrates at certain $\mathbf{k}_{\parallel}$ [75, 76, 90]. In order to test the band structure E($\mathbf{k}_{\parallel}$) of Ag on Ni(111) the angle-dependent photoemission from QWS in a Ag overlayer of different thickness has been probed. Results for an 11 ML film measured in the $\overline{\Gamma M}$ direction of the surface BZ (Fig. 2.4(d)) are reported in Fig. 2.4(a). A pronounced peak of the Ag L-gap centered surface state (SS) at $\overline{\Gamma}$ at ~ 90 meV binding energy manifests the uniformity of the overlayer and a high quality of the surface. Extracted QWS dispersions are plotted in Fig. 2.4(b).

2.1.4 Discussion

The KKR calculated surface-projected gap [79] is shown as gray area in Fig. 2.4(b). Since the experimentally measured gap is situated at 1 eV lower binding energy it comes out that even a most careful analysis *does not* reveal any shifts of in the measured dispersions as a function of the $\mathbf{k}_{\parallel}$-vector. In order to clarify this point, an additional evaluation of the effective mass of electrons in quantum well states was made. Dispersions E($\mathbf{k}_{\parallel}$) of sp-states are well described by a free-electron parabolic function E($\mathbf{k}_{\parallel}$)=E$_0$+$\frac{h^2 k_{\parallel}^2}{8\pi^2 m_{\parallel}^*}$ for relatively small values of the in-plane wave vector $\mathbf{k}_{\parallel}$. Here E_0 is the QWS energy detected in normal emission and $m_{\parallel}^*$ is the in-plane effective mass of the electron. A simple least-square fit for relatively small values of the wave-vector (-0.2Å^{-1} < | $\mathbf{k}_{\parallel}$ | <+0.2Å^{-1}) gives the values of the effective mass which are specified for each QWS in terms of the free electron mass m_e in Fig. 2.4(b). The diagram in Fig. 2.4(c) shows a plot of the in-plane effective mass versus binding energy of the confined electron. It is seen that the effective mass $m_{\parallel}^*$ decreases slightly for quantum numbers n=1 to 2, and falls drastically for n=4 and $n = 5$ at binding energies higher than 2.5 eV. Such behavior is rather untypical. For metal-on-metal systems where the confined electron undergoes backscattering mainly in the gap region, the effective mass naturally increases for increasing binding energy [89]. An anomalous behavior of $m_{\parallel}^*$ has been observed in systems with strong influence of the substrate on the electronic structure of the metallic overlayer. In particular, a decrease of the effective mass
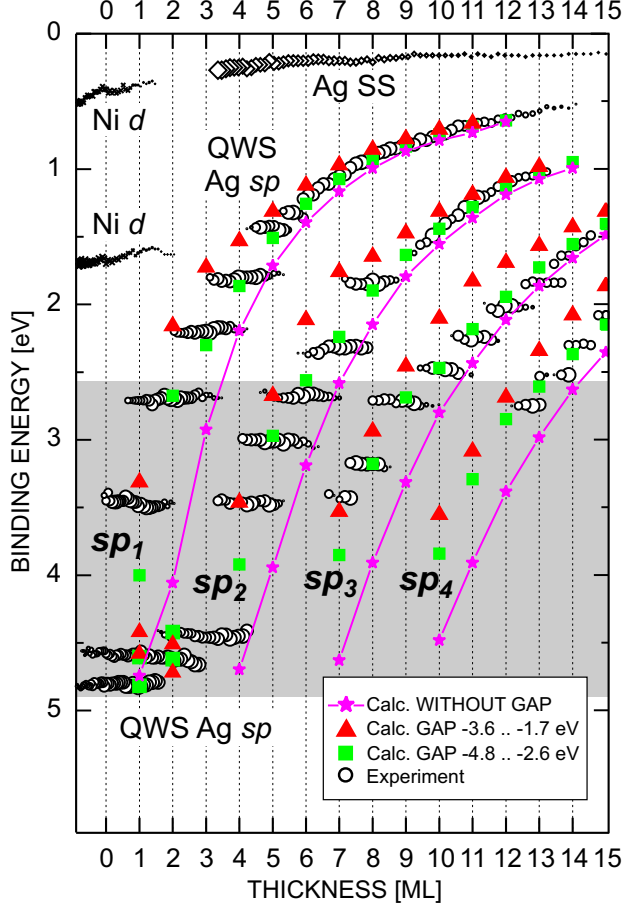
36

Figure 2.3: (a) thickness-dependent electronic structure of QWS's in Ag on Ni(111). Measured binding energies are given as open circles. Signs (■) denote results from the phase accumulation model closest to experiment i.e. for the gap 4.8 – 2.6 eV. Marks (▲) represent the QWS's calculated within the same model for the experimentally measured gap of Ni taken from Ref. [56]. Stars (★) represent QWS energies for a hypothetical substrate without gap.

with increasing binding energy of QWS in Ag on V(001) has been explained in terms of hybridization between the Ag sp-band and the d-band of V [91]. An effect of the same nature have been observed in Ag/Si(111) and Ag/Si(001) [76]. Based on this, interfacial hybridization between the $sp(\Lambda_6)$-band of Ag and $d(\Lambda_1, \Lambda_3)$-bands of Ni can be claimed in Ag/Ni(111). Since it is known that hybridization with substrate states tends to increase the value of $m_\parallel^*$ [82, 89] the observed kink in Fig. 2.4(c) is considered as first indication that upper edge $\Lambda_1^{\min}$ of the substrate gap lies between quantum well states with $n=3$ and $n=4$.

Having established the role of the interfacial hybridization, the *extended phase accumulation model* will be applied to describe the electronic structure of quantum wells and to determine the substrate gap edges more accurately. This model is a method of choice for systems with substantial electron scattering outside of the projected energy gap. The extended phase accumulation model originates from

11ML Ag/Ni(111)
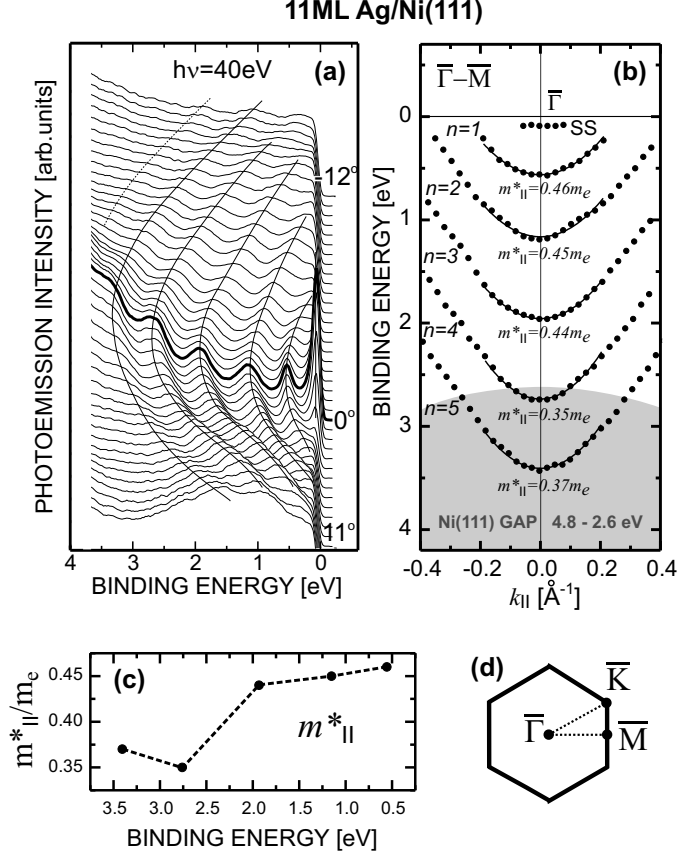
Figure 2.4: $\mathbf{k}_\parallel$-dependent electronic structure of quantum well states in 11ML of Ag on Ni(111); (a) photoelectron spectra taken for different emission angles; (b) dispersions $E(\mathbf{k}_\parallel)$ extracted from (a). The Ni(111) surface projected gap according to local density theory is plotted in gray; (c) behavior of the in-plane effective mass $m_\parallel^*$ with QWS energy; (d) surface Brillouin zone of the (111)-face of the f.c.c. crystal structure.

the conventional model [92, 77], which describes the formation of standing electron waves in a potential well in terms of the basic phase equation [86]:

$$(2.1) \qquad \Phi_B + \Phi_C + 2kd = 2\pi n$$

In this formula Φ_B and Φ_C denote the phase shift of the electron wave function upon its reflection at the surface barrier and at the interface. k is the wave vector of the electron propagating in the Ag overlayer and d means the overlayer thickness. For the term Φ_B the common semi-empirical form for the surface barrier on metals [82, 86] is taken:

$$(2.2) \qquad \Phi_B = \pi \times \left[\frac{3.4\text{eV}}{E_V - E_B}\right] - \pi$$

38

Here E_V denotes the vacuum level and E_B is the electron binding energy. As Φ_C is responsible for reflection of the propagating electron at the interface (i.e. is related to the relative energy gap of the substrate), it will be expressed in terms of the gap borders $E_{U,gap}$ (which we denoted above as $\Lambda_1^{\min}$) and $E_{L,gap}$ ($\Lambda_1^{\max}$)- the top and the bottom edge, respectively (see Fig. 2.5)

$$(2.3) \qquad \Phi_C = 2 \times \arcsin\sqrt{\frac{E_B - E_{L,gap}}{E_{U,gap} - E_{L,gap}}} - \pi$$

In the extended phase accumulation model which is used in the analysis, the phase equation (2.1) undergoes modification by an extra term Φ_{scatt} which extends the potential for interfacial reflection beyond the edges of the relative gap:

$$(2.4) \qquad \Phi_B + \Phi_C + 2kd + \Phi_{scatt} = 2\pi n$$

It is established that Φ_{scatt} has the same mathematical form as Φ_C from Eq. (2.3) [93]. In the case of Ag/Ni(111) Φ_{scatt} extends from $\Lambda_1^{\min}$ to the top of the Ag sp-band at 0.3 eV (Fig. 2.5(a)). Another specific feature of the extended phase accumulation model is the expression for the term $2kd$, which denotes the wave function of the propagating electron. Based on the recent tight-binding-calculations for the electronic structure of the simple atomic chain [87, 88] the term $2kd$ is introduced in the following form [81]

$$(2.5) \qquad 2kd = 2 \times \arccos[1 - \frac{2E_B}{E_{U,band} - E_{L,band}}]$$

where $E_{U,band}$ and $E_{L,band}$ describe the edges of the Ag band involved in the confinement.

Now one can obtain energy levels of quantum well states as the values E_B which satisfy the phase equation (2.4). Fig. 2.5(b,c) shows for reference the band structures of Ag and Ni in the direction Γ-L of the bulk BZ. Note that the plot in Fig. 2.5(c) displays two alternative band structures of Ni. The one which is marked by black lines was calculated by KKR and LCGO methods [7, 79]. The other one, shown in gray is an experimental band structure and was measured directly by angle-resolved photoemission of Ni [56, 55]. One can clearly see the mentioned difference of $\sim$1 eV in the location of the $d(\Lambda_1)$-band. The experimentally measured band is narrower, positioned at lower binding energies, and defines a substrate gap from 1.7 to 3.6 eV. In contrast, the gap calculated using the KKR method covers an energy region from 2.69 eV to 4.78 eV, i.e. situated significantly deeper.

In order to find out the substrate gap which provides the best description of the experimentally observed quantum well states, a fit procedure has been developed, where parameters of Ni bands were varied seeking the best correlation between experimental QWS energies and those given by Eq. (2.4). For this purpose a special
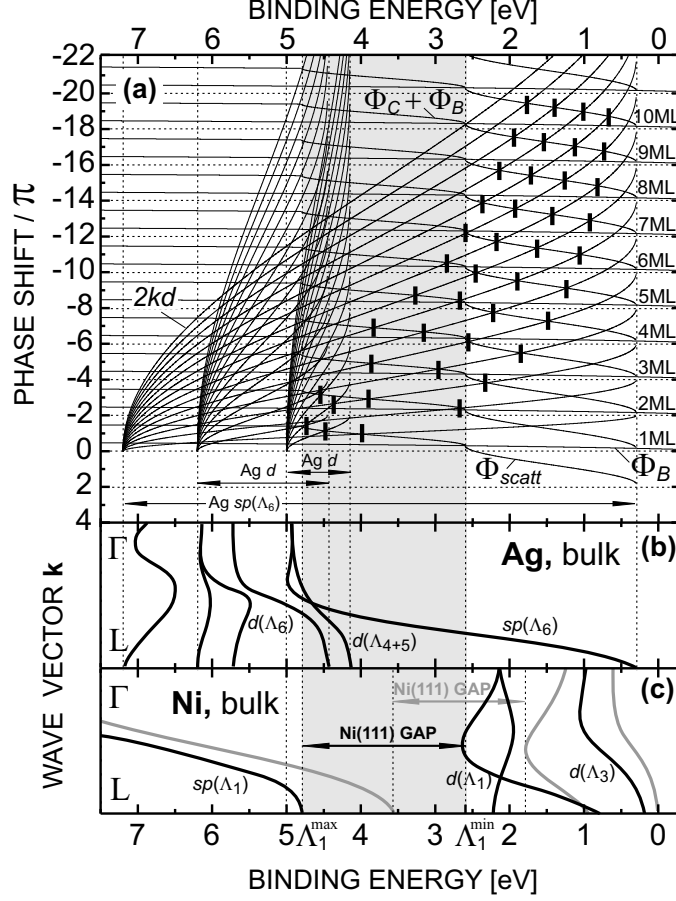
Figure 2.5: (a) phase diagram illustrating the graphical solution of the extended phase equation (2.4); (b) and (c) - the band structures of Ag and Ni given for the ΓL direction of the bulk BZ on the same energy scale. The Ni(111)-surface-projected gap for which QW energies are derived is represented by the gray bar.

software was written and the results of the numerical solution are presented in the phase diagram in Fig. 2.5(a). Three bands of Ag ($sp(\Lambda_6)$ for the calculation of sp QWS branches below 4 eV, and two d-bands (Λ_6 and Λ_{4+5}) to describe QWS's of d-type between 4 and 5 eV) were involved in the analysis of the confined electronic structure. Corresponding terms $2kd$ of the electron wave-functions in these bands are plotted for all 15 ML by black solid lines in Fig. 2.5(a). As scattering potential below the lower edge of the gap ($E_B < E_{L,gap}$) just Φ_B has been used. Inside the gap ($E_{L,gap} < E_B < E_{U,gap}$) the electron phase shift upon reflection at the surface and the interface was determined as the sum $\Phi_B + \Phi_C$. Above the upper gap border ($E_{U,gap} < E_B < E_{U,band}$) the term Φ_{scatt} was implemented up to the upper edge of Ag $sp(\Lambda_6)$-band. Energy values at which the term $2kd$ intersects the scattering potential are the required solutions of the phase equation (2.4) for energy levels of QWS for a system with d ML Ag/Ni(111).

The fitting algorithm employed to vary the edges of the Ni(111) relative gap $E_{L,gap}$ and $E_{U,gap}$ uses as minimization criterion the sum of absolute energy devia-

tions $\sum_{n=2}^{12} | E_{B,n} - E_{exp,n} |^2$ in QWS branches (E_B and E_{exp}, respectively, denote calculated and measured QWS levels in the overlayer). The fitting criterion does not include the energy of the first QWS in each branch, since effects of interband hybridization between sp- and d-states of Ag are significant there. They affect the electron wave function at binding energies above 3.5 eV, making the phase accumulation model inappropriate for description. In fact, similar problems have been observed earlier [83].
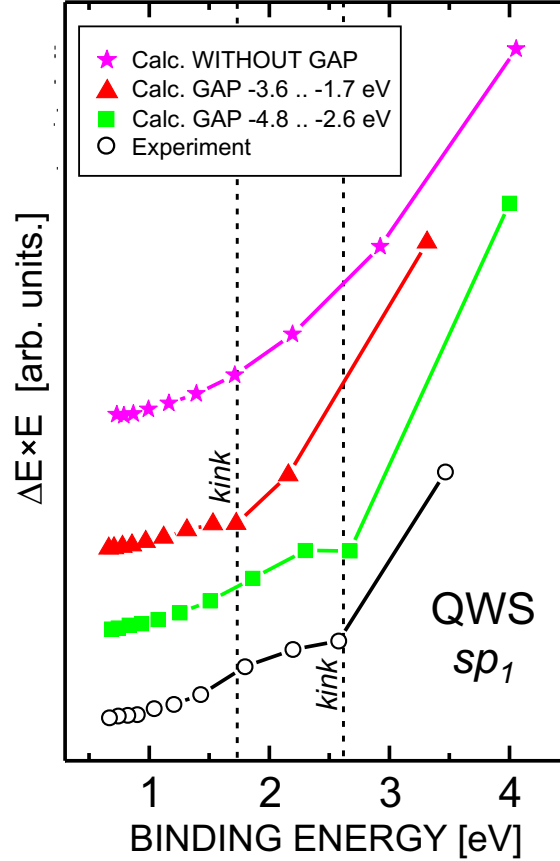
Figure 2.6: Behavior of finite energy difference of quantum well states in the sp_1 branch with binding energy. Experimentally measured QWS energies demonstrate a kink at near 2.6 eV. The same is calculated in the case of a substrate gap 4.8-2.6 eV. Model calculations performed without gap reveal no kink at all.

The outcome of the variational fit analysis is reported in Fig. 2.3. Best consistency with measured energies of confined electrons was found for the Ni(111) gap extending from 2.6 eV to 4.8 eV (the solution of the phase equation for this gap is shown in Fig. 2.5(a)). The gap itself is marked with gray. The obtained results are compared with experimentally measured energies in Fig. 2.3, where QWS's calculated for the 2.6–4.8 eV gap are denoted by green symbols (■). Results of a calculation for the Ni(111) gap measured directly by photoemission [56, 55] are also shown (red marks (▲)). As one can see, the experimental gap provides much less correlation between calculated and measured electronic structure of quantum

Table 2.1: Binding energies (eV) of Ni bands in the high-symmetry direction of the bulk BZ ΓL and corresponding parameters of the Ni(111) surface projected gap obtained by different methods.

Method	Ref.	Γ (Γ'_{25})	L (L_1)	$E_{L,gap}$ ($\Lambda_1^{\max}$)	$E_{U,gap}$ ($\Lambda_1^{\min}$)	Gap width
Exp., PES	[56]	-1.1	-3.6	-3.6	-1.7	1.9
Theor., KKR	[79]	-2.15	-4.78	-4.78	-2.69	2.09
This work, QWS		-	-4.8	-4.8	-2.6	2.2

wells, it even leads to some missing energy levels, especially in the sp_2-branch. Different Ni band structures along [111] are summarized and compared in Table I. As one can see, the gap obtained from the variational fit procedure is almost perfectly consistent with the one determined by local density calculations in contrast to the gap taken from the Ni band structure measured directly by photoemission. For completeness of the analysis, a model calculation of binding energies of quantum well states without relative gap in Ni was also performed (only Φ_{scatt} from -4.8 to -0.3 eV is considered and the gap edge ($\Lambda_1^{\min}$) is skipped). The obtained binding energies are shown in the diagram in Fig. 2.3 with magenta stars (★). They are obviously much deeper in energy than the experimental data points.

The position of ($\Lambda_1^{\min}$) can be obtained more evidently if the finite energy difference $\Delta E = [E(N+1) - E(N)] \cdot E(N)$ of QWS is analysed (N denotes the number of monolayers). It is plotted against the binding energy in Fig. 2.6. While ΔE calculated without gap (★) demonstrates a monotonously increasing behavior, it has obvious kinks at $\Lambda_1^{\min}$ when the gap is considered (1.7 eV for ▲ and 2.6 eV for ■). One can easily see in Fig. 2.6 that ΔE of quantum well states measured in this work (○) exactly repeats the behavior of ΔE calculated for a substrate gap with $\Lambda_1^{\min}$=2.6 eV in the formalism of the phase accumulation model.

So far, the upper edge $\Lambda_1^{\min}$ can be determined from the fit procedure and is consistent with the behavior of the effective mass (Fig. 2.4(c)). The situation with the bottom edge of the gap $\Lambda_1^{\max}$ is more ambiguous. An analysis of dispersions of sp-QWS's is not possible at binding energies above 3.5 eV due to intense photoemission from Ag d-states (Fig. 2.2(b)). Moreover, a variation of the gap bottom affects the structure of quantum well energy levels only indirectly, as opposed to $\Lambda_1^{\min}$ which is situated much closer to E_F. One possibility of a more precise analysis is a variation of $\Lambda_1^{\max}$ in order to fit QWS's derived from $d(\Lambda_{4+5})$- and $d(\Lambda_6)$-bands of Ag between 4 and 5 eV (Fig. 2.2). Their data points as well as calculated values are shown in the bottom of Fig. 2.3. Since the experimental gap 1.7–3.6 eV (top row in Table 2.1) does not reach the upper edge of these bands (see Fig. 2.5(b,c)) the existence of QWS's of d-type at 4.55 and 4.75 eV is not supported by the experimental gap. Furthermore, an evaluation of their energies for the 1.7–3.6 eV gap fails to give consistency with the experiment. The gaps listed in rows 2 and 3 of Table 2.1 are more easily justified in this respect. Their bottom edge $\Lambda_1^{\max}$ is located at ~4.8 eV i.e. inside of the d-band of Ag, which is more physical. It

also means a good correlation to the experimentally measured energy levels (Fig. 2.3). However, due to the aforementioned interband hybridization between d- and sp-states of Ag this result is not unambiguous.

As a final remark, it would be interesting to compare the presented results to the data of Ref. [78, 77]. According to these works, Ag on Ni(111) forms a diffuse interface boundary where the electron is lost due to incoherent scattering and the discrete peaks observed are an effect of quantization only in the final state of photoemission. While this interpretation may hold for the low photon energies (<15 eV) as used in Ref. [78], it is not realistic for high energies like 50 eV in the present study. Also the bulk band structures in Fig. 2.5 suggest that Ag/Ni(111) represents the classical case of a quantum-well system with strong confinement inside of the gap and "leaky" behavior outside. This is supported by the present analysis based on the phase accumulation model.

In summary, the behavior of quantum-well states in Ag/Ni(111) with $\mathbf{k}_\parallel$ and with thickness has been analysed. Quantum-well energies derived from the phase accumulation model were fitted to the experiment with the Ni bulk band gap as free parameter. In this way the minimum of the Λ_1 band has been determined as 2.6 eV in good agreement with early local density calculations of Ni. From the analysis of d-type quantum well states the bottom edge of Ni(111) substrate gap was revealed at 4.8 eV. Agreement for other values fails, in particular for those derived from photoemission data. This result supports the simplest view on photoemission from Ni, stating that electron correlation in the ground state is sufficiently described by standard local density theory and deviations are final state effects.

2.2 Summary of conclusions

Angle-resolved photoemission measured at moderate photon energies shows that Ag/Ni(111) is a case of a classical quantum-well system, characterized by *initial* state confinement of Ag *sp*- and *d*-bands in the energy gap of the Ni(111) substrate. The application of extended phase accumulation model for calculation of the quantum well energies is physically justified and allows indirect probing of the Ni(111) band structure through a variational fit procedure where the edges of substrate gap are taken as free parameters.

The upper edge of Ni(111) gap (the bottom of Ni $d(\Lambda_1)$ band $\Lambda_1^{\min}$) can be determined from the analysis of the confined electron's effective mass. Its behavior with binding energy demonstrates a significant lowering at the edge of the Ni gap as a result of hybridization between Ag and Ni bands. The gap border can more precisely be determined by the jumps in monotony of QWS energy levels. The energy difference plotted for experimentally measured quantum well states demonstrates a kink at 2.6 eV. This kink is in agreement with model calculations performed in the framework of the phase accumulation model for corresponding parameters of the substrate gap. Thus, the upper gap edge $\Lambda_1^{\min}$ is determined to have a binding energy of 2.6 eV. This value is perfectly consistent with the theoretical band structure of Ni obtained in the local-density approximation formalism.

Chapter 3

Towards Lower Dimensionality: Stepped Surfaces

Physics of two-dimensional epitaxial overlayers has for a long time been in the focus of research activities, since they are very important for applications. Technology uses multilayers in many respects - from light-emission diodes [120] to magnetic storage and control devices [121]. Nowadays systems of lower dimensionality are becoming even more important. Since integrated circuits tend to miniaturize and technology goes into the nanometer scale [14, 15, 16], the consideration of quantum size effects in the electronic structure of novel devices becomes unavoidable. This requires some basic models, which help to understand how electron transport in the elements of the circuit is affected by reduced dimensions.

One of the simplest cases of such model systems is the stepped (vicinal) metallic surface, where the electrons are affected by the periodicity of the steps and may become quantized in the potential of a single terrace [101]. This model can be extended to the more common case of uniform quantum wires or nanostripes, periodic arrays of which can be prepared on a vicinal template by step decoration. The behavior of electrons in such systems is believed to be close to the one in a real conductor of an integrated device. The following chapter deals with studies of the electronic structure of stepped surfaces and nanostructures self-organized on top.

3.1 Electronic structure of vicinal W($nn1$)

3.1.1 Introduction

By cutting a single-crystal in a certain orientation relative to main crystallographic directions, one can produce a regular superlattice of atomically uniform steps or terraces the periodicity of which will be strictly defined by the angle of miscut. Stepped surfaces are envisaged as adequate templates for the growth of a large number of identical nanostructures like quantum wires and quantum stripes [95]. Such nanostructures may gain unique properties like anisotropic and quantum- size dependent electronic structure [126, 127, 128]. Whether or not these effects will in the future be used, depends on the ability of the stepped substrate to support quantization effects in the electronic structure. The method of choice to test this is angle-resolved photoemission which provides the electronic structure including band dispersions [21].

The stepped surfaces most extensively studied to date are the (111) vicinals of f.c.c. Cu and Au, where surface state electrons in a narrow bulk band gap at the L-point are probed [99, 100, 101, 167, 102, 105]. Shockley-type surface states prove themselves as quasi-two-dimensional electron gas, featuring low inelastic scattering and Fermi wave-lengths significantly larger than the interatomic lattice constant. These points emphasize their high potential for studies of quantum-size effects in metals. Although most of the physics of Shockley surface states can be described in terms of elementary wave mechanics [98], there are many ambiguities and intriguing issues. For instance, different types of surface state behavior have been observed: the wave functions were either spread out over the "optical" macrosurface [99, 102, 103, 105] or localized at the terrace microsurface [167], and a switch over from two-dimensional to one-dimensional behavior was observed at a step width of $\sim$ 17 Å [101] (see graphical illustration in Fig. 3.1(c) and (d)). Most recently, intense final-state effects due to so-called *umklapp* scattering at the superlattice of steps and stripes have been observed in photoemission from carbon nanostripes on stepped Ni(771) [170]. Similar effects occur also in the electronic structure of vicinal Au(111) [168]. In the *umklapp* effect the photoelectron can undergo scattering at the surface lattice when leaving the crystal and acquire an extra reciprocal surface lattice vector which leads to observable final-state effects, especially when the surface periodicity differs from the one of the bulk [106, 107, 108]. Taking all of these points together, it becomes clear why the electronic structure of stepped surfaces is highly important for the understanding of nanostructures which can be fabricated on top of such templates.

Since in the present work step decoration of Au with unique electronic structure has been successfully produced on top of vicinal tungsten (see the next Section), it was decided to clarify the presence of one- or two-dimensional behavior and initial- or final-state effects on stepped W(110). Tungsten is in principle well suited since theory predicts a substantial portion of the W density of states surface localized [109] although the identification of surface states in an experiment is often complicated and has on W been achieved only for a small number of cases [164].

While experimental data is still outstanding, theory went ahead predicting, e. g., that W surface states will be important even for the own stability of the substrate steps [145].

A strong superlattice effect fulfilling the periodicity of the step superlattice will be reported in the following. By angle- and energy-dependent measurements in photoemission and in low-energy electron diffraction (LEED), it will be shown that the observed behavior is due to a final-state diffraction at the step superlattice instead of a superlattice band structure effect on the initial state.

3.1.2   Experimental details

The (331) and (551) faces of W have been investigated in the experiment besides W(110). These surfaces are characterized by terrace widths of three and five tungsten lattice constants, respectively, or 9.5 Å and 15.8 Å. Fig. 3.1(a) and (b) show the surface atom arrangement across the steps. Single crystals used in the experiments were commercially supplied. In the production procedure the angle of miscut α (Fig. 3.1)(c) was determined by X-ray diffraction to 0.1° precision of the surface orientation for cutting and successive mechanical polishing. The miscut angle amounts to 13° for W(331) and 8° for W(551) along the [001] direction leading to step edges oriented along [1$\overline{1}$0]. The surface unit cell is determined by double step width. In Fig. 3.1 the surface unit cells of W(110) and of the superlattice are marked with rhombuses. The step width is marked as L_{331} and L_{551} for W(331) and W(551), respectively.

Peculiarly to the experiment, the samples were cleaned *in situ*. In order to remove carbon, which originates from the hydrocarbons used for surface polishing and from the bulk of W, an oxygen treatment used to be done. The tungsten sample was heated several times in a partial pressure of O_2 of 1×10^{-7}mbar at 1200°C. Successive flashing to 2200°C removes residuals of oxygen leading to sharp $p(6 \times 1)$ and $p(10 \times 1)$ step reconstructions of W(331) and W(551), respectively, in the LEED. Experimental aspects of the photoemission measurements were described in detail in previous Chapter. Photoelectrons were excited with linearly polarized synchrotron light at the U125/1 and UE56/1 PGM beamlines [235, 236] at BESSY.

3.1.3   Results

Angle-dependent photoemission

Fig. 3.2 displays angle-resolved photoemission spectra of W(331) for $\mathbf{k}_{\parallel}$ vectors parallel (a) and perpendicular (b) to the step direction at 62.5 eV photon energy for different polar angles. Here and further on all polar angles θ are related to the [110] microsurface normal (see illustration in Fig. 3.1(d)). The bottom of Fig. 3.2 shows for the sake of comparison normal-emission spectra from flat W(110) measured in a way to ensure the same measurement conditions as for the vicinal substrates. In particular, the $\mathbf{E}$-vector of the light points along [0$\overline{1}$1] in Fig. 3.2(a)
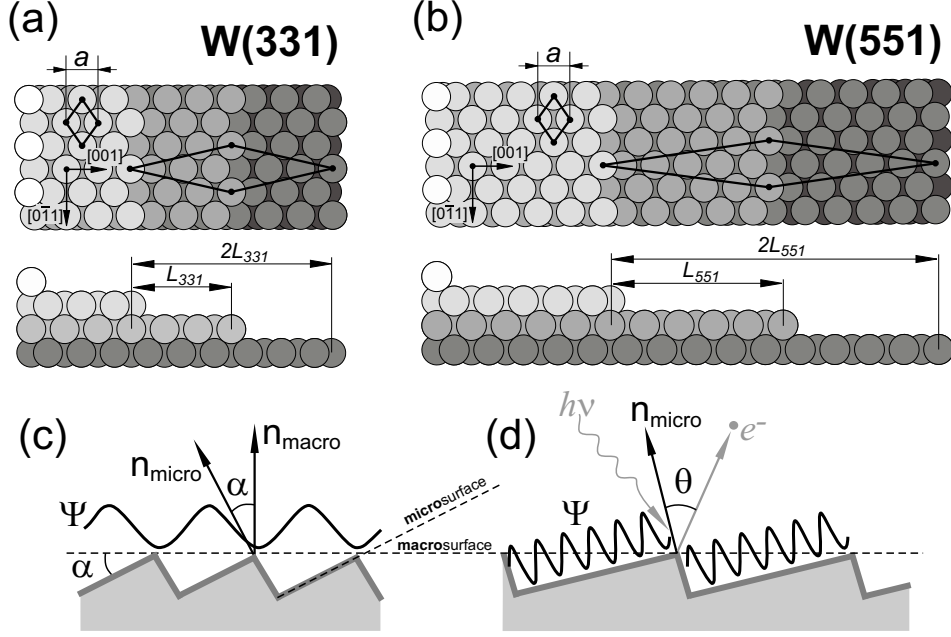
Figure 3.1: Geometry of W(331) (a) and W(551) (b). The steps run perpendicular to the [001] or ΓH direction and are by a factor of 5/3 wider on W(551); Two models of surface states are shown. The wave function either propagate along the "optical" macrosurface (a) or is localized on the terrace microsurface (b). Also $\mathbf{n}_{micro}$ and $\mathbf{n}_{macro}$ vectors of surface normal and detection angle θ are defined.

and along [001] in 3.2(b) for both flat and stepped surfaces. Prominent features identified earlier on W(110) are an intense surface resonance (S.R.) at 1.2 eV for $\overline{\Gamma}$ [164, 165, 81] and bulk emission from the top of the Σ_1 band which is sampled near the N-point (N_1) of the bulk Brillouin zone when the excitation energy is around 63 eV. Details of the electronic structure of bulk W taken from Ref. [164] can be found in Fig. 3.3. Photoelectron excitations at different $h\nu$ are shown with dashed arrows. Spectra obtained in the normal to terrace (i.e. microsurface) direction [110] in the emission-angle series from W(331) in Fig. 3.2, are colored red. For $\mathbf{k}_\parallel$ parallel to the steps (Fig. 3.2(a)), peak S is seen to disperse symmetrically about the microsurface normal. Low intensity of the surface-resonance peak at 1.2 eV binding energy [164] can be explained if one suggests that bulk emission (which is degenerate on W(110) (Fig. 3.3)) dominates the peak at 1.2 eV on the vicinal substrate. The [110]-normal-emission spectra of stepped and flat W(110) display strong differences. For W(331), the Σ_1 band does not appear at 6 eV as for W(110) but at 5.2 eV where states are *forbidden in bulk W* due to the large gap from 6.2 to 3.3 eV for emission along [110] [164, 81] (see Fig. 3.3, the gap is shown in gray). Since the surface localized states can be identified by their non-dispersing character with variation of the excitation energy [20], and because the photoelectron kinetic energy largely determines the possible final-state effects [104, 170], extensive $h\nu$-dependent studies have been performed. A lot of dispersions, measured with different photon energies from W(110), W(331) and

W(551) in the [001] direction (perpendicular to the steps), are shown in Fig. 3.5.
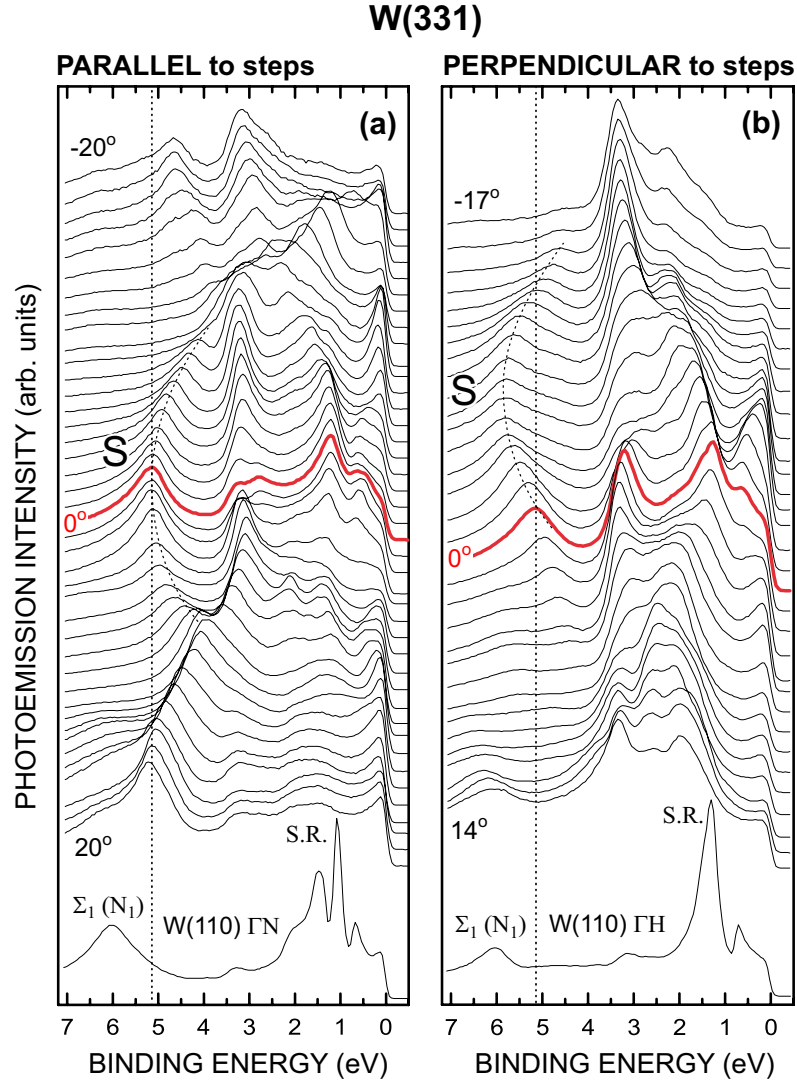
W(331)

Figure 3.2: Angle-dependent photoemission spectra of W(331) parallel (a) and perpendicular (b) to the step direction for $h\nu$=62.5 eV. The bottom of the band labeled S appears 6° away from the terrace normal.

Fig. 3.5(a) indicates the presence of a surface resonance on flat W(110) which has not yet been reported inside or near the W gap (6.2–3.3 eV) in any work. The dispersion measured at $h\nu$=62.5 eV gives only an indication for this since it comprises degenerate bulk and surface bands. At $h\nu$=110 eV photon energy, however, the Γ point is reached (see Fig. 3.3) and the bulk derived emission along [110] from Σ_1 corresponds to the band bottom at 9 eV. No other peaks from W bulk are expected in normal emission in the whole energy range from 9 eV up to the border of the band gap at 3.3 eV. Nevertheless, a dispersion has remained at 5.8 eV and is identified with *surface emission*. This band is marked in Fig. 3.5(a) with black symbols (■). Its dispersion $E(\mathbf{k}_{\parallel})$ follows the shape of the bulk band
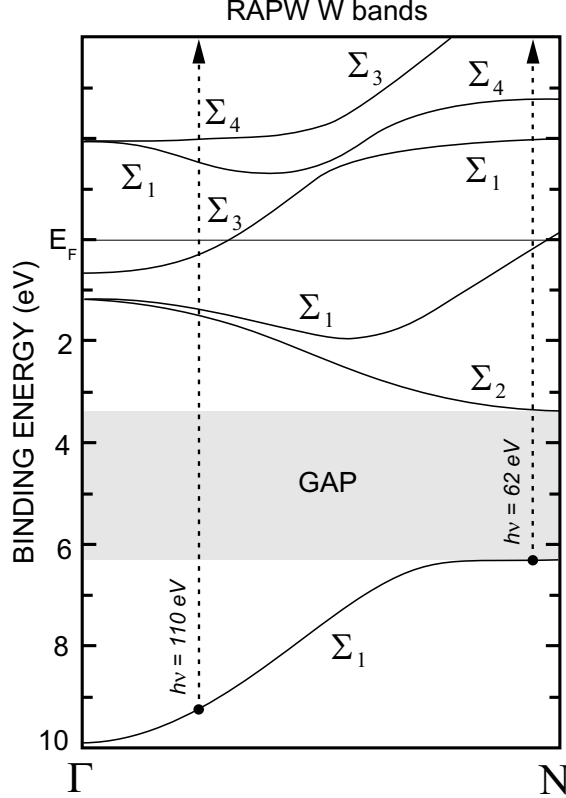
Figure 3.3: The electronic structure of bulk W taken from Ref. [164] has been calculated using relativistic augmented plane wave (RAPW) method. Photoemission transitions of the electrons excited from the Σ_1 band along [110] are shown for different $h\nu$ by dashed arrows.

gap according to the surface projection of the bulk bands calculated in Ref. [110].

Let us return now to Fig. 3.2. A very intriguing effect has been revealed in angle-dependent spectra measured from W(331) in the direction perpendicular to the steps. The 5.2 eV peak disperses downwards reaching a minimum energy of 6 eV up the stairs about 6° away from the terrace normal (at this angle the same energy is reached as for normal emission on flat W(110)). Additional $h\nu$-dependent photoemission measurements allow a better judgement of this behavior. Fig. 3.4(a)–(c) demonstrate a color-scale representation of photoemission spectra at 50- , 62.5- and 125-eV photon energy for different emission angles perpendicular to the steps. Changing the photon energy, one moves in terms of the W bulk band structure along the [110]- or Σ-direction away from the N-point (~ 63 eV) towards Γ (Fig. 3.3). At $h\nu$=62.5 eV, one branch S with binding energy between 4 and 6 eV, shifted away from the microsurface normal is observed. At $h\nu$=50 eV, additionally a second branch S* appears at positive emission angles. At 125 eV photon energy, both branches S and S* are equally pronounced and shifted symmetrically with respect to the microsurface normal.

Characterization with LEED

Considering the high probability of a final-state influence on the observed electronic structure of the valence band (Fig. 3.4(a)–(c)), additional LEED measurements have been done. In the LEED picture, the electron at the surface undergoes "outer" scattering in the final state of the "inner" photoemission process. Considerable correlation with results of photoemission have been found. It was revealed that intensities of two bands S and S* which vary strongly with photon energy so that at hν=62.5 eV the S* branch even vanishes (Fig. 3.4(b)) exhibit exactly the same behavior as intensities of vicinal superlattice spot in the LEED with variation of primary electron energy E_p. The LEED patterns photographed *in situ* for comparable energies of the electron beam are displayed in Fig. 3.4(d)-(f) *vis-à-vis* the measured dispersions. The LEED spots (dispersions) are split for 44 eV (50 eV) and 125 eV (125 eV), and for 62.5 eV (62.5 eV) almost all of the intensity is concentrated in a single spot (band).

3.1.4 Discussion

The dispersions presented in Fig. 3.5 allow to determine the shift between the two branches S and S* as 0.66 Å^{-1} for W(331). For W(551) one can even observe a repeated band structure of more than two branches with a period of 0.40 Å^{-1}. These values correspond exactly to the period of the superlattice Brillouin zones of the two surfaces or, following a simple reasoning, to the distance from $\overline{\Gamma}$ to $\overline{\Gamma}'$ along [001] for W(110) (4.0 Å^{-1}) divided by the 6-fold and 10-fold surface periodicities measured by LEED. The surface Brillouin zones of W(110), W(331) and W(551) are shown in Fig. 3.5 right next to the dispersions. Corresponding high symmetry points of the step superlattice are marked as $\tilde{\Gamma}$ and $\tilde{\Gamma}'$. In the Brillouin zone picture, the electron is assumed to hop across the steps and form Bloch waves along the macrosurface. This is the simplest interpretation in which the repetition of the band dispersion is due to band periodicity in the repeated zone scheme of the step superlattice. Such behavior would very well be compatible with an identification of the feature S as surface resonance. This requires the wave function to be oriented parallel to the macrosurface (Fig. 3.1(c)) [99, 101], which means that in order to be an initial-state effect, the repeated $E(\mathbf{k}_{\parallel})$ dispersions for various photon energies must coincide when $\mathbf{k}_{\parallel}$ is related to the *macrosurface* ($\mathbf{k}_{\parallel} = 0$ corresponds to the macrosurface normal) and deviate when $\mathbf{k}_{\parallel}$ is related to the microsurface ($\mathbf{k}_{\parallel} = 0$ at the microsurface normal). Due to the large miscut angles between macro- and microsurface of 13° for W(331) and 8° for W(551) the reported experiment can distinguish between the two cases. Dispersions of the bulk-derived W bands (like Σ_1) allow unambiguously to determine the direction of the microsurface normal, which corresponds to bulk photoemission along [110]. This is also very clearly seen in the original data of Fig. 3.2(b) where the peak at ∼ 1.5 eV disperses around the microsurface normal. A plot relative to the macrosurface clearly fails. It can be seen from the marks of macrosurface normals for photon energies of 50, 62.5, and 105 eV which were inserted into Fig. 3.5(b) and are clearly separated. The

one for 125 eV would appear outside of the figure frame. This proves that in its initial state the electron occupying S remains localized at the one-dimensional microsurface (as shown in Fig. 3.1(d)) and that the repetition of band S is not due to an initial-state effect.
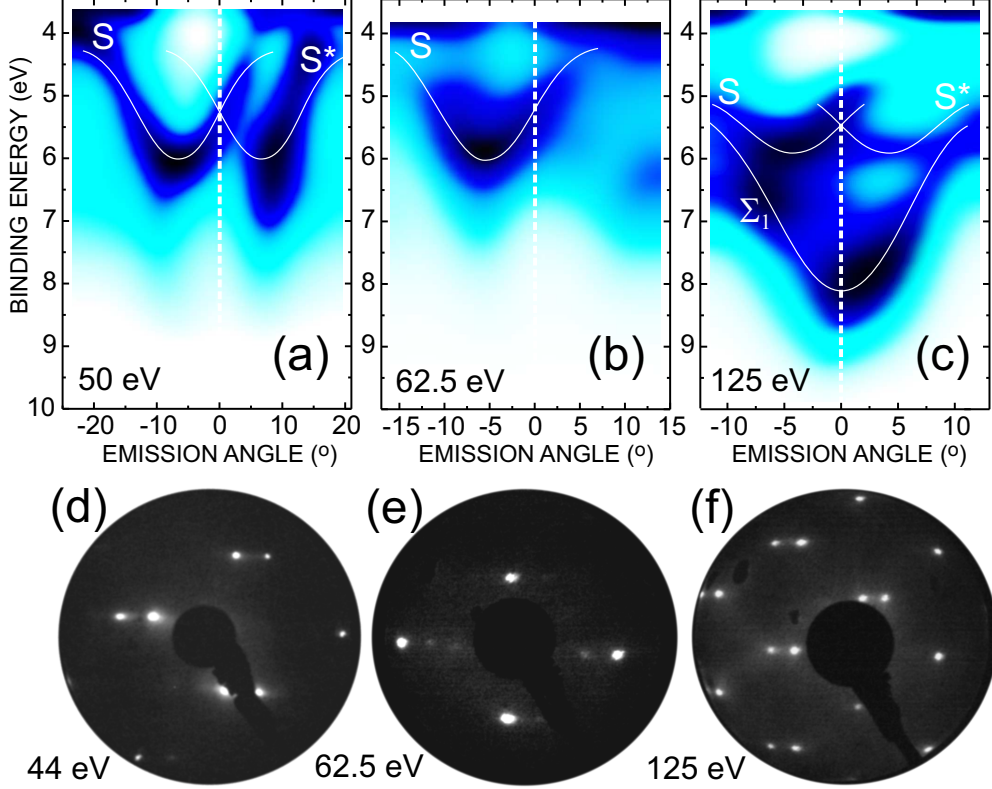

Figure 3.4: Extraction of dispersions from photoemission spectra for W(331) (a–c) together with LEED patterns of similar intensity behavior (d–f). The emission angle is given with respect to the [110] microsurface normal. Photoemission intensity is represented on an inverted color-scale: darker areas correspond to a more intense signal.

It is challenging to propose a model which can appropriately describe the observed effects. One can explain the results on the basis of a description by umklapp scattering at the vicinal superlattice. In the *umklapp* the photoelectron acquires an extra reciprocal surface lattice vector G as a result of scattering at the surface lattice:

$$(3.1) \qquad \mathbf{k}_{\parallel,vacuum} = \mathbf{k}_{\parallel,crystal} + \mathbf{G}_{\parallel}$$

However, in such a form this equation does not describe the experiment with $\mathbf{G}_{\parallel} = \Delta k_{331} = 0.66 \ \text{Å}^{-1}$ for W(331) and $\mathbf{G}_{\parallel} = \Delta k_{551} = 0.40 \ \text{Å}^{-1}$ for W(551). Instead, if the dispersion of band S on flat W(110) with $\mathbf{k}_{\parallel,crystal}$ is compared with the dispersions measured on W(331) and W(551), one obtains $\mathbf{k}_{\parallel,vacuum} = \mathbf{k}_{\parallel,crystal} \pm \mathbf{G}_{\parallel}/2$ with the dispersion for $\mathbf{k}_{\parallel} = 0$ completely missing.
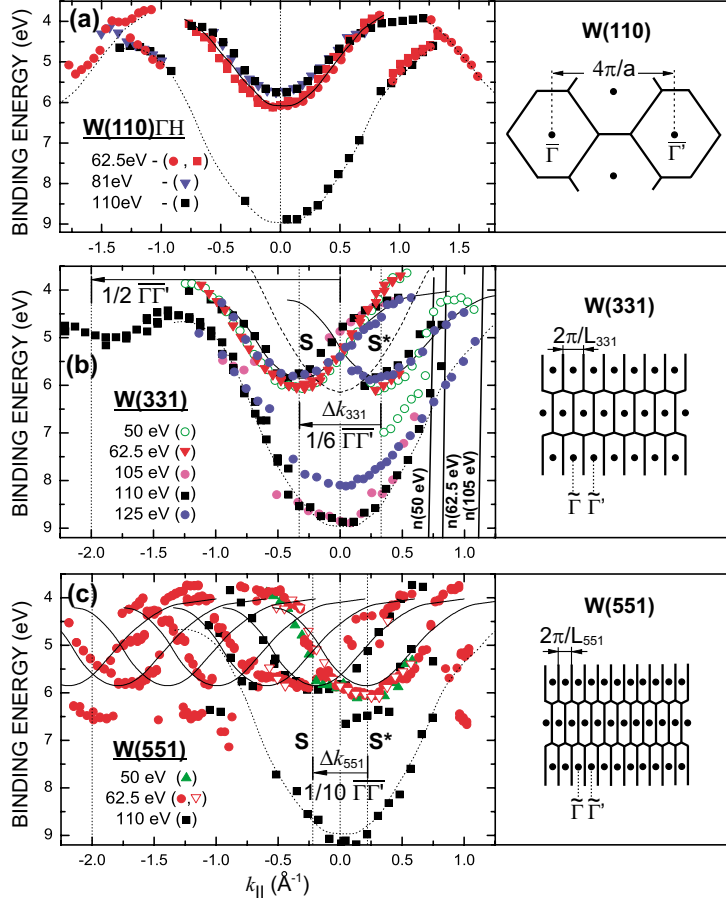
Figure 3.5: Dispersion for $\mathbf{k}_\parallel$-vectors along [001] for W(110) (a) and for W(331) (b) and W(551) (c), i. e., perpendicular to the steps. $\mathbf{k}_\parallel$ is given relative to the [110] microsurface normal. The macrosurface normal $n(h\nu)$ shifts strongly between 50 and 105 eV (125 eV outside of the frame) and is therefore not a reference for the repeated surface band S. Corresponding surface Brillouin zones are shown next to the dispersions.

More appropriate is the description given for LEED from stepped surfaces [111, 112]. Fig. 3.6 (see Ref. [111]) compares Ewald constructions for diffraction from ideal flat (a) and stepped surfaces (b). Fig. 3.6(b) shows how a single LEED spots splits up into two, when the $\mathbf{k}$-vector moves from the in-phase to the antiphase condition. The reciprocal lattice rods for scattering from a stepped surface are perpendicular to the macrosurface and therefore tilted with respect to the microsurface. Because they pass through the Γ-point of W, scattering conditions remain unchanged there, but they separate at the N-point (antiphase). This explains why the dispersion S, which is located at the N-point, appears split and the band bottom at 9 eV, which is located at the Γ-point at $h\nu$=110 eV, remains single. As the photoemission transition determines the primary beam for electron scattering, it restricts the dispersions which appear repeated to those at the N-point. Location at the N-point in momentum space is probably the main cause
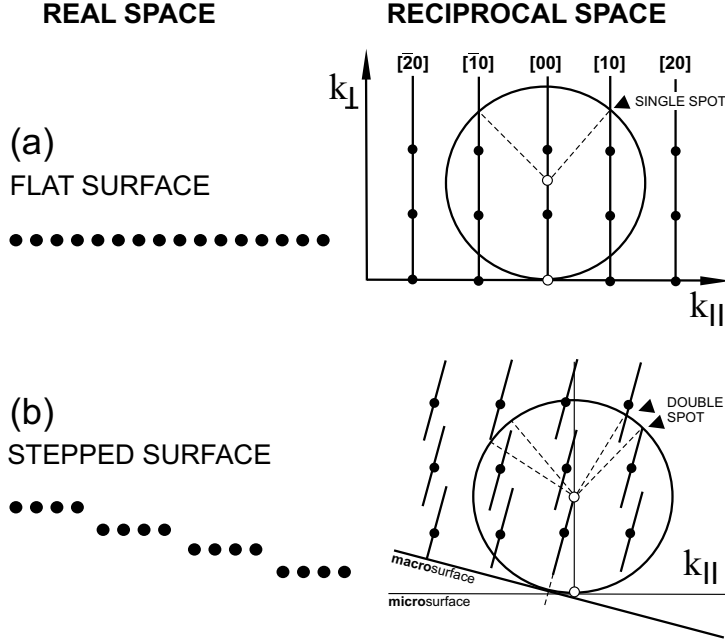
Figure 3.6: Ewald construction for diffraction from ideal flat surface (a) and superlattice of steps (b). In the second case the reciprocal lattice rods for scattering from a vicinal surface are tilted with respect to the microsurface. The figure is taken from Ref. [111].

for the repetition of the band structure and the surface localization may be less important.

In summary, a new surface resonance on W(110) and stepped W(331) and W(551) has been identified at ~ 6 eV binding energy. This feature shows diffraction effects on a large intensity, energy, and momentum scale in agreement with the lateral superlattice translation. The data do not reconcile with an initial state effect in the band structure of the superlattice but can be explained on the basis of electron scattering from stepped surfaces in terms of the LEED formalism. The point of **k**-space where the photoemission transition takes places has been concluded as crucial factor for the observed superlattice effects. The result that the repetition is a final-state effect and that the electron wave function is localized at the microsurface is an important prerequisite for tailoring electronic properties in one-dimensional nanostructures grown on stepped W substrates.

3.2 Lateral electron confinement in Au step-decorations on W($nn1$)

3.2.1 Introduction

The previous section was devoted to superlattice effects in the electronic structure of stepped surfaces. It has been pointed out that either umklapp or lateral quantum-size effects are critical for understanding of their basic electronic properties. These results are significant with respect to the role of vicinal surfaces as supporting substrates for nanostructuring. So far, a considerable number of works is devoted to quantum well states in continuous two-dimensional metallic films [113, 114, 115, 116, 117]. Based on this experience, another type of confined states of even lower dimensionality can be produced. These are so called lateral quantum well states which appear in atomic wires or nanostripes. The nanostripes are typically one atomic layer thick and posses a width of several lattice constant.

They can be prepared on vicinal surfaces employing the step decoration by the adsorbed material. If the width of the step is small compared to the adatom mean free path, nucleation of an epitaxial film typically begins at the step edge [122] in order to maximize number of bonds to the substrate. The width and the periodicity of the nanostripes is controlled by the amount of the deposited adsorbate and by the surface miscut angle, respectively. If quantization in the direction normal to the terrace is supported by the substrate band structure, i.e. an appropriate substrate band gap is available, an additional *lateral* confinement of the electrons propagating perpendicular to the stripe may take place leading to an anisotropic one-dimensional band structure [125]. In this case the quantum stripe is acting as potential well bound by two coordinates: firstly, in the direction perpendicular to the substrate, and, secondly, in the direction perpendicular to the stripe (but parallel to the substrate surface).

Recently, physics of nanowires and nanostripes has been extensively studied. For instance, atomic wires prepared on vicinal Si(111) substrates are attracting huge attention [126, 127, 128]. Chains of Au atoms on Si steps demonstrate a tailored electronic structure in terms of partial band filling [129]. Tuning the wire separation by choosing different periodicity of Si steps one can vary the interaction between the chains and alternate significantly their electronic structure and conductivity [130]. Metallic wires on semiconducting substrates have a potentially great impact on technology, since they have been proposed as the basic elements of computer memory with storage density of Terabit/cm^2 [131, 132].

Some fascinating properties of the nanosized step decoration systems are related to their magnetism [133, 134, 135, 136, 137, 138]. So far, it has been shown that supported atomic chains of magnetic materials exhibit one-dimensional ferromagnetism in contrast to predictions of basic spin-lattice models [139]. In a number of works local magnetic properties of nanostructures have been studied with local probe methods. In particular, an alternating sign of the magnetization of neighboring Fe stripes prepared on vicinal W(110) has been revealed by spin-resolved

STM and attributed to interstep dipolar coupling [140].

The forthcoming Section is devoted to fabrication of nanosystems on the vicinal surfaces W(331) and W(551). The W(nn1) surfaces have step edges (Fig. 3.1) which run along [1$\bar{1}$0] and have a zig-zag profile. This means they are rather open as opposed to the energetically more favorable close-packed edges (like, for instance, at W(145) [123]). In the present work it was found that such disturbed profile affects the growth of the epitaxial film, leading either to the formation of non-uniform stripes or to a polycrystalline adlayer without observable effects of size-quantization. In a variety of experiments it has been established that nanopatterning through the "classical" step-decoration does not work for the W(nn1) substrates. In order to gain ordered metallic nanostructures of Au on W(331) and W(551) several agents must be employed. As it was found, a very particular submonolayer amount of oxygen adsorbed on the vicinal surface is required to control self-organization of Au on top. Another important factor is the temperature. Moderate annealing (500-550°) of 0.6ML of Au deposited on W(331) or W(551) with nearly 0.2 ML of chemisorbed O lead to the formation of a quasi-periodic nanostructure of nail-like clusters, the dimensions of which are defined by the step periodicity of the pure substrate (under "quasi-periodicity" we mean here a uniformity in the nanostructure dimensions and no pronounced lateral periodicity in their arrangement on the substrate). This nanosystem gains a strongly anisotropic one-dimensional electronic structure featuring distinct effects of lateral electron quantization.

In the following, results of a combined study of this system are reported. Because of the significant role of oxygen, the oxidation of W(331) and W(551) has firstly been studied in detail by LEED, STM and photoemission of the chemically sensitive core-levels W4f and Au4f. The geometry of the produced nanostructures was analyzed with STM and LEED, while quantum-size effects in the valence band were probed by angle-resolved photoemission. General conclusions about geometry and mechanism of the self-organization will finally be made. Since both substrates W(331) and W(551) provide qualitatively the same nanostructures, which are defined by the same effects of self-organization, the following report will mainly focus on W(551). The difference to W(331) will be pointed out where it appears.

In order to understand the role of the terraces to greater detail, the electronic structure of Au nanostructures produced on stepped tungsten will be compared to the results of a photoemission investigation of Au films grown on strongly oxidized flat W(110), which is the base plane of steps on W(nn1).

3.2.2 Experimental details

Initially, clean tungsten samples were prepared as described in the previous Section. Then, the surface was oxidized at an elevated temperature of 1100-1200°C and a partial pressure of O_2 of 2×10^{-7}. Afterwards, the oxygen coverage was successively decreased by a number of short thermal flashes of the sample up to 1800°C, during which the temperature was stepped up by 200°C each time. After each treatment the surface geometry was tested by LEED, while its stoichiometry

was probed by photoemission of the W4f core-level. We will refer to the most detailed report in the literature where oxidation of the flat W(110) surface was studied by photoemission of core-levels [141]. Comparing the obtained line shapes of W4f peaks and combining them with the LEED observations, one can unambiguously obtain information on how big the amount of O left on the substrate after each step of annealing is. LEED patterns were in the present work always used as a reference for reproducing the surface. When a coverage of 0.2ML of O was achieved, 0.6ML Au were deposited from a drop melted on a resistively heated tungsten filament. The Au adlayer thickness has been carefully controlled by a microbalance and photoemission of the valence band. Successive annealing at 550°C leads to self-organization of nanostructures, which is the main object of present study.

Details and technical aspects of the photoemission measurements have already been discussed before and can be found in Chapter 1. In the present experiment BESSY beamlines U125 and UE56/1 were employed as a tunable source of photons. Surface verification by STM was done selectively for several oxygen coverages. For details on the STM set-up and on the tip preparation we also refer to Chapter 1.

3.2.3 Results

Characterization with LEED and STM

Results of the surface geometry verification for stepped surfaces by LEED are shown in Fig. 3.7. Fig. 3.7(a) presents the diffraction pattern from clean W(551). The b.c.c. (110) pattern from the plane of terrace is clearly split perpendicular to steps exhibiting a surface reconstruction $p(10{\times}1)$ with a distinct periodicity of steps in the direction [001] of the W lattice (for W(331) this reconstruction is $p(6{\times}1)$). All superstructure notations which are introduced in the following will be referred to the (110) terrace plane for the sake of simplicity. STM measurements of this stepped substrate are reported in Fig. 3.8(a). The distinct topography profile S_1 across the steps is given in Fig. 3.8(d). It reveals an average terrace width $a =$15.8Å.

Because the role of oxygen for the observed self-organization of Au was found to be crucial, additional studies of W(nn1) oxidation were done. Fig. 3.7(b) displays the LEED pattern of an O-covered surface, which has been obtained after a short flash of strongly oxidized W(551) up to 1600° for 5 sec. Annealing at this temperature leaves on the surface approximately 0.75 ML of oxygen which forms a superstructure $p(2{\times}2)$. The exact coverage and type of the superstructure are determined from the shape of W4f photoemission spectra (see Fig. 3.12(a) compared to the data from Ref. [141]). However, the LEED pattern in Fig. 3.7(b) does not clearly reflect the $p(2{\times}2)$ reconstruction, neither is a distinct step-related splitting visible. Multiple spots appear on the lines which run between the major spots of the W(110) $p(1{\times}1)$ pattern. Notably, if the energy of the primary electron beam is varied, the spots are moving along these lines independently from the basic $p(1{\times}1)$ pattern. Such behavior manifests some kind of O-induced *faceting*.

Apparently, information obtained with LEED is not enough to understand the influence of oxygen on the substrate, therefore STM measurements of oxidized W(551) have additionally been performed.
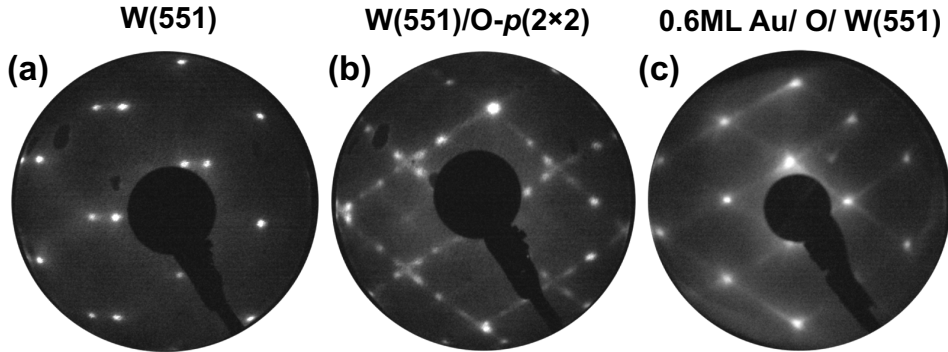
W(551) **W(551)/O-*p*(2×2)** **0.6ML Au/ O/ W(551)**

(a) **(b)** **(c)**

Figure 3.7: Results of the LEED study at a primary electron beam of 65 eV; (a) diffraction pattern obtained from clean W(551) reveals a $p(10\times1)$ periodicity of steps ($p(10\times1)$ for W(331)); (b) pattern measured from oxidized W(551) with $p(2\times2)$ superstructure of O; (c) diffraction from quasi-periodic self-organized nanostructure.

Fig. 3.8(b) reports STM data of W(551)/O-$p(2\times2)$. One can clearly see that the substrate does not maintain any more its initial stepped character, but rather looks like a system of nearly arbitrarily distributed triangular terraces. They are aligned parallel to the direction of steps which is $[1\bar{1}0]$ on W($nn1$). Two short sides with an angle of 110° between them form a corner, which points along [001], i.e. perpendicular to the former terraces. The angle 110° comes obviously from the hexagons of W(110) which form zigzag step edges on vicinal W($nn1$), i.e. the angle between $[11\bar{1}]$ and [111] (see Fig. 3.1). Oxygen is not visible at the parameters of tunneling which have been used. Careful analysis of the terrace dimensions reveals an interesting point: some facets have a different width, however not larger than 32Å, which corresponds to twice the width of the initial steps. This fact, in particular, correlates with the dimensions of the W(551)-$p(10\times1)$ step superlattice. The topographic profile S$_2$ of W(551)/O-$p(2\times2)$ is shown in Fig. 3.8(d) for reference. Despite the fact that W(551)/O-$p(2\times2)$ is not exactly the substrate on which the investigated nanostructure has been produced, the reported results are very important for further understanding of the reasons for self-assembly. Successful preparation of step decorations requires much less oxygen than the 0.75ML in W(551)/O-$p(2\times2)$. As it has already been mentioned, an amount of only 0.2 ML (0.3ML for W(331)) of O is needed to initiate self-organization at elevated temperature. In order to reach this coverage the W(551)/O-$p(2\times2)$ has been further flashed up to 1800° for 5 sec. LEED reveals afterwards a pattern which is identical to the one from clean W(551) (Fig. 3.7(a)), however PES measurements of O1s and W4f core-levels (see Fig. 3.12) still demonstrate the presence of oxygen at the surface. This point means that W(551) has recovered the initial stepped character upon desorption of O and that a minor amount of it most likely remains adsorbed

at the step edges. Because one can judge from LEED that the superstructure of oxygen remnants has the same periodicity as clean vicinal W, the W(551) with 0.2ML of O will be further denoted as W(551)/O-$p(10\times1)$.
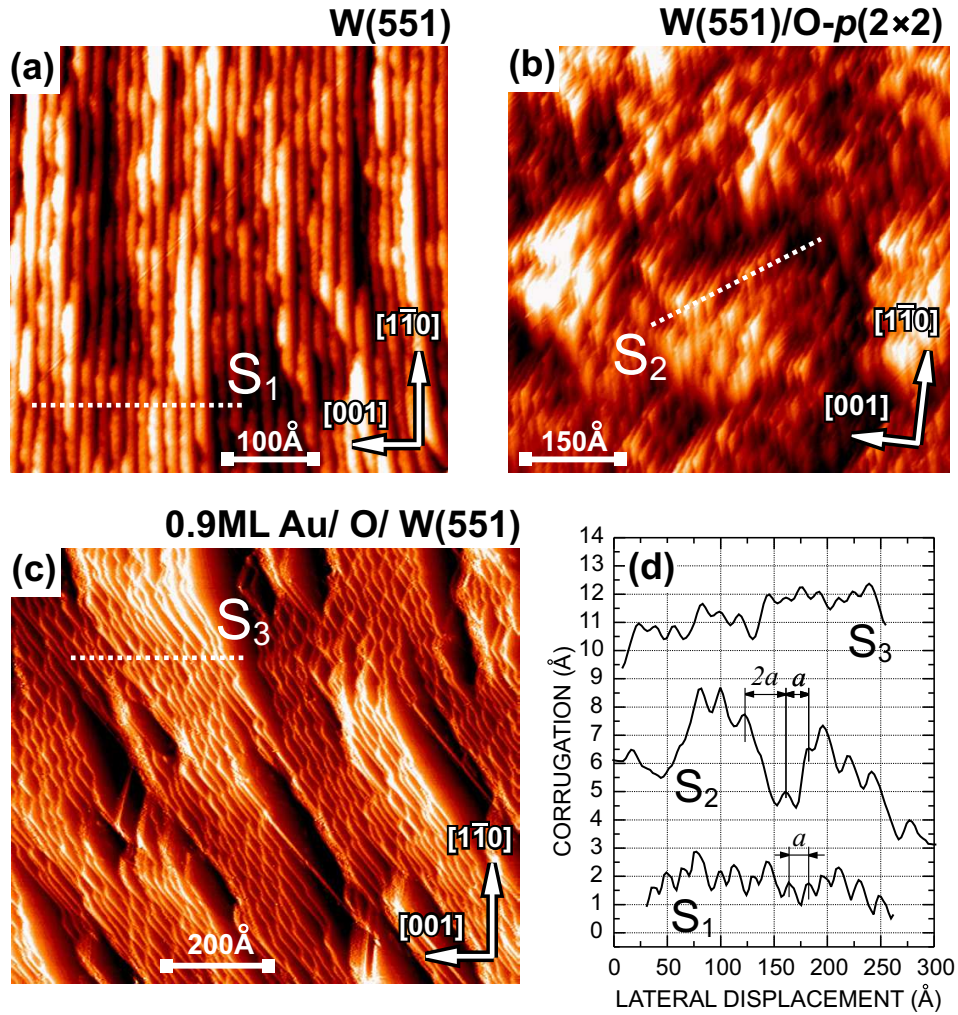

Figure 3.8: STM results; (a) clean W(551) measured at V_{bias}=0.4 V / I_{tunn}=25 nA; (b) O-$p(2\times2)$-induced faceting of W(551) (V_{bias}=1.7 V / I_{tunn}=14 nA); (c) quasi-periodic nanostructure produced from a sub-ML amount of Au deposited and annealed on slightly oxidized W(551) (V_{bias}=0.8 V / I_{tunn}=3.5 nA); (d) characteristic topography profiles S$_{1-3}$ from (a)-(c).

Deposition and moderate annealing at 550°C of 0.5-0.6ML of Au on W(551)/O-$p(10\times1)$ lead to formation of a nanostructure the LEED pattern of which is reported in Fig. 3.7(c). Diffraction shows a well ordered atomic structure, but does not reveal any additional periodicity related to the steps or terraces. In spite of this, STM measurements (in the STM experiment, however, 0.9ML of Au were used but the LEED pattern was identical (Fig. 3.7(c)) reveal fascinating nanostructures of nail-like shape (Fig. 3.8(c)). The *quasi-periodic* character of this nanostructure seen in Fig. 3.8(c) explains why no additional periodicity was ob-

served in the LEED. A distinct topographic section S_3 of the nails is shown in Fig. 3.8(d). One needs to emphasize importance of annealing. Without thermal treatment the LEED pattern obtained from the surface just after deposition of Au was very diffuse, suggesting no ordered crystal structure at all.

Angle-dependent photoemission

Angle-resolved valence band spectra of vicinal samples measured at every step of sample preparation are shown in Fig. 3.9. Spectrum (I) was measured at a photon energy of hν=62 eV from clean W(551) in the direction normal to the microsurface. The angle of normal emission has been calibrated from an analysis of E($\mathbf{k}_\parallel$) dispersions of clean W(nn1). The **E**-vector of the light was parallel to [001] of W and $\mathbf{k}_\parallel$-vectors of the electrons propagating in the direction perpendicular to steps have been probed. The most intense peaks were measured at binding energies of 6 eV (emission from the W sp band Σ_1 [164]) and at 1.2 eV (surface resonance (S.R.) [165]). Spectrum (II) corresponds to the slightly oxidized substrate W(551)/O-p(10×1) before deposition of Au. A minor presence of oxygen is detectable by the signal of O2p at a binding energy of 5.1 eV, which looks like a shoulder in the emission from the sp band of W. Another distinct evidence of the adsorbate is the suppressed surface resonance S.R.

Spectrum (III) in Fig. 3.9 was recorded directly after deposition of 0.6ML Au on W(551) preoxidized with 0.2ML of O. It represents two broad peaks derived from Au d-bands at 6.2 eV and 3.5 eV [118, 119]. The remaining intensity of the tungsten S.R. is evidence of a sub-ML coverage. The normal emission spectrum (IV) corresponds to annealed Au on W(551)/O-p(10×1). One can see that peaks of d-bands are now much sharper, which indicates enhanced ordering of the atomic structure. In addition, several new, although not very intense peaks appear between binding energies of 1.5 and 0.5 eV. Note that the S.R. is completely missing, which, in particular, means adsorbate- and temperature-induced structural changes in the W substrate itself. The most interesting effect, however, appears in the spectra measured for *off-normal* emission. Spectrum (V) in Fig. 3.9 has been measured for an emission angle of 3°. It features a very intense peak of a novel state at 0.6 eV binding energy. The same effect appears as well for annealed Au on oxidized W(331), however the maximum of this peak appears at an emission angle of 4°. A similar electronic state appears also in the flat system Au/O/W(110) but demonstrates particularly different properties, as will be discussed below.

In order to probe the behavior of this state in detail, **k**-vector dependent spectra were measured. Results are reported in Fig. 3.10. Fig. 3.10(a) and 3.10(b) present angle-resolved photoemission of the electrons propagating perpendicular to the direction of steps ($\mathbf{k}_\parallel \parallel$ [001]) of W(331) and W(551), respectively. One can observe that the state at 0.6 eV disperses in a parabolic way downwards (dashed line) and is shifted off the normal emission and split into several discrete levels (vertical solid lines) with an energy separation of about 0.5 eV. Extracted dispersions E($\mathbf{k}_\parallel$) of this state are presented in Figs. 3.11(a) and 3.11(b) where they are additionally illustrated by the grayscale intensity plots (Figs. 3.11(d) and 3.11(e)) constructed
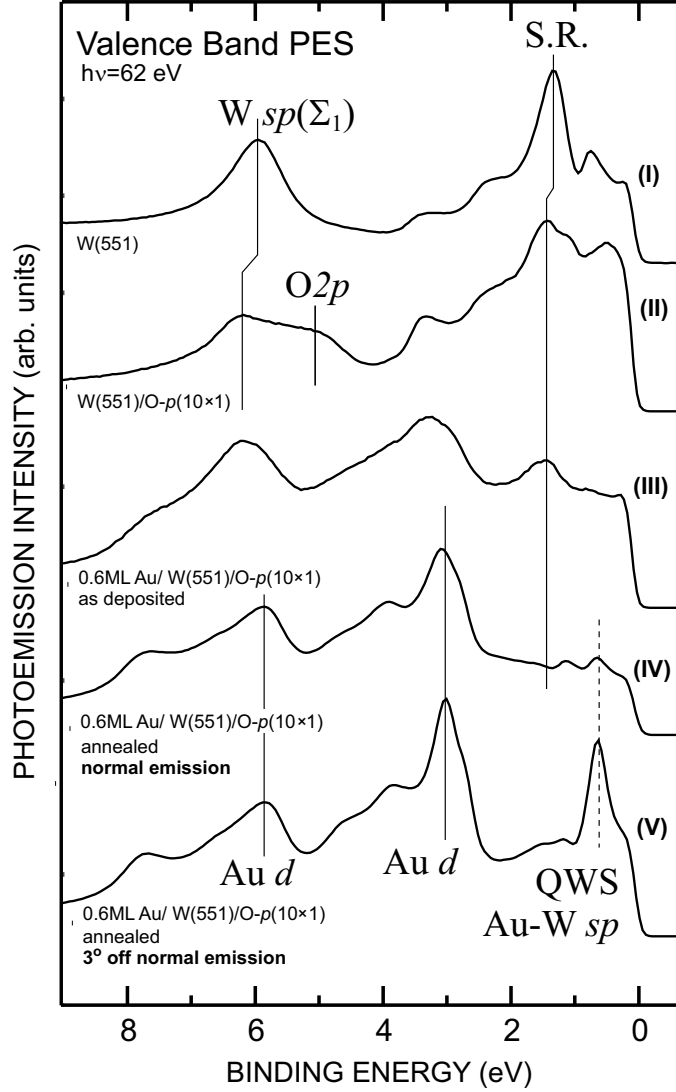
Figure 3.9: Photoemission spectra of the valence band, measured at different stages of sample preparation.

from the spectra displayed in Fig. 3.10. Note that angular shifts of dispersions are different for W(331) and W(551). A precise analysis of the data points reveals that the momentum shift of this band is Δk_{331}=0.29 Å^{-1} in the case of W(331), while for W(551) this value is Δk_{551}=0.19 Å^{-1}. Fig. 3.10 also presents results of a comparative study. In particular, angle-dependent spectra of clean stepped W(331) which has neither Au nor O on it were recorded (Fig. 3.10(d)). The absence of any peaks at binding energies around 0.6 eV shows that the state observed at this energy in Fig. 3.10(a) and 3.10(b) is definitely related to Au. In order to check any possible influence of a lateral step periodicity on the quantization of the 0.6 eV band, the E($\mathbf{k}_{\parallel}$) dispersion of 0.6ML Au/ W(nn1)/O-p(10×1) has also been measured in the direction parallel to the initial steps of the W substrate ($\mathbf{k}_{\parallel} \parallel$ [1$\bar{1}$0]). The spectra are presented in Fig. 3.10(e). Surprisingly, no peaks at 0.6 eV
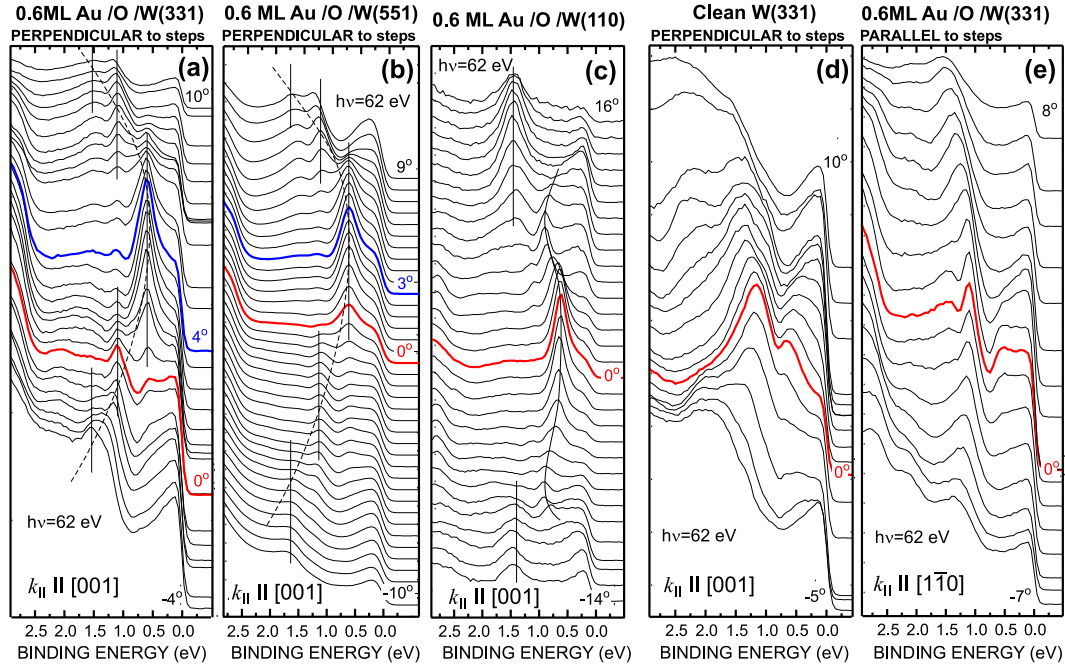
Figure 3.10: Angle-dependent photoemission from the lateral quantum well state in Au/W(nn1)/O which is detected at 0.6 eV binding energy; (a) photoemission of electrons propagating perpendicular to the steps of W(331); (b) the same as (a) but for W(551); (c) "reference system": dispersion of 0.6 eV state in the Au film on flat W(110); (d) comparative study - photoemission in the same direction as for (a) and (b) but from clean W(331); (e) spectra of photoelectrons propagating in the Au nanostructure produced on W(331) along the steps. The direction of normal emission is defined as 0° in the figures.

have been detected at all.

A very interesting behavior is seen for the "reference" system Au on flat oxidized W(110). While the state at 1.4 eV binding energy has almost no dispersion (Fig. 3.10(c)), the peak at 0.6 eV disperses downwards up to 0.9 eV (Figs. 3.10(c) and 3.11(f)). Assuming that the origin of this electronic state is the same as for the corresponding band in the Au nanostructure on W(nn1), one can conclude that we deal with an energy gap opening between 0.9 eV and 1.4 eV.

Core level photoemission

It is well known that photoemission of core levels can provide information on the chemical environment of atoms in the bulk or at the surface of a crystal [142, 143, 144, 162]. Analysing energy shifts of spectral components through decomposition of the original spectra, one can obtain a lot of qualitative and quantitative information on the types of chemical bonding in the solid. Knowledge of the surface chemistry in such a complicated system like Au/ W(nn1)/ O is strongly required to understand the observed phenomena of self-organization.
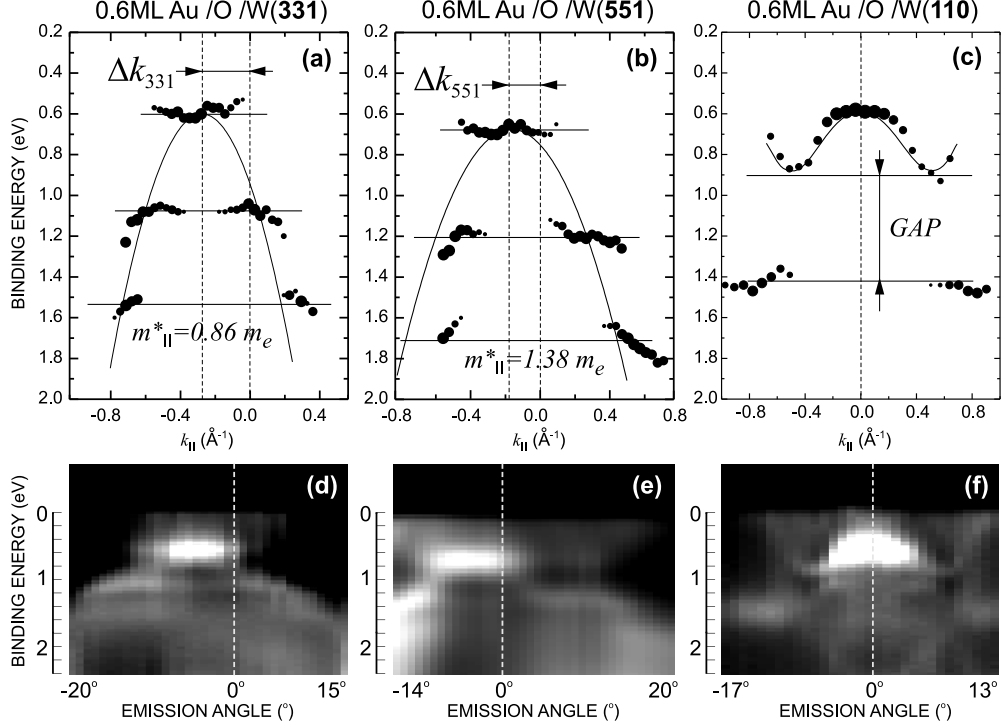
Figure 3.11: $E(\mathbf{k}_{\parallel})$ dispersions of lateral quantum well state extracted from Fig. 3.10 for W(331) (a), W(551) (b) and W(110) (c). A parabolic fit of band dispersion is shown as solid line; (d)-(f) grayscale intensity maps constructed from the spectra in Fig. 3.10 are shown *vis-à-vis* the plotted dispersions.

Characteristic spectra of core levels $W4f_{\frac{7}{2}}$, $Au4f_{\frac{7}{2}}$ recorded at different stages of the W(551) preparation are presented in Fig. 3.12(a) and 3.12(c), respectively. Simple least square fits using Voigt functions was used in order to gain the spectral components [247]. Original data points are represented in Fig. 3.12 as open circles. Results of the fits are shown as solid curves. Spectrum (I) in Fig. 3.12(a) corresponds to the clean substrate W(551) and features two intense well resolved peaks: photoemission from bulk at 31.4 eV and a surface-induced component at 31.09 eV. Spectrum (II) has been measured from W(551) with 0.75 ML of O (W(551)/O-$p(2\times2)$). The exact amount of oxygen was found from the shape of W4f core level, its spectral content and comparison to the literature [141]. In the spectrum of W(551)/O-$p(2\times2)$ a surface induced peak is shifted significantly towards the bulk one, which is an evidence of high adsorbate coverage. In addition, two spectral components *Ox2* (31.77 eV) and *Ox3* (32.13 eV) are well pronounced. They correspond to 2-fold and 3-fold oxidation of W atoms being fingerprints of the O $p(2\times2)$ superstructure on W(110) [141].

Spectrum (III) in Fig. 3.12(a) was measured from the slightly oxidized W(551)/O-$p(10\times1)$ which was used as a substrate for deposition of Au. As it has already been mentioned, LEED measurements of this surface have shown diffraction patterns which were identical to the one from clean W(551) (i.e. $p(10\times1)$ superlattice).
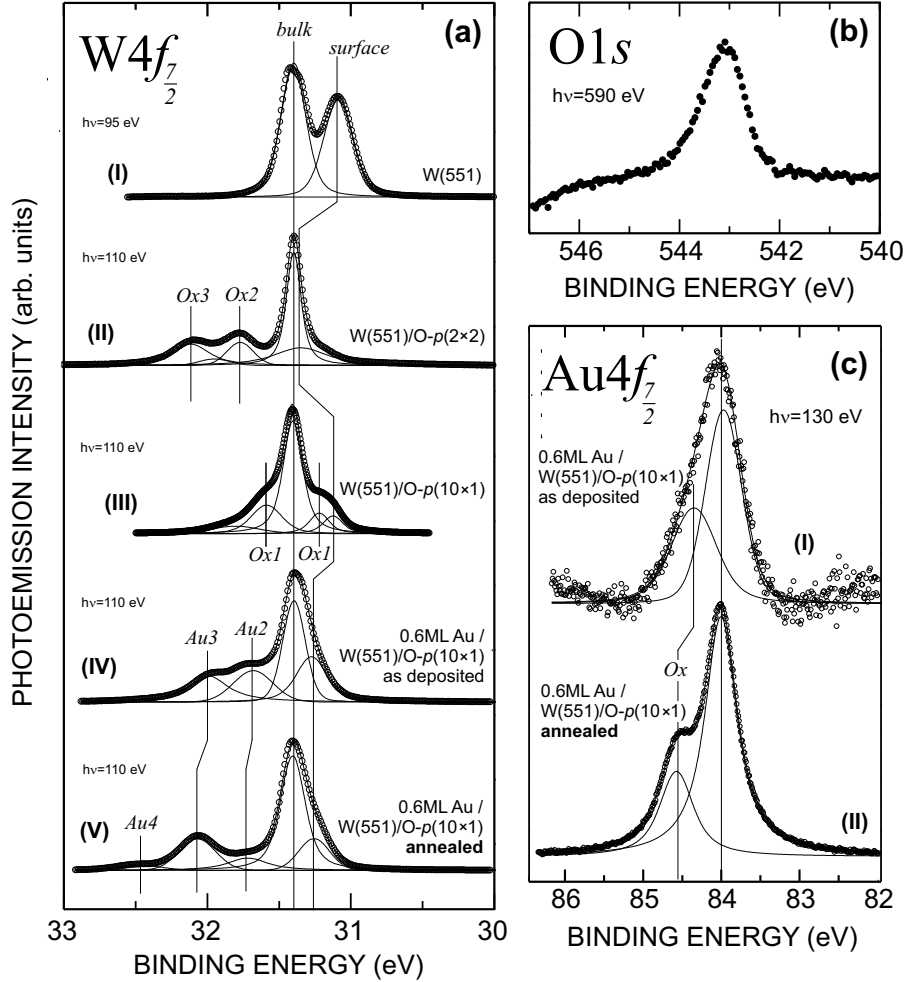
63

Figure 3.12: Core level study; (a) Photoemission from W4f at different stages of sample preparation; (b) Spectroscopy of O1s reveals presence of oxygen at the surface even after nanostructure development; (c) Spectra of Au4f demonstrate strong oxidation of gold upon self-organization.

On the other hand, spectrum (III) provides an evidence of oxygen, the coverage of which is determined as 0.2 ML. Two additional components which are marked as *Ox1* (31.59 eV and 31.21 eV) denote photoemission from W atoms with 1-fold oxidation state [141]. In order to assure that the shape of the core level in spectrum (III) is truly determined by chemisorbed oxygen, XPS measurements of O1s were also performed. The spectrum obtained (Fig. 3.12(b)), taken at hν=590 eV, fully confirms our assumption.

The last two spectra in Fig. 3.12(a) reflect the chemistry of the W substrate with 0.6 ML of deposited Au before (IV) and after (V) annealing at 550°C. They exhibit a nontrivial spectral lineshape, resembling very much spectrum (II) which corresponds to W(551) with 0.75 ML arranged in the $p(2\times2)$ superstructure. Because it was established that the amount of oxygen at the surface is significantly less than 0.75 ML, the corresponding spectral components at 31.68 eV and 32.0

eV can only be called Au-induced and will be further denoted as $Au2$ and $Au3$, respectively. It is interesting that the chemical reaction which causes the appearance of these shifted peaks already takes place at room temperature. After moderate annealing which fully develops the quasi-periodic structure of step-arranged nanoclusters (Fig. 3.7(c) and Fig. 3.8(c)), the components $Au2$ and $Au3$ experience a minor shift of less than 0.1 eV towards higher binding energies, but their intensity ratio changes drastically. Peak $Au3$ becomes dominating while $Au2$ almost vanishes. Furthermore, a new spectral component $Au4$ appears at a binding energy of 32.48 eV. The origin of this chemical shift will be later discussed in more detail.

Since strong chemical shifts appear for W4f, it would be appropriate to check Au core levels for similar effects. The Au4$f_{\frac{7}{2}}$ spectra measured before (I) and after (II) annealing are presented in Fig. 3.12(c). A well resolved component Ox appears at a binding energy of 84.36 eV for non-annealed sample and shifts to 84.62 eV after annealing and development of the nanostructure. This is direct evidence that Au atoms are strongly involved in the chemical interactions which likely control self-organization.

3.2.4 Discussion

Quantum-size effects

Let us start the discussion from an analysis of quantum-size effects observed in the dispersion of the pronounced state which appears at 0.6 eV binding energy away from normal emission (Fig. 3.10(a,b) and Fig. 3.11). Summarizing briefly the experimental results, it has been mentioned that no peaks at 0.6 eV have been detected in the photoemission from the valence band before the final step of the preparation - annealing and development of self-organized nanostructures (Fig. 3.7(c) and Fig. 3.8(c)). On the basis of this point we argue that the 0.6 eV state is related explicitly to the produced nanostructure (not to Au alone because angle-resolved spectra obtained from the sample with non-annealed gold do not reveal any traces of this state). This band demonstrates a large parabolic dispersion downwards in the range from 0.6 eV to 2.5 eV which is evidence for an sp-electronic state with negative effective mass. In addition, the band appears quantized to constant energy levels (0.6 eV, 1.07 eV and 1.54 eV for W(331), and 0.67 eV, 1.2 eV and 1.72 eV for W(551)), featuring approximately the same energy splitting of $\sim$0.5 eV for both W samples. The most intense peak at 0.6 eV (which we call "0.6 eV state" in the text) appears at just the energy level of a confined electron with quantum number $N = 1$. Dispersions of this state are shifted in **k**-space by Δk_{331}=0.29 Å^{-1} in the case of W(331), and by Δk_{551}=0.19 Å^{-1} for W(551). Another important fact observed is that quantization can be distinguished only for the electrons with $\mathbf{k}_\parallel \parallel [001]$ i.e. propagating perpendicular to the initial steps of W($nn1$). Angle-resolved photoemission of electrons moving parallel to the steps does not demonstrate the existence of this band even when the nanostructure is fully developed (Fig. 3.10(d)). Summarizing these evidences one can unambiguously describe the observed effect as lateral quantization of an sp-electron

band which newly appears in the nanostructure of clusters after its oxygen- and temperature-induced self assembly. Confinement in the direction perpendicular to the (110)-face of W is provided by interfacial scattering [156, 81, 83].

The idea of lateral quantization is additionally confirmed by a comparative study of Au on flat O/W(110). As shown before (Figs. 3.10(c) and 3.11(c)) its electronic structure possesses the same band at 0.6 eV, which shows, however, dispersion and demonstrates only partial confinement with characteristic "leaky" behavior [101] and an energy gap opening between 0.9 and 1.4 eV (Fig. 3.11(c))

One can now try to analyse the electronic structure of this lateral sp-electron QWS in detail for vicinal substrates. Firstly, it is important to relate $\mathbf{k}$-vector shifts Δk_{551} and Δk_{551} to real-space crystallographic parameters of the step-arranged nanostructure of clusters. According to the definition of the reciprocal lattice ($\frac{2\pi}{D} = \Delta k$) for Δk_{331}=0.29 Å^{-1} one gains the real-space distance D$_{331}$=21.6 Å and for Δk_{551}=0.19 Å^{-1} one obtains D$_{551}$=32.9 Å. These values are very well consistent with the double step periodicity of the substrates W(331) (D$_{331}$ =19.6 Å) and W(551) (D$_{551}$ =31.6 Å) (Fig. 3.1). This, in particular means, that the initial periodicity of the vicinal W surfaces strictly defines the dimensions of the produced nanostructures and affects their electronic properties. Let us now try to describe lateral quantization quantitatively and evaluate nanostructure dimensions from the observed energy splitting (Fig. 3.11). Energy levels of confined electrons can be related to parameters of the quantum well on the basis of an approach used for the description of surface state quantization on vicinal Au(111) [167, 168, 169]. Considering a nanowire as infinite one-dimensional potential well of width L the binding energies of confined electron states are given by the equation:

$$(3.2) \qquad\qquad E_N = E_F - E_0 + \frac{\hbar^2 \pi^2}{2m_\parallel^* L^2} N^2$$

The in-plane effective mass $m_\parallel^*$ of the electron can usually be determined from the dispersion measured in the direction parallel to quantum wires, stripes, or atomic chains. However, the dispersion in the direction parallel to the steps of W($nn1$) is absent since the 0.6 eV state was not detected (Fig. 3.10(d)). Therefore this method is not available. The only way to find out the effective mass is to determine parabolic dispersions from an analysis of QWS energy levels. Maxima of intensity have been determined in every set of data points in Fig. 3.11 and a parabolic fit has been performed. The obtained dispersions (solid line) reveal effective mass values $m_\parallel^*$=0.86 m_e and $m_\parallel^*$=1.38 m_e for W(331) and W(551), respectively (m_e denotes mass of the free electron). Considering that the QWS energy splitting is the same for both substrates and equal to (0.5 ± 0.05) eV, the formula Eq. (3.2) gives L_{331}=(16 ± 2)Å and L_{551}=(10 ± 2) Å. These results are reversed in respect to the original width of W(331) and W(551) steps. The most probable reason of such contradiction may be hidden in the model itself. The point is that Eq. (3.2) is only justified for truly one-dimensional systems like nanowires or nanostripes, because it deals with a potential well which is *infinitely* long in one direction.

However, the STM data in Fig. 3.8(c) clearly displays that the nanostructures are not one-dimensional but rather are two-dimensional clusters.
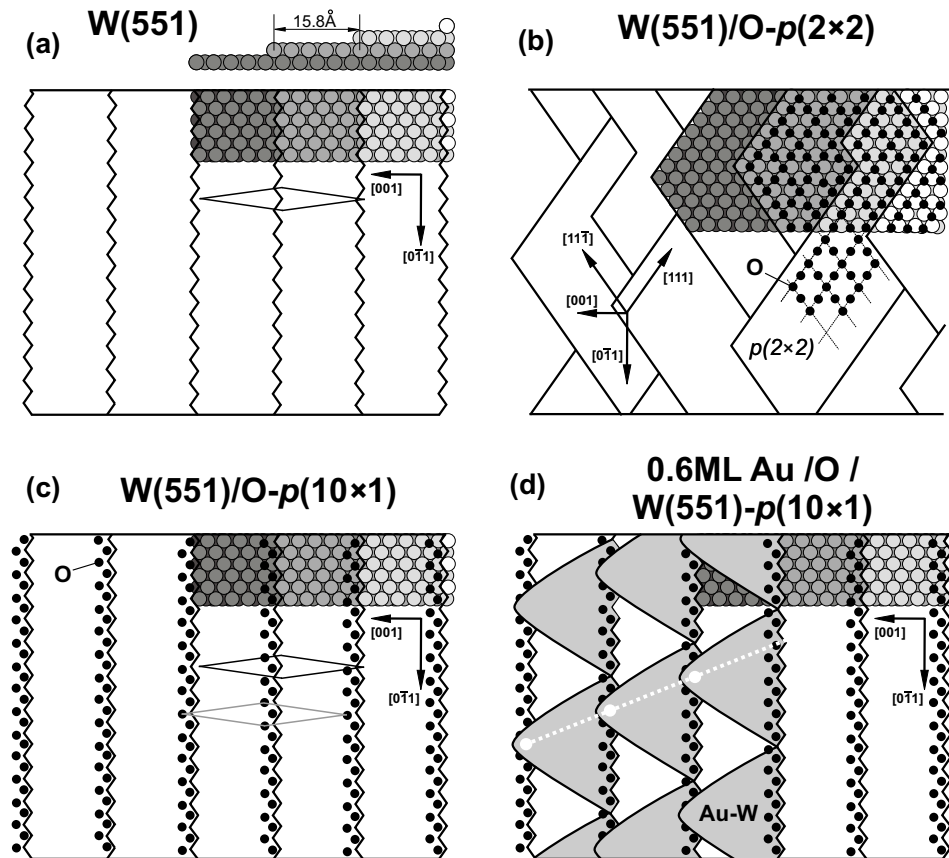

Figure 3.13: Structural models; (a) W(551) with zig-zag like profile of the step edge; (b) oxygen-induced faceting of W(551) at 0.75 ML coverage, step edges are now aligned to the symmetry axis of the O-$p(2\times2)$ superstructure; (c) 0.2ML of oxygen, predominant adsorption at the step edges; (d) possible arrangement of Au-W alloyed clusters.

The role of oxygen and surface alloying

Let us now consider the crystallography and formation of the nanostructures. The stepped substrate morphology is illustratively shown in Fig. 3.13. Fig. 3.13(a) displays stepped W(551) with ideal geometry. The edge profile is outlined with a zigzag line. The step periodicity of this vicinal surface is given by the double of the width of a terrace: the surface lattice of step-reconstruction is marked as elongated rhombus. The inset in the top-right corner comments on the atomic layout of the steps (the height is specified by different gradations of gray).

There remains a very important question. What exactly are the structural changes of W(551) under the influence of oxygen? It has already been concluded from LEED (Fig. 3.7(c)) and STM (Fig. 3.8(b)), that a W($nn1$) stepped substrate thermally oxidized with 0.75 ML of O becomes faceted in triangular terraces of different dimensions. As spectroscopy of the W$4f$ core level (Fig. 3.12(III)) reveals in comparison to the literature on W(110), O forms a $p(2\times2)$ superstructure. This, in particular, leads to the structural model of W(551)/O-$p(2\times2)$ shown in Fig. 3.13(b). It is known that rows of oxygen atoms in the $p(2\times2)$ and $p(2\times1)$ reconstructions are aligned parallel to [111] and [11$\bar{1}$] directions of the W lattice [152, 153]. It appears that chemisorbtion of O causes an extensive rebuilding of W steps through atomic transport and formation of favorable close-packed edges the direction of which coincides with the alignment of oxygen rows. In fact, it has been shown in earlier theoretical studies of terrace energetics on W(110) that formation of steps of W($nn1$) (which are parallel to the direction [1$\bar{1}$0]) are not energetically favorable, having almost twice of the formation energy of terraces with close-packed profile [145]. In the presence of the $p(2 \times 2)$ matrix of oxygen (which likely tends to align edges of steps to its own lattice) this energy increases drastically, causing a realignment of tungsten to closed-packed terrace edges. The next question is what happens at lower oxygen coverage? According to LEED observations, which reveal that 0.2ML of O on W(551) does not destroy the step periodicity (the LEED pattern is the same as from clean W(551) (Fig. 3.7(a))), it would be fair to assume that low amounts of oxygen are adsorbed at the step edges only, exactly reproducing the (10×1) periodicity of W steps, as shown in Fig. 3.13(c). On the other hand, taking into account the tendency of W($nn1$) terraces to gain closed-packed edges under the influence of oxidation, it is not difficult to imagine, that already at 0.2ML of O the edge profile will be disturbed, yet keeping the average terrace width unchanged. This local edge reconstruction is obviously the basic factor which determines the Au-W interaction and controls the observed self-organization.

The kind of underlying interaction can be clarified from W$4f$ spectra measured after deposition of sub-ML amounts of Au. The spectrum (IV) in Fig. 3.12 obtained from 0.6ML Au/ W(551)/O-$p(10\times1)$ exhibits two spectral components $Au2$ (31.68 eV) and $Au3$ (32.0 eV) shifted towards higher binding energies. The appearance of these shifted peaks unambiguously manifests a chemical interaction between Au and W, accompanied by a substantial electron transfer. This is an evidence of metallic bonding between these two elements which takes place as result of *surface alloying*. Although, in the bulk Au and W do not alloy [146], at the surface gold atoms can be exchanged with atoms of tungsten in the first monolayer [181, 147]. Let us remember that minor doping of the W($nn1$) substrate with O is a crucial factor for the observed phenomenon of Au-W chemical interaction: no chemical shift in W$4f$ has been observed upon Au deposition on a carefully cleaned substrate. Considering the role of oxygen, one can assume that O atoms adsorbed at step edges cause a buckling of the edge profiles in a way that other crystallographic planes become "open" allowing Au atoms to penetrate into the first monolayer of the W terrace. Note that, as spectrum (IV) in Fig. 3.12 shows,

this process takes place already at room temperature. A very important point is that the spectrum (IV) in Fig. 3.12 strongly resembles spectrum (II) measured from oxidized W(551) without Au. Analogously to peaks $Ox2$ and $Ox3$ from spectrum (II), which corresponds to 2- and 3-fold oxidation states of W, respectively, the components $Au2$ and $Au3$ can be attributed to chemical states in an alloy, where, for example, the tungsten atom is surrounded by 2 and 3 atoms of gold, respectively. The spectral lineshapes of W4f measured from annealed 0.6ML Au/ W(551)/O-p(10×1) (spectrum (V) in Fig. 3.12) with fully developed Au nanostructure, further supports the idea of surface alloying. As one can see in spectrum (V), the component $Au2$ almost vanishes, while $Au3$ even increases moderately. This effect reflects increased coordination numbers of W atoms (with respect to Au) as a result of extensive penetration of gold into the lattice of tungsten. In addition to that, a new component $Au4$ appears in spectrum (V) at 32.49 eV, which should likely be attributed to penetration of Au even into the second atomic layer of W substrate. Significant improvement of the surface lattice is confirmed by LEED which shows well-ordered and uniform pattern with sharp spots (Fig. 3.7(c)). One more proof of alloying can be found in valence band photoemission. Comparing spectra (III) and (IV) in Fig. 3.9 which were measured from annealed and non-annealed Au/ W(551)/O-p(10×1), respectively, one can clearly note an overall vanishing of the tungsten surface resonance S.R. at 1.2 eV after annealing. This is convincing evidence of significant structural changes in the first monolayer of the W substrate.

Notably, in the case of flat substrate W(110), surface alloying can also be achieved, as confirmed by photoemission of core levels (the data is not reported here). But as it has already been mentioned, an oxygen coverage increased to 1ML and an elevated annealing temperature of 850°C are required for that purpose. This fact suggests the role of the steps on W(nn1) as "catalysts" of atomic exchange.

Structural model

Answering the question of how surface alloying causes self-organization of nanostructures, one can assume a strong and anisotropic stress which appears in the topmost layer of the tungsten substrate upon penetration of gold. At elevated temperatures the atomic mobility increases, so that the potential barriers of lateral diffusion can be overcome leading to a structural rearrangement which complies with decreasing the potential energy of the atomic system. Most likely, Au atoms slide W atoms apart and occupy hourglass-like areas between them (see atomic structures in Fig. 3.13 and Fig. 3.1) forming internal chains aligned to [111] and [11$\bar{1}$] directions of W lattice - similar as oxygen does in the p(2×2) superstructure (Fig. 3.13(a)). This idea is confirmed by the LEED measurements. The LEED pattern from Au nanostructures (Fig. 3.7(c)) somehow resembles the one from W(551)/O-p(2×2) (Fig. 3.7(b)): blurred lines corresponding to [111] and [11$\bar{1}$] directions of the W crystal which interconnect major spots are distinct for both images.

One can assume an important role of the oxygen doping for the development

of the nanostructure. As the surface alloying between Au and W is initiated, O adsorbed at the step edges (Fig. 3.13(c)) is likely substituted by atoms of Au and starts to diffuse laterally over the steps, causing reduction of the potential barriers of the lateral atomic diffusion. Indeed, in a number of works [148, 149, 150, 151] oxygen has been proven an efficient surfactant.

A simple structural model of alloyed nanostructures is shown in Fig. 3.13(d). Nail-like nanoclusters of a Au-W compound are sitting on the terraces of the W(nn1) substrate forming a quasi-periodic matrix. The sketch in Fig. 3.13(d) does not reflect this quasi-periodic character. In fact, it should be expressed either as different shifts between the nails or in their periodically modulated width in the direction along terraces. This would explain why any detectable secondary periodicity is absent in the LEED pattern (Fig. 3.7(c)).

It is now time to discuss how the proposed structural model can explain the quantization of the 0.6 eV state in the valence band. Since neither W nor Au alone lead to any peaks at this binding energy before annealing (Fig. 3.9), the 0.6 eV state can unambiguously be identified as part of a *new band of an ordered Au-W surface alloy.* It is hoped that more information about the nature of this state can be delivered as a result of band structure calculations on the basis of this model which will be an interesting topic of further research. The next question is how the model can explain the strong anisotropy found in the electronic structure measured parallel and perpendicular to the terraces of W(nn1). Considering the Au-W compound rather as a matrix of arranged clusters, than a one-dimensional step decoration (which was rejected based on the failure of one-dimensional theoretical description in terms of Eq. (3.2)) and assuming a general geometry of clusters as proposed in Fig. 3.13(d), one arrives at a rather realistic model. Variable dimensions of alloyed clusters in the direction [0$\bar{1}$1] of W(nn1) steps can explain the absence of the 0.6 eV alloying-induced band of sp-electrons dispersing in this direction. As for the direction perpendicular to the steps, this means that one has to assume a greater uniformity in the cluster width as well as partial overlapping of their valence band wave-functions in the region of the substrate step edge (as shown in Fig. 3.13(d)). The last point, in particular, will provide the existence of 0.6 eV band based on propagation and scattering of sp-electrons between the nails, leading to the appearance of characteristic lateral QWS's in the 6 eV band (Fig. 3.9(V) and Fig. 3.11). If one considers geometry and positions of nails on steps as proposed in Fig. 3.13(d), it comes out that electrons might propagate in the nanostructure not exactly perpendicular to the terrace, but rather at different azimuthal angle, as shown by white the dotted line in Fig. 3.13(d). In fact, experiments confirm this idea. A maximum of intensity and sharpness in the spectra of lateral QWS's has been indeed achieved for an **E**-vector of the light the azimuthal angle of which was ∼30° away from the direction perpendicular to the steps.

In the case of Au on flat oxidized W(110) no significant anisotropy has been seen in the dispersions of the 0.6 eV state. The band structure measured for the electrons propagating along [001] of W crystal (Fig. 3.11(c)) was found to be very similar to the one mapped along the [1$\bar{1}$0] direction (not presented). This observation lends further credit to the idea that clusters and steps are the origin

of the observed lateral quantum-size effects.

One more question stays open: what is the reason of the observed difference between effective masses of the electron in the alloyed nanostructures prepared on W(331) and W(551) (Fig. 3.11)? It can be assured that adsorbed oxygen is responsible. As it has been established by spectroscopy of the O1s core level (Fig. 3.12(b)) that the concentration of oxygen at the surface does not change after annealing of the sample and development of the alloyed nanostructure. On the other hand, looking at photoemission spectra of the Au4f core level (Fig. 3.12(c)) one clearly sees a strong chemical shift Ox. Because this shift appears at higher binding energies, it cannot be attributed to electron exchange between Au and W, which was the reason for shifts in W4f (Fig. 3.12(a)). Should the same type of chemical bonding be claimed for both effects, the shifts must appear in the directions *opposite* to the main emission line. This, in particular, means that the chemical shift in Au4f is determined by another type of interaction: partial oxidation of gold. Presumably, upon annealing, oxygen migrates away from the step edges, uniformly penetrates in every alloyed cluster and forms its own sub-lattice as a result of selective oxidation of Au atoms. These atoms change their charge states introducing a perturbation for electrons propagating across the nanostructure. As it has been mentioned in the description of experimental details, for W(331) and W(551) different amounts of O are needed in order to initiate self-organization. Therefore there will be different concentrations of oxidized Au and, correspondingly, different perturbation of the crystal potential resulting in different values of the effective mass. Summarizing the facts discussed above one can be assured that the self-organized Au-W nanostructures cannot be considered as simple step decoration of Au on W(nn1). It is rather a complicated compound of three elements: $Au_xW_yO_z$. As for the exact stoichiometry of this surface alloy, one can assume concentrations from structural models shown in Fig. 3.13. In the case of W(551) it is likely to be $Au_3W_5O_1$, while for W(331) the most probable formula is $Au_3W_6O_2$.

It is useful to relate the latter conclusions to a number of works, devoted to the oxygen-mediated growth of epitaxial metallic films. O has been known as surfactant for a long time [148, 149, 150]. Recently the growth of Cu on oxygen doped Ru(0001) was investigated in detail by STM [151]. Since the electronic and the atomic properties of Cu and Ru to some extent are similar to the ones of Au and W, the obtained results are interesting for comparison. It has been shown, that a sub-ML amount of oxygen (0.2–0.6 ML), preadsorbed on Ru(0001) is able to switch the growth of Cu at elevated temperatures from multilayer to layer-by-layer by reducing potential barriers of atomic migration. Moreover, O always stays "floating" at the surface of the Cu film, being penetrated into the first monolayer and forming an ordered alloy with Cu atoms: $Cu_2O(111)$. The explanations assumed here are fully in agreement with these experiments. Since the produced nanostructure Au/O/W(nn1) is only one monolayer thick, oxygen can exactly in the same way incorporate itself inside the alloyed clusters and form its own sublattice and bond to Au atoms. On the other hand, it should be kept in mind, that oxygen works not only as surfactant, but, actually, induces the self-

organization by initiating the Au-W surface alloying at the local reconstructions of the step edges.

3.2.5 Concluding remarks

In summary, quasi-periodic nanostructures with unique anisotropy in their electronic properties have been discovered as a result of Au deposition on slightly oxidized W(551) and W(331) followed by moderate annealing. The surface geometry was studied by LEED and STM measurements.

The comparative study has established that adsorbed oxygen and elevated temperature are *compulsory* factors of self-organization. Photoelectron spectroscopy of the valence band in normal emission revealed the appearance of a new electronic state at 0.6 eV binding energy, which is distinct neither to Au nor to W alone. Band dispersions $E(\mathbf{k}_\parallel)$ of this state measured with angle-dependent photoemission have shown that in the direction nearly perpendicular to the steps of W($nn1$) this state largely disperses downwards and appears quantized into constant energy levels, while in the direction parallel it was not detected at all. Photoelectron spectra of W$4f$ and Au$4f$ core levels have revealed that strong chemical interactions control the self-assembly of the nanostructures. In particular, it was established that minor doping of W($nn1$) by oxygen forces Au to alloy with the topmost atomic layer of tungsten. Oxygen-activated step edges were found to be the "catalysts" which initiate and stimulate Au-W atomic intermixing. Anisotropic stress, which appears as a result of such alloying is assumed to be responsible for the formation of the arranged clusters of the Au-W compound. Because strong chemical shifts have been observed in Au$4f$ spectra, incorporation of O into the lattice of the alloy, accompanied by partial oxidation of Au has been concluded. The peak at 0.6 eV was identified as originating from an intrinsic band of the Au-W compound.

As a final remark, the reported experiment is an extremely clear illustration of how important it is to combine different analytical methods in order to understand the nature of particular physical phenomena. It the present case there is a very strong interplay between electronic and atomic properties of the produced nanostructures. The understanding of this interplay was found only by using two experimental techniques in combination: STM for surface imaging and ARPES for mapping of the band structure.

3.3   Summary of conclusions

Chapter 3 can be summarized as follows. Angle resolved photoemission from flat W(110) and stepped W(nn1) has revealed an electronic state at 6 eV binding energy never observed before. This state is identified as surface resonance localized on the terrace microsurface. In the photoemission from stepped W(nn1) this feature appears in off normal (with respect to the microsurface) emission being symmetrically shifted in **k**-space by half of the Brillouin zone of step superlattice. Such behavior is caused by electron diffraction in the final state of photoemission.

It was established that stepped W(nn1) substrates can serve as template for self-organization of quasi-periodic Au nanostructures when two factors are provided: submonolayer amount of chemisorbed oxygen and elevated temperature. The produced nanostructure was found not to be purely of Au, but a complex Au-W surface alloy where Au atoms are partially oxidized. It is not truly one-dimensional, as might be expected for step decorations, but a system of nail-like clusters. This alloyed nanostructure features a novel electronic band at 0.6 eV binding energy. In **k**-space this band is shifted away from the microsurface normal by a reciprocal vector of step superlattice and appears split into constant energy levels as a result of lateral quantization in the cluster.

Chapter 4

Self-Organization on Large-Scale Surface Reconstructions

The preceding part of this Thesis dealt with nanostructures produced by typical techniques of self-assembly. In particular, in Chapter 2 which is devoted to quantum-size effects in thin films, a two-dimensional Ag overlayer has been epitaxially grown on the flat substrate Ni(111). Chapter 3 was concerned with lateral electron confinement in step decorations on vicinal W(110) surfaces. The common feature of both experiments is that the dimensionality of the self-assembled nanostructures repeats the dimensionality of its supporting substrates: it was two-dimensional in the case of flat Ni(111) and one- and zero-dimensional in the case of stepped W.

In the forthcoming Chapter it will be shown that such situation is not mandatory: a large-scale lateral reconstruction on a *flat* surface can lead to self organization of one-dimensional nanostructures and quantum clusters. In particular, formation of 1 nm-wide gold nanowires has been achieved on the two-dimensional tungsten surface carbide W(110)/C-R(15×3) at elevated temperature. Measurements of the nanowire electronic properties with ARPES demonstrate a distinct one-dimensional character of their electronic structure revealing effects of lateral electron quantization. Furthermore, self assembly of perfectly uniform molecular clusters of archetype fullerenes C_{60} has been observed on this substrate by STM. Both of these effects are unique in the sense that similar phenomena have never been observed before.

The Chapter has the following structure. In the first section results of a combined STM, ARPES, and XPS study of the W(110)/C-R(15×3) are presented. General features of its atomic and electronic structure are revealed and discussed.

Furthermore, temperature-controlled self-organization of Au nanowires and their electronic properties studied by STM and ARPES are reported. The last part demonstrates self-organization of C_{60} and offers an explanation for this effect involving model calculations in the van der Waals formalism.

4.1 Structure and electronic properties of a surface carbide: W(110)/C-R(15×3)

4.1.1 Introduction

Recent achievements from a combined study of atomic structure and electronic properties of a surface carbide overlayer on W(110) will be reported below. The 15×3 superstructure is well known for a long time, mainly due to the fact that it usually appears at the surface of newly produced W(110) samples during annealing because of surface segregation of carbon from the bulk of the crystal. While the bulk WC compounds, famous for extreme mechanical hardness, were extensively studied due to their role in applications [154, 243, 155], the 15×3 carbide overlayer used to be considered as undesirable contamination of W(110). We are interested in this structure for two reasons: a possible template effect for the nanostructure growth of the large scale reconstruction and the sizeable relative band gap of W(110) which can support electron confinement and offer a "window" for studying electronic properties of nanostructures.

The first studies of the C/W(110) system were done with the LEED technique. Two types of carbon-induced reconstructions were discovered: so-called R(15×3) [158] and R(15×12) [159]. Reflecting only the global periodicity of the surface, the LEED pattern itself provides limited information on the internal structure of the surface unit cell. The easiest way to obtain this information is to implement a local probe method: STM or AFM. Bode et al. (in 1995 for the first time) atomically resolved the cell of surface carbide [224, 225]. Their data reveal a two-fold symmetry of the overlayer and excluded some previously proposed models for the geometry of this superstructure: for instance, the W_2C model [160]. Relying on STM data, the idea of a surface lattice deformation by buckling of tungsten atoms in the topmost layer was also introduced [224]. Despite a number of works there is still no precise answer about the crystallographic structure of W(110)/C-R(15×3).

Since atomic and electronic properties of surface carbide are important with respect to self-organization of nanostructures on top, a particular effort has been applied to extend the knowledge on this system. Within the current Section, studies of geometry and, mainly, electronic properties of the R(15×3) carbon superstructure will be presented and further discussed.

A variety of techniques has been applied. The results presented are structured in several subsections which discuss LEED observations, verification by STM, photoemission study of chemical shifts in W4f and C1s core levels and, finally, the mapping of the band structures for W(110)/C-R(15×3) and clean W(110) performed with the ARPES method. In the last part, general conclusions about the atomic structure of R(15×3) surface carbide are made, based on LEED/STM observations and quantum-size effects discovered in the electronic structure.

4.1.2 Experimental details

Like in Chapter 3, the tungsten sample was cleaned by several cycles of annealing in oxygen (1×10^{-7}mbar) at 1200°C followed by flashing to 2200°C. Cleanliness of the sample was verified by absence of reconstructions in the LEED (Fig. 4.1(a), as well as by the presence of an intense surface-induced component in W4f core level spectrum (Fig. 4.4(a)). Formation of the carbide overlayer was achieved by heating the crystal for 5 min at 500-550°C under partial pressure of propylene of 5×10^{-8}mbar. A short flash to 2200° revealed the R(15×3) superstructure over the whole area of the surface (Fig. 4.1(b)).

STM measurements were performed in a double-chamber set-up equipped with an Omicron VT SPM microscope, as described in Chapter 1. Base pressure during the experiment was lower than 2×10^{-10}mbar. Electrochemically etched polycrystalline tungsten tips were used. *In situ* tip preparation (see Chapter 1) has also been carried out. Recording of the topography has been done under fixed sample bias voltage (+500 mV) and tunneling current of several tens of nA, unless specified. In a number of experiments, additional processing was implemented. Since one of the targets was to investigate the charge in the surface carbide W(110)/C-R(15×3), the tips were further prepared by "mechanical" breaks where the clean tungsten tip was carefully dipped into the clean W surface for several Å. It appears that upon extraction from the surface a nail-like nanocluster of W remains at the tip apex, providing a very high spatial resolution.

Photoemission measurements were performed under similar UHV conditions and strictly the same preparation routine. A detailed report on the photoemission set-up "HiRes", which was used in the present experiment, can be found in Chapter 1. Measurements were done at the UE56/1 PGM and U52 SGM beamlines at BESSY.

4.1.3 Results

Characterization with LEED

The LEED technique has been used to check the quality of the W substrate and the subsequently produced R(15×3) carbon superstructure. LEED patterns taken 58 eV energy of the primary electron beam (E_p) are given on Fig. 4.1(a,b). While Fig. 4.1(a) shows a sharp p(1×1) patten of clean W(110), Fig 4.1(b) demonstrates the distinct 15×3 superstructure after carbidization, which is rotated by 14° relative to [001] of the tungsten surface. These two images, taken at the same parameters, provide initial information about the ratios of the W and C surface unit cells and their mutual angular arrangement.

Characterization with STM, overall features

Results of the STM study of the tungsten surface carbide are presented in Fig. 4.2(c). The STM verification of the clean W(110) is given in Fig. 4.2(a) mainly for reference. The tungsten surface is not atomically resolved. Due to strong
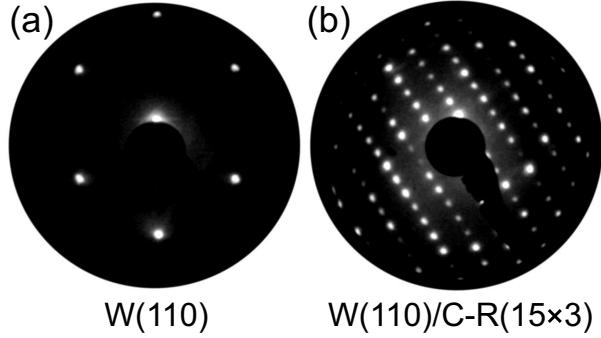
Figure 4.1: (a) the LEED pattern from the clean W(110) surface displays a $p(1\times1)$ pattern. Primary electron beam energy E_p=58eV; (b) Diffraction from two-dimensional surface carbide taken at the same orientation of the tungsten crystal and the same E_p. The distinct 15×3 superstructure rotated by 14° to [001] direction of the substrate is clearly visible.

localization of d-states in the conduction band of W, extension of the electron density above the surface is minor [163], a fact which makes the achievement of atomic resolution on this metal rather tricky. STM tips used in this work were not capable of this task. The STM topography obtained for the clean W(110) is, however, useful for z-calibration. A distinct line profile S across the edge of a monoatomic terrace (Fig. 4.2(b)) gives a height difference close to 2Å, which proves the perfect calibration of the microscope.

Figs. 4.2(c) and (d) demonstrate the carbon-induced R(15×3) reconstruction on W(110). A high resolution large-scale STM image of the surface carbide obtained at minimal tip-surface separation (tunneling current I_{tunn}=5nA and sample bias voltage V_{bias}=+500 mV) is shown in Fig. 4.2(c). Atomic resolution appears only for the tip extremely close to the surface (this point will be discussed in the next paragraph). Going high up with the current to I_{tunn} =25nA reveals the topography presented in Fig. 4.2(d). Dimensions of the surface unit cell were found to be (13 ± 1)Å $\times$ (8 ± 1)Å being perfectly consistent with the literature [224]. High symmetry directions of the carbide matrix are introduced as $V_\parallel$ and $V_\perp$. This notation will be further extensively used. Orientation of the W substrate has been revealed from comparative analysis of the LEED patterns and orientation of steps in STM images measured before and after carbidization. Two reference directions [001] and [1$\bar{1}$1] of W crystal are marked drift corrected with white arrows. In Figs. 4.2(c) and (d) one can clearly see the distinct zigzag chains of carbon atoms displaced between the non-atomically resolved stripes (dotted black line) which run along the direction $V_\parallel$ which is 14° anticlockwise rotated relative to the [001] vector of the W crystal. These stripes are, actually, also rows of carbon atoms. Poor resolution on these rows (also reported before [224, 225]) is due to their particular geometric and electronic configuration. In the atomically resolved measurements, carbon atoms exhibit a diameter of 1 Å, while their typical z-corrugation is not very large: about 0.3 Å.
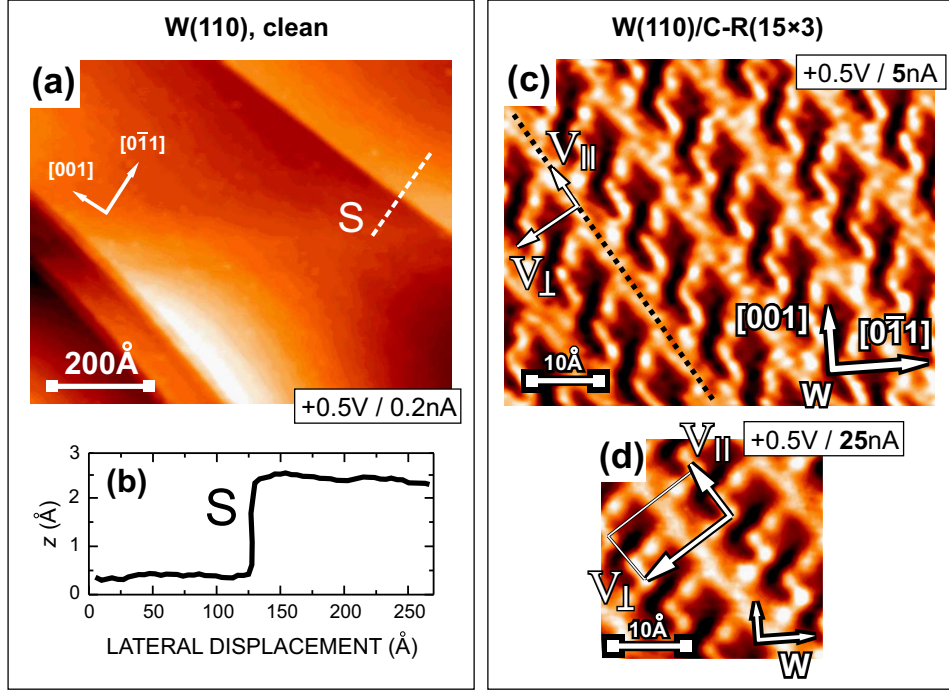
Figure 4.2: (a) STM topography of the clean W(110) measured at V_{bias}=+500 mV and I_{tunn}=0.2 nA; (b) line section across the edge of a monoatomic step on the W(110) surface. The step height is 2 Å; (c) large scale STM image of W(110)/C-R(15×3) taken at V_{bias}=+500 mV and $I_{tunn} = 5nA$; (d) the same area recorded at minimal tip-surface separation ($I_{tunn} = 25nA$).

Distance-dependent mode of the electronic structure detection: strong evidence of surface polarization

It was just mentioned, that atomic resolution on W(110)/C-R(15×3) can only be achieved at very low tunneling resistance i.e. at extremely low width of the potential barrier between the tip and the surface. In this respect, an important question appears: how realistic is the geometry of W(110)/C-R(15×3) observed by STM, and how should the electronic structure of the surface carbide be considered in the interpretation of the recorded images? Since STM is the only tool to investigate the local electronic structure of nanoobjects with nm-range resolution, a particular attempt to resolve a spatial charge distribution over the template has been undertaken. A distant dependent STM imaging of the local density (LDOS) of *unoccupied* states near the Fermi level (E_F) was done. Using the mechanically sharpened tip which provides high-resolution in x-,y- and z-directions, the LDOS above the surface of W(110)/C-R(15×3) has been measured.

It is important to note, that one has to be careful using the term "surface", (especially, in the case of ionic or covalent crystals, like WC). According to the classical definition [94] it means the plane of zero integral of charge density. Since in the present study we are interested in the geometry of chemical bonds over the atoms of W(110)/C-R(15×3), "surface" means the first atomic plane of the crystal.
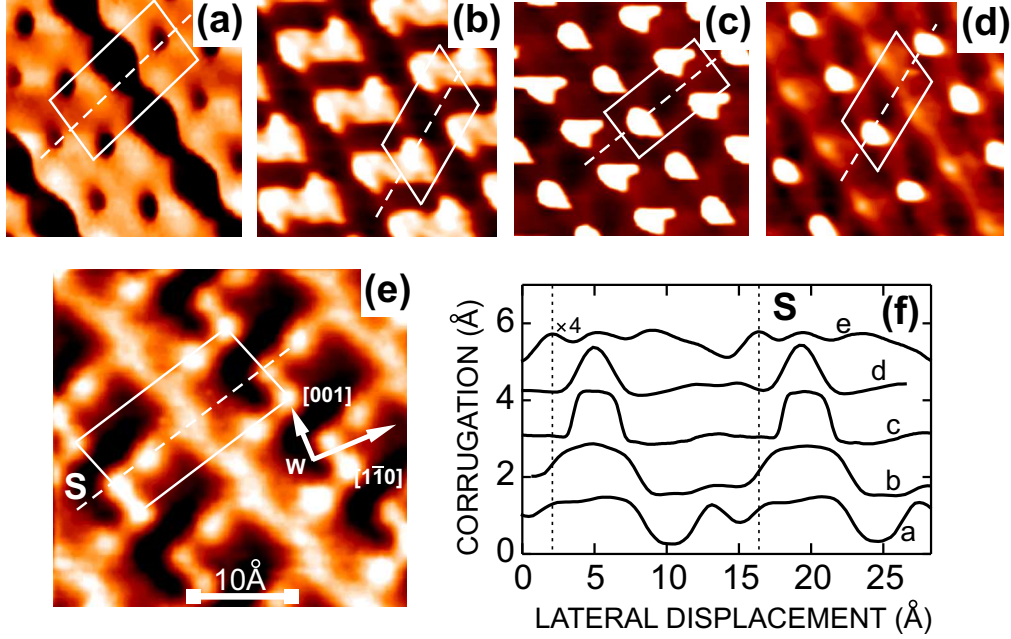
Figure 4.3: Distance-dependent STM study of W(110)/C-R(15×3). Evolution of the image morphology with decreasing of tunneling gap resistance: (a) tunneling resistance $\rho=1$ GΩ, striped pattern; (b) $\rho=770$ MΩ, cluster-like sequence; (c) $\rho=620$ MΩ array of double spots; (d) $\rho=540$ MΩ, strongly localized single spot; (e) $\rho=170$ MΩ, atomic resolution is achieved. Dimensions of the surface carbide unit cell after drift-compensation are found to be $(13.0\pm1.0\text{Å})\times(8.0\pm1.0\text{Å})$. Diagram (f) presents characteristic corrugations along the section S (dashed line in (a)-(e)).

Thus, it is more appropriate to speak about "bulk termination": in the following the term "surface" will be used exactly in this sense.

STM images taken at different values of the tip-surface separation demonstrate complex qualitative differences. The most typical topography patterns of the same sample area taken at different resistances (ρ) of the tunneling gap are shown in Fig. 4.3. The diagram in Fig. 4.3(f) provides a quantitative description of the corrugation amplitude presenting a characteristic corrugation along the section S. The first image (Fig. 4.3(a)) has been recorded at $\rho=1$ GΩ and corresponds to maximal distance of the tip from the surface. The last one (Fig. 4.3(e)) is taken at lowest separation, $\rho=170$ MΩ. With the tip high above the surface, the carbide superstructure in Fig. 4.3(a) is visible as stripes with holes and a wave-like edge profile. With decreasing separation the image loses its stripe character and starts to look like a cluster assembly (Fig. 4.3(b)). Further decrease of the tunneling barrier causes a breakup of the clusters into separate smaller spots with high image contrast (Fig. 4.3(c)). Going closer to the surface reveals a certain asymmetry in the structure. So Fig. 4.3(d), taken at $\rho=540$ MΩ, shows that the spots in every second row almost vanish while the rows in between maintain their large corrugation and become more localized. This asymmetry is a particularly important point for understanding the substrate geometry: it will be referred to

later. Finally, at higher tunneling current (ρ=170 MΩ) the morphology of the image changes drastically together with the achievement of atomic resolution (Fig. 4.3(e)): only now the internal zigzag structure [224] of the unit cell is resolved (Fig. 4.3(e) is the same as Fig. 4.2(d) and is given here for reference). Special care was taken in identifying the superstructure unit cell in the images which are not atomically resolved (Fig. 4.3(a-d)). In particular, positions of single adsorbed molecules and surface defects were used. The result is shown as white rectangles or parallelograms. Geometrical deformation, distinct to the images in Fig. 4.3(b) and Fig. 4.3(d), is an artefact determined by drift effects of the STM.

Note that the scan profiles (Fig. 4.3(f)) in non-atomically resolved images demonstrate a plateau-like behavior with relatively constant profile on its top and sharp edges meaning high contrast. The corrugation amplitude is nearly the same for all the images and has a value of about 1.2 Å. Starting out from ρ=600 MΩ, the profile changes and shows narrow peaks corresponding to a strongly localized DOS. Such plateau-like behavior is attributed to the presence of dangling bonds over the carbon atoms in zigzag chains, which create a laterally anisotropic charge distribution in the unoccupied LDOS at the surface of W(110)/C-R(15×3). These dangling bonds could either be carbon p_z orbitals, or one of the hybridized states sp^n.

Core level photoemission

Core levels of the elements in compounds can be very sensitive to the chemical environment. Analysing energy shifts of core level peaks one can gain information about the chemical bonding in the solid. Another possible origin of shifted core level peaks is the surface. Since the density of states at the crystal surface is energetically narrower due to lower coordination numbers of surface atoms, the requirement of charge neutrality at the metal surface causes in the simplest picture, an energy shift of the electronic structure of the surface atomic layer [161]. In order to probe the chemical configuration of carbon and tungsten in the surface carbide, XPS measurements have been performed. Photoemission spectra of distinct W$4f_{\frac{7}{2}}$ and C$1s$ core levels for the W(110)/C-R(15×3) system are shown in Figs. 4.4(a) and 4.4(b), respectively. The W$4f$ spectrum is given in comparison to the one for the clean W substrate. In order to reveal chemically shifted spectral components, a fitting routine [247] has been done. A summary of the parameters which provide the best fitting results is given in Table 4.1.

In the W$4f_{\frac{7}{2}}$ spectrum of clean W one can clearly identify the bulk emission line W$_B$ (31.41 eV) and a surface-induced component W$_S$, shifted by 0.32 eV towards lower binding energy relative to W$_B$. The surface-induced peak is related to the aforementioned narrowing of the DOS at the bulk termination.

The W$4f_{\frac{7}{2}}$ spectrum of the 15×3 carbon superstructure displays strong changes concerning these spectral components. While the bulk-derived peak W$_B$ saves its position, a surface-induced component W$_S$ is shifted now towards higher binding energies having 0.15 eV separation from W$_B$. One has to note that the intensity ratio between W$_B$ and W$_S$ in the case of the carbidized surface is approximately
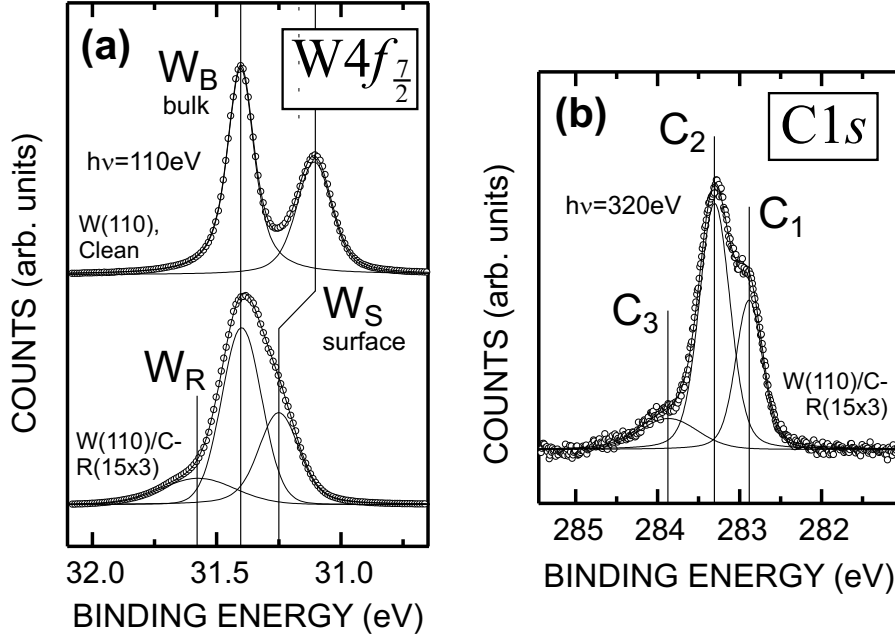
Figure 4.4: (a) W4$f_{\frac{7}{2}}$ core level spectra from clean W(110) and after the cracking of propylene. A shift of the surface induced peak W$_S$ by 0.14 eV manifests the formation of a continuous single-monolayer carbide film. The excitation energy is hν=110 eV. (b) Photoemission from the 1s core level of carbon. The fitting procedure gives three components C$_1$, C$_2$ and C$_3$. C$_1$, C$_2$ are determined by different chemical configurations of C atoms in the topmost carbon layer. C$_3$ is assigned to carbon atoms incorporated into surface defects.

conserved. Furthermore, an additional component W$_R$ appears at 31.89 eV, which was not observed for the clean W surface. The C1s spectrum of carbon overlayer also demonstrates a relatively rich structure revealing three components C$_1$, C$_2$ and C$_3$ at binding energies of 282.89 eV, 283.31, eV and 283.86 eV, respectively.

The origin of these components can be explained in terms of the chemical configuration of the C atoms in the surface layers. This question is to be further discussed below.

Angle-dependent photoemission

An investigation of the valence-band structure has been done for W(110)/C-R(15×3). The dispersion was accurately measured in high-symmetry directions of the 15×3 superstructure. In real-space notation, introduced for the STM data in Fig. 4.2, these directions are V$_\parallel$ (short edge of the surface carbide unit cell) and V$_\perp$ (long edge of the unit cell). Due to the fact that the vector V$_\parallel$ of the 15×3 superstructure is rotated by 14° relative to the [001] direction of W [158, 159] (see also the LEED on Fig. 4.1(a,b)), these directions are no high-symmetry directions of the substrate, therefore there will be no simple notation in terms of the W(110) surface Brillouin zone.

Table 4.1: Summary of the fitting routine for $W4f_{\frac{7}{2}}$ and C1s core levels. The component binding energies (E_b) are shown as well as fitting parameters for the FWHM (Lorentzian - ΔL and Gaussian - ΔG) which supply the best fitting result.

Component	E_b(eV)	ΔL(eV)	ΔG(eV)
W4f: W_S clean	31.09	0.07	0.13
W4f: W_B clean	31.41	0.09	0.07
W4f: W_S 15 × 3	31.26	0.06	0.16
W4f: W_B 15 × 3	31.41	0.05	0.18
W4f: W_R 15 × 3	31.58	0.02	0.34
C1s: C_1	282.89	0.10	0.39
C1s: C_2	283.31	0.11	0.33
C1s: C_3	283.86	0.10	0.78

Experimental data measured at hν=110 eV is presented in Figs. 4.5(a) and 4.5(b). While Fig. 4.5(a) shows a set of original angle-resolved spectra for $V_\parallel$, Fig. 4.5(b) contains the data set for $V_\perp$. Spectra in these two plots are scaled in a way to pronounce dispersions of weak peaks observed in the region 3-6.5 eV binding energy. Angles are marked for emission normal to the surface and for the topmost and bottommost spectra in each set. The normal emission (0°) spectrum is additionally emphasized by a thick solid line. In Figs. 4.5(a') and 4.5(b') the same spectra are shown but in the range of binding energies 1-4 eV normalized to the maximal countrate in order to demonstrate the dispersion of the most intensive bands of W.

After comparison of the photoemission data from W(110)/C-R(15×3) to the band structure measured along $V_\parallel$ and $V_\perp$ for the clean W(110) surface (Figs. 4.5(c) and 4.5(d)) it becomes easy to identify carbon-induced states (C-states) in the 3-6.5 eV binding energy range of the valence band and distinguish them from the states of the W. While the states with binding energy around 3 and 4 eV are assigned to C, because they appear inside of the W bulk band gap [164, 165], assignment of the high-binding-energy state (5.5-6 eV) is ambiguous, due to the fact that there is an sp-band (Σ_5^1) of W at the same energy. This sp-state is clearly visible in Figs. 4.5(c) and 4.5(d) which present the original spectra for clean W(110), emphasizing also the absence of C-induced states in the 3-6.5 eV energy range. One has to note that bulk hexagonal WC [241, 243] features a carbon sp-band at nearly the same binding energy. Therefore, this state is assumed to be carbon-induced.

One has to point out several effects discovered comparing the band structures of W(110)/C-R(15×3) mapped for both directions $V_\parallel$ and $V_\perp$. Figs. 4.6(a) and 4.6(b) represent the dispersions E($\mathbf{k}_\parallel$) extracted from photoemission spectra. First of all one has to note a superlattice effect in the dispersion of C-states. A different periodicity in $V_\parallel$ and $V_\perp$ direction can clearly be seen. While the reciprocal-lattice period $\Delta k_{C\parallel}$ of the dispersion along $V_\parallel$ is ∼0.6 Å^{-1}, the period for $V_\perp$, $\Delta k_{C\perp}$, is
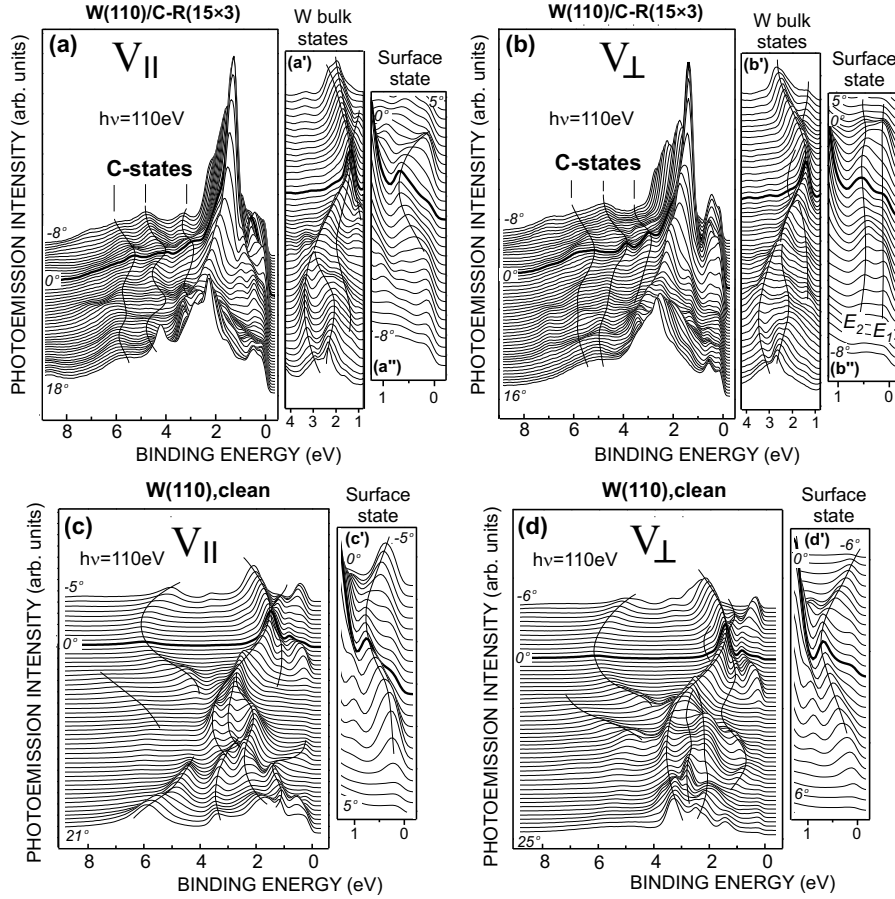
Figure 4.5: Angle-resolved spectra of the valence band of surface carbide W(110)/C-R(15×3) and clean W(110) measured in high-symmetry directions of the 15×3 superstructure. The data set measured for $\mathbf{k}_\parallel$ along direction $V_\perp$ is given in (a), for $V_\parallel$ - in (b). Insets emphasize the behavior of the bulk states of the substrate (a'), (b') and of the 0.6 eV surface state of W (a"), (b"). Plots (c) and (d) map the band structure of clean W(110) along $V_\perp$ and $V_\parallel$ respectively. Insets (c') and (d') illustrate the behavior of the 0.6 eV band for the clean W surface.

significantly larger: ~ 0.8 Å^{-1}.

A particular behavior is observed in the vicinity of E_F. For normal emission, the peak appears at 0.7 eV almost unmodified upon carbidization, just shifted towards higher binding energy by ~ 0.1 eV. This is remarkable since this feature has been assigned to a surface state [164, 166]. This means that the W(110)/C-R(15×3) structure includes some unmodified areas of W(110). For off-normal emission, however, strong modifications are observed. While for clean W(110) the 0.6 eV state shows a parabolic dispersion along $V_\parallel$ as well as along $V_\perp$, for W(110)/C-R(15×3) it becomes strongly anisotropic. Along $V_\parallel$, the dispersion remains largely parabolic, whereas along $V_\perp$ it splits up into two weakly dispersing peaks (E_1 and E_2 in Fig. 4.6(b)) manifesting a typical effect of size-quantization.
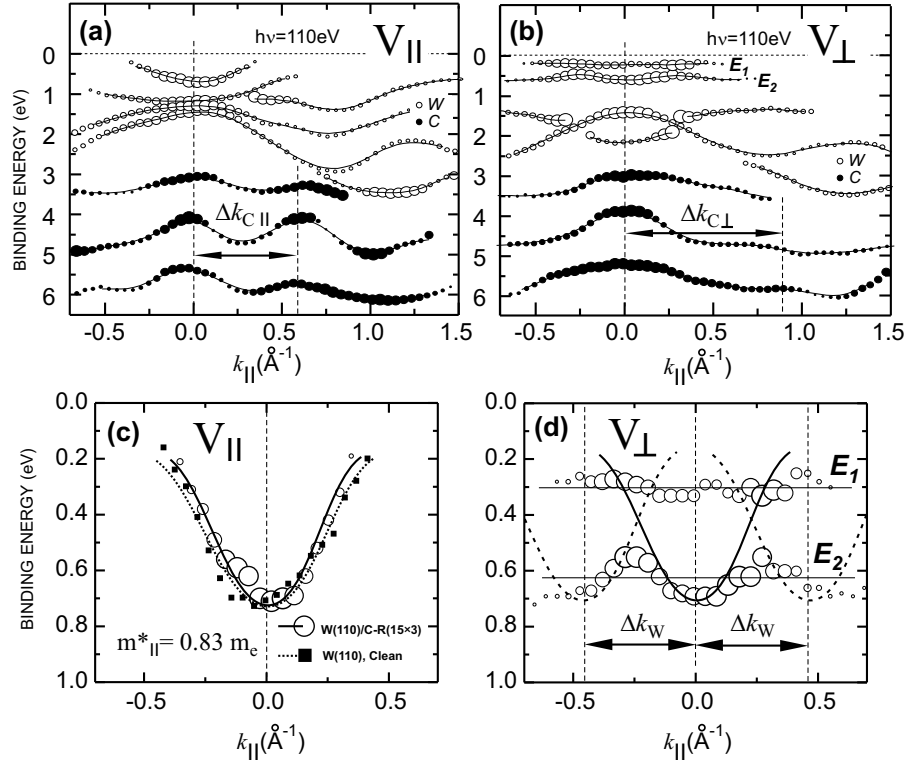
84

W(110)/C-R(15×3)

Figure 4.6: Electronic structure of the W(110)/C-R(15×3) surface carbide. Dispersions are extracted from the angle-resolved photoemission spectra shown in Figs. 4.5(a) and 4.5(b) for directions $V_\perp$ and $V_\parallel$. Bands marked with filled symbols in (a) and (b) are identified as carbon induced. The size of each data point reflects the intensity of the photoemission peak. The superlattice effect on these states is clearly visible (a), as well as quantization of the surface state at 0.6 eV (b); Plots (c) and (d) emphasize the dispersion of this state in directions $V_\perp$ and $V_\parallel$, respectively.

4.1.4 Discussion

The first step which is to be undertaken to formalize any further considerations is building up a structural model for the surface carbide W(110)/C-R(15×3). A determination of the correct lateral correspondence of the carbide superstructure to the W(110) substrate is impossible using only the methods of direct and reciprocal imaging like STM and LEED. The only mutual parameter which is known from LEED (Fig. 4.1) is the 14° angle of rotation between surface carbide unit cell ($V_\perp$,$V_\parallel$) and the basis vectors ([001],[1$\bar{1}$0]) of the W crystal.

A structural model based on the observed LEED (Fig. 4.1) and STM (Fig. 4.2) is introduced (Fig. 4.7(a)). This simple model was already once proposed in the literature [224, 225]. The lateral correspondence of the carbon matrix is chosen arbitrarily. Note that it is relevant to speak only about the correspon-
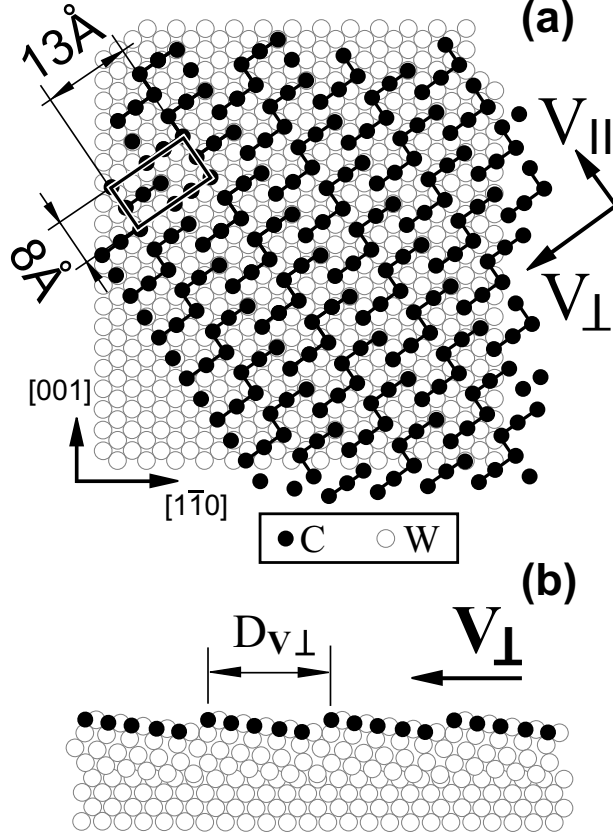
85

Figure 4.7: (a) structural model of the two-dimensional surface carbide W(110)/C-R(15×3); (b) idea of one-dimensional surface buckling upon carbidization.

dence to the bulk lattice of W, since the surface arrangement of tungsten atoms must be drastically affected by the strong chemical bonding to carbon. Although the following discussion will mainly be focused on the electronic structure of the W(110)/C-R(15×3), some qualitative conclusion on the atomic structure of the surface carbide will be made from the analysis of PES and STM.

Let us now start discussing the electronic structure and note some important features observed in the angle-dependent valence band photoemission. As Figs. 4.6 (a) and (b) show, three carbon-induced bands (marked with filled circles) located between 3 and 6.5 eV disperse with different period along the lattice vectors $V_\perp$ and $V_\parallel$ of the surface carbide superstructure. While the periodicity of dispersion measured in reciprocal space along $V_\parallel$ is $\Delta k_{C\parallel}$=0.6 Å^{-1}, for $V_\perp$ this value is $\Delta k_{C\perp}$=0.8 Å^{-1}. The real-space periods of this oscillations are $D_{C\parallel} = \frac{2\pi}{\Delta k_{C\parallel}}$=11 Å and $D_{C\perp} = \frac{2\pi}{\Delta k_{C\perp}}$=7 Å. Even if one considers a combined error for these values evaluated as 2 Å and 1 Å for $D_{C\parallel}$ and $D_{C\perp}$, respectively, they do not fit to the dimensions of the surface carbide unit cell (8± 1)Å×(13± 1)Å, determined by STM (Fig. 4.2). In order to understand this *superlattice* phenomenon, some considerations about the nature of these bands are to be made. Firstly, they are pure carbon states because their binding energies appear in the energy region of

the surface projected gap of W(110). Secondly, they can only be 2p-states (pure or sp-hybridized), because the characteristic peak of C2s is located at nearly 12 eV binding energy (Fig. 4.8), the same as in the bulk of hexagonal WC [242]. It is also very likely that these states are localized in the dangling bonds observed in the distance-dependent STM measurements (Fig. 4.3). The last point makes it apparently possible, that they gain their own superlattice above the surface carbide. For instance, their characteristic periodicity along the $V_\perp$ direction can be *half* of the carbide surface cell because of the in-plane break in the overlayer potential at the knees of the zigzag chains (Fig. 4.2(d)). Hence, for a period $D_{C\perp}$ one gains 7 Å, which correlates well with the expected dimensions.
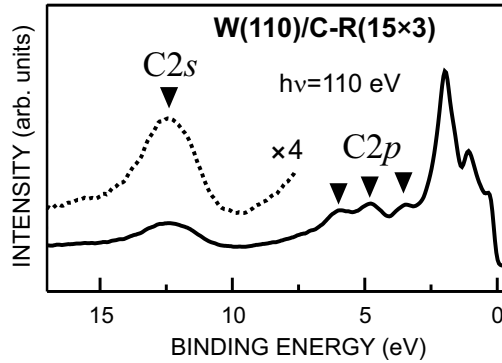

Figure 4.8: Photoemission of carbon states 2s and 2p from the valence band of the surface carbide.

Another important point which has to be discussed is the the lateral quantum size effect observed in the dispersion of the 0.7 eV band in W(110)/C-R(15×3) along $V_\perp$ (Fig. 4.5(b")). The precise behavior of this state is shown in the plot of E($\mathbf{k}_\parallel$) measured along $V_\parallel$ (Fig. 4.6(c)) and $V_\perp$ (Fig. 4.6(d)). Searching for an explanation for the splitting of this state into separate energy levels E_1 and E_2, one can speculate about different phenomena which can be involved. The spectra strongly resemble those from lateral quantum-well states confined on the terraces of vicinal Au(111) [167]. Indeed, rows of carbon atoms have in theoretical calculations been proven repulsive scatterers [172] and can, therefore, provide confinement. However, both lateral quantization and superlattice *umklapp* scattering may serve as explanation for the observed behavior. Careful analysis of the dispersion in Fig. 4.6(d) reveals that the observed splitting can be the result of a superposition between the ground state and umklapp scattered bands, translated by $\Delta k_W = 0.45$ Å^{-1} in $\mathbf{k}_\parallel$ space. If the dispersion is interpreted as resulting from umklapp effects the superlattice periodicity in the direction $V_\parallel$ is given by $\frac{2\pi}{\Delta k_W} = 14$ Å, which is fully in agreement with the expectation from the dimensions of the unit cell determined by STM.

We also want to consider the alternative interpretation of lateral quantization. One can use the particle-in-box approach applied in Ref. [167] for description of surface state quantization on the steps of vicinal Au(111). The formula (3.2):

$$(4.1) \qquad\qquad E_N = E_F - E_0 + \frac{\hbar^2 \pi^2}{2m_{\parallel}^* L^2} N^2$$

was already introduced in previous chapter. It gives the binding energy of the Nth quantized level referred to the ground state E_F - E_0. The in-plane effective mass m^* of the electron can be independently determined from the parabolic dispersion measured in the direction $V_{\parallel}$ (Fig. 4.6(c)) using a least squares fit in the interval $-0.2\text{Å}^{-1} <| \mathbf{k}_{\parallel} |< 0.2\text{Å}^{-1}$ as $m_{\parallel}^*$=0.83 m_e. Considering this value and the energy splitting E_2-E_1=0.31 eV one obtains from Eq. (4.1) the width of the quantum well as $D_{V\parallel} = 15 \pm 2$ Å. Within the error bar this value is consistent with the expected periodicity of 13 Å. There is still one more question to answer. Why is quantization observed along $V_{\perp}$, but no traces of it are found in the dispersion along $V_{\parallel}$? One reasonable explanation is a carbon-induced buckling of the W substrate hypothetically assumed in Ref. [224]. The pure W(110) areas required for the existence of the surface states can be identified as dark spots in Fig. 4.2(c,d). The W surface in these areas under the influence of carbon can become tilted forming a periodic saw-tooth profile in $V_{\perp}$ direction (Fig. 4.7(b)). In the STM, however, this buckling can remain invisible due to the shape of the carbon wave-functions, which are responsible for the tunneling. Another important evidence of such buckling is the aforementioned asymmetry observed in the evolution of the distance-dependent STM images (Fig. 4.3(d)). It is very likely that at a particular separation between the tip and the surface the spatial electronic structure will reflect that the template is not flat in the z-direction.

Now, summarizing the information on the electronic structure it is possible to assemble and improve the structural model of W(110)/C-R(15×3). The understanding of the surface carbide derived from this work is introduced below. Generally, it is suggested that carbon superstructure is embedded into the first monolayer of tungsten. This can be easily realized due to the small atomic radius of carbon (0.91 Å) which is twice less than the same of tungsten (2.02 Å). At elevated temperature during carbidization, carbon atoms may efficiently tend to form the hexagonal WC structure, traversing into the bulk while forming chemical bonds with W. Hence, the zigzag "fishnet" of carbon, which one sees in the STM data, represents the areas on the (110)-face of W through which carbon diffuses into the substrate (and where diffusion has already taken place for the first monolayer). The aspect that in STM one detects only C but no W is likely a question of chemical contrast due to the shape of $2p$-wave functions of carbon, i.e. a purely electronic effect.

Let us analyse the results of XPS measurements of the core levels W4f and C1s (Fig. 4.4) with respect to the proposed structural model. According to the model there is no direct C-C bonding in the surface carbide, and only W-C bonding can be responsible for the observed chemical shifts. Returning to the XPS spectra of C1s (Fig. 4.4(b)), two intense components C_1 and C_2 are observed. They originate from carbon atoms in different chemical configurations, which in

particular means different values of charge transfer resulting in local energy shifts. The relative intensity ratio of these two components ($\sim$1:2) suggests that peak C_1 originates from C in linear rows (see Fig. 4.7(a) and Fig. 4.2(c), dotted black line) which maintains 2 atoms per unit cell, while C_2 corresponds to the zigzag chain which incorporates 4 atoms. Looking at the STM data (Fig. 4.2(c,d)), one has to note that the W environment of C atoms in the embedded rows must be reduced compared to the zigzags, because in the zigzag each C has only two carbon atoms as neighbors, while in the rows the number of neighbors is three.

On the other hand, LAPW calculations of the electronic structure of bulk WC [243] have revealed that W-C chemical bonding features stronger electron transfer W$\rightarrow$C (this is also expected from the corresponding electronegativities: 1.7 for W, and 2.5 for C [227, 228]). This is, however, inconsistent with the observation that the binding energy of the C_2 component is higher. A possible explanation is that the carbon atoms in the linear rows anyhow have a higher coordination to W i.e. they are embedded deeper into the substrate than that ones in zigzags. This assumption fits well to the idea of surface buckling (Fig. 4.7(b)). Correspondingly, C_1 manifests stronger charge transfer W$\rightarrow$C being placed 0.5 eV towards lower binding energies.

It is useful to compare the absolute binding energies of core levels measured from the surface carbide with the same obtained from the bulk hexagonal WC [229]. For instance, in the bulk carbide the W4f component W_B is placed at 0.4 eV higher binding energy than in W(110)/C-R(15$\times$3). This is an additional evidence of lower coordination numbers of W with respect to C, which further supports the presented model and manifests the single monolayer character of the surface carbide on W(110).

The observed unequal charge transfer is also consistent with STM and ARPES measurements. In particular, a relatively decreased population of the 2p states of carbon in the zigzags explains two points: (i) achievement of atomic resolution on zigzag chains, and rather poor STM imaging of carbon rows (STM imaging in Fig. 4.2 has been performed for unoccupied states), and (ii) the aforementioned miscorrelation of the superlattice dispersion of C-states in the direction $V_\perp$ (Fig. 4.6): if the wave functions of carbon rows are not overlapping with those in the zigzags, then it is possible that they show no dispersion at all.

Speaking about the component C_3 in the C1s spectrum (Fig. 4.4) it is needed to note that it has the highest binding energy, which, in particular, means weakest electron exchange with W. This happens for C atoms which have lower coordination numbers with respect to the W lattice. Therefore, the component C_3 can be attributed to some amounts of carbon adsorbed at the surface or incorporated into the surface defects (like domain borders of the R(15$\times$3) superstructure).

The last thing to be proved is that the observed quantization of the 0.7 eV surface state (and its existence) are consistent with the proposed structural model of an embedded carbon "fishnet". Penetration of carbon atoms inside the surface lattice of W(110) will strongly affect the atomic structure of open tungsten areas between the carbon zigzags. On the other hand, it still creates a surface-like bulk termination with new properties and new modulation of the crystal potential.

This point is supported by the presence of the surface-induced component W_S in the W4f spectra upon carbidization (Fig. 4.4(a)). Hence, the surface state at 0.7 eV can be considered as a *new* surface state created by the potential of the W(110) surface with periodically arranged carbon insets. This point is supported by a different binding energy of the surface state before (0.6 eV) and after (0.7 eV) carbidization. The behavior of the dispersion has also been compared. In particular, in Fig. 4.6(c) the dispersion of the surface state on clean W(110) is additionally plotted (black squares) being shifted to 0.7 eV binding energy for comparison. However, in the effective mass no drastic difference is observed.

Summarizing, a combined study of two-dimensional tungsten surface carbide W(110)/C-R(15×3) involving LEED, STM, XPS, and ARPES techniques has been performed. LEED and STM measurements revealed the atomic structure of the carbide overlayer and its orientation relative to the tungsten bulk. Based on XPS measurements of the C1s core level as well as on spectra of the chemically sensitive W4f a general structural model has been proposed. It suggests that the matrix of carbon atoms is embedded into the first or even second atomic layer of W(110). The electronic structure of the surface carbide measured with ARPES revealed anisotropic quantum size effects involving the surface state at 0.6 eV (clean W) and 0.7 eV (carbidized surface) binding energy. In comparison to pure W(110), the electronic structure measured along the lattice vectors of the surface carbide unit cell revealed a parabolic character of dispersion in one direction and splitting up into separate energy levels in the other. Such behavior can be explained involving ideas of umklapp scattering as well as lateral quantization.

Although an extensive study of W(110)/C-R(15×3) has been performed, a complete understanding of this system is not yet achieved. Within the results reported above only a carbon-induced surface passivation and the geometry were established. But the exact crystallographic structure of the first several monolayers is still missing. It is rather acceptable in the framework of this Thesis, since the characterization of the surface carbide was only an intermediate task, required for understanding of successively produced metallic and molecular nanostructures. As for general scientific interest, certain additional experiments are necessary. In particular, the next step to be undertaken is use of the surface sensitive method of X-ray structure analysis in grazing incidence [6].

4.2 Self-assembled Au nanowires and their electronic structure

4.2.1 Introduction

It has already been mentioned that metal nanostructures are extremely important for technology because their properties can be affected by electron confinement and quantization. Achievement of confinement in two-dimensional films, where the thickness is the main parameter has meanwhile become a routine: these systems are well understood structurally and electronically [77]. Analysis of a typical two-dimensional system has been demonstrated in Chapter 2, where the ground state of Ni(111) has been probed by electron quantization in the Ag overlayer. A review of relevant literature has also been given in Chapter 2.

Additional lateral quantization in a nanowire array will affect the electronic density of states in the metal even more profoundly and in particular create anisotropic $E(\mathbf{k})$ band dispersions. On the atomic scale, it has been achieved to create atomic chains of metals that display a one-dimensional band dispersion using self organization on stepped [175, 176, 177, 178] and flat substrates [179]. A similar, but rather complicated system has been reported in Chapter 3 of the present Thesis, where anisotropic lateral quantum-size effects have been observed in alloyed step-decorations of W(331) and W(551).

Taking the measured band dispersion as criterion for one-dimensionality, it appears to be difficult to produce nanowires that bridge the range from the single-atom diameter [175, 176, 177, 178, 179] to nanometer width. Such wide wires would open up a more realistic perspective for application but we are not aware of any measurement of the band dispersion of such systems. On the other hand, there is no obvious principle hindrance since a one-dimensional dispersion and lateral quantization have been demonstrated for electrons on stepped Au crystals with wide terraces of 3.8 nm width [167] so it may be concluded that present preparation techniques for nanowires are not sufficiently advanced to achieve this. In the following it will be demonstrated that self-organization on a flat W(110) pre-patterned with the R(15×3) superstructure of carbon can control formation of nm-wide wires, which display a one-dimensional dispersion and characteristic lateral quantum well states.

4.2.2 Experimental details

The surface geometry of the nanowires was studied LEED and STM. The electronic structure was investigated with photoemission techniques using the VG ESCAlab electron analyser at 80 meV energy and 1° angle resolutions. Undulator radiation from the BESSY beamlines UE52 and UE56/1 was employed.

The W(110) sample was prepared *in situ* keeping the pressure in the chamber below 2×10^{-10}mbar. Initial cleanliness of the W surface was verified with LEED (Fig. 4.9(a)). Formation of the 15×3 carbide overlayer was achieved in the way described in the previous section. The nanowires have been prepared by deposition

of 0.7ML Au from a resistively heated evaporator followed by annealing at 600°C. This thermal treatment was found to be necessary for self-assembly of the nanowire array.

4.2.3 Results

Characterization with LEED and STM

The LEED pattern from the nanowires is shown in Fig. 4.9(c). It reveals a distinct one-dimensional R(9×1) pattern. Fig. 4.9(a) and (b), which demonstrate electron diffraction from the clean and carbidized W(110), respectively, are the same as in Fig. 4.1 and given here for reference in order to demonstrate the orientation of the nanowires to the W(110) substrate.
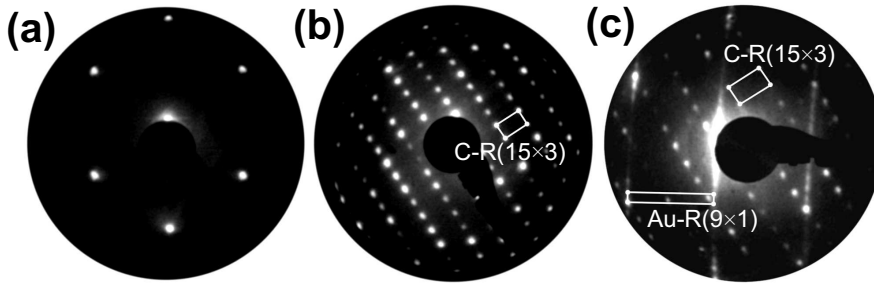

Figure 4.9: The LEED characterization; (a) verification of cleanliness of W(110) and (b) diffraction from the R(15×3) carbide superstructure (the same as in Fig. 4.1); (c) the LEED pattern taken at the same orientation of the sample from the 0.7ML Au on W(110)/C-R(15×3) after annealing reveals the R(9×1) Au reconstruction which is assigned to formation of the nanowires. All patterns are observed at 65 eV.

STM measurements of the self-assembled Au nanowires are presented in Fig. 4.10(a) and (b). Fig. 4.10(a) presents a large-scale STM scan which reveals the dynamics of self-organization. Because the STM image demonstrates large areas of the R(15×3) carbon reconstruction which are free of Au, one can conclude that Au under elevated temperature migrates over the surface forming compact nanowire-patterned islands. Fig. 4.10(b) was taken at significantly enlarged scale. It provides insight into the nanowire dimensions and internal structure. The nanowires are doubled and form arrays of pairs over the surface. Each pair has a width of about 25Å. The perpendicular profile A of the single pair is shown in Fig. 4.10(d) revealing a width of 10Å for each wire. Fig. 4.10(b) clearly demonstrates that every first nanowire in the pair has a dense continuous structure, while every second one consists of uniform and periodically arranged clusters. The illustration to this property is given in Fig. 4.10(e), where the profile sections B and C along the wires are shown. It is difficult to conclude on the thickness but presumably the Au nanowires are 2 or 3 atomic layers thick, at least one of which is embedded
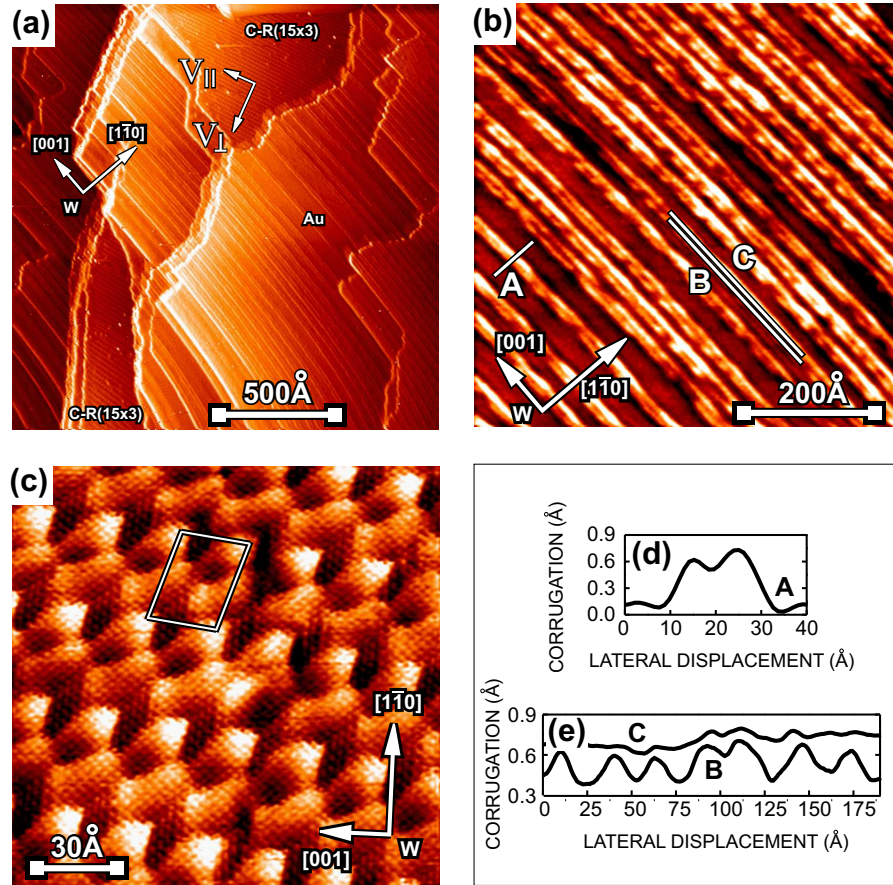
Figure 4.10: STM study. Large-scale STM image of annealed Au/W(110)/C-R(15×3) reveals co-existence of open areas of the R(15×3) carbon reconstruction and Au nanowires; internal structure of the Au nanowires (b); they appear in pairs (d). The first nanowire has a continuous and dense structure while every second nanowire consists of periodically arranged Au clusters (e). For comparison, submonolayer Au on *clean* W(110) forms no nanowires but a different large-scale reconstruction (c).

into the carbon matrix or alloyed with the topmost layer of W. This point will be discussed further below.

Comparing the LEED images for the clean R(15×3) (Fig. 4.9(b)) and the annealed Au/W(110)-R(15×3) (Fig. 4.9(c)), it becomes evident that the nanowires are rather aligned to the [001] vector of W(110) substrate than to the R(15×3) matrix of the interface carbon.

Angle-dependent photoemission

The electronic structure of the nanowire array studied by angle-resolved photoelectron spectroscopy is reported in Fig. 4.11. Spectra were measured for **k**-vectors of photoemitted electrons parallel (Fig. 4.11(a)) and perpendicular (Fig. 4.11(b))

to the wire orientation. Figs. 4.11(c) and (d) represent dispersions in **k**-space extracted from the spectra. The size of the markers reflects the intensity of the peaks. The Au-induced states are marked with solid and dashed lines. They were unambiguously identified by comparison to spectra for W(110)/C-(15×3) obtained without Au (Fig. 4.12). Dispersions in Fig. 4.12 were measured along the same directions as in Fig. 4.11. They show that the surface carbide has a pronounced contribution mainly for binding energies below 4 eV. Within this energy range the spectra coincide with the ones after nanostripe formation (Fig. 4.11). As for energies above 4 eV, there are either no sharp peaks of the carbide or they have a particular binding energy or dispersion that differ from those of the Au band and can clearly be distinguished for these reasons.

Figs. 4.11(a) and 4.11(c) exhibit an almost non-dispersing state d_1, which has a binding energy of about 6.5 eV, as well as a state d_2 dispersing in the range from 3.5 eV to 5 eV. The electronic structure obtained in the perpendicular direction is more complicated. The band d_2 is now split up into a pair of states with almost vanishing dispersions and binding energies E_1=4 eV and E_2=5 eV.

4.2.4 Discussion

The observed anisotropy with large dispersion along the nanowires and no dispersion perpendicular proves already the one-dimensional behavior of the electrons in the nanowires. Confinement along the direction perpendicular to the surface is ensured by comparison to the band structure of W(110) which features a large band gap [164, 165] in the range from 2 eV to 6.3 eV, i.e. including E_1 and E_2. The gap is essential for formation of two-dimensional quantum-well states on W(110) [81, 83] and supports also the present quantum wire states.

In order to relate the observed splitting to the atomic structure of the nanowires the approach [167, 168, 169] used for description of the surface state quantization on W(110)/C-R(15×3) in the previous Section has been employed again. Considering a nanowire as infinite one-dimensional potential well of width L binding energies of confined electron states are given by Eq. (4.1) ($E_N = E_F - E_0 + \frac{\hbar^2 \pi^2}{2m_\parallel^* L^2} N^2$).

The in-plane effective mass of the electron in the d_2 state has been determined, as before, from the dispersion observed in the direction parallel to the wires (Fig. 4.11(a,c)) using a least squares fit $E(k_\parallel)=\hbar^2 k_\parallel^2/2m_\parallel^*$ in the momentum interval $-0.2\text{Å}^{-1} < k_\parallel < 0.2\text{Å}^{-1}$. Here one obtains $m_\parallel^*=-0.97m_e$ (m_e is the mass of the free electron), which is typical for d-states [173, 174] (Note that m* < 0 leads to a quantum well of reversed energy scale). Considering this value and the width of the wire L= 10 ± 1 Å (Fig. 4.10(d)), Eq. (4.1) gives the energy splitting between the quantum well levels $\Delta E = E_1 - E_2 = 1.0 \pm 0.2$ eV, which is well consistent with the experimentally observed value 0.9 eV.

It is necessary to test whether *umklapp* scattering in the final state of the photoemission process could lead to a similar dispersion [170, 171]. As seen in Fig. 4.11(d), the dispersion of d$_2$ in the direction perpendicular to the wires appears as if repeated with a period $\Delta k \sim 0.8$ Å^{-1}. The corresponding periodicity in real space
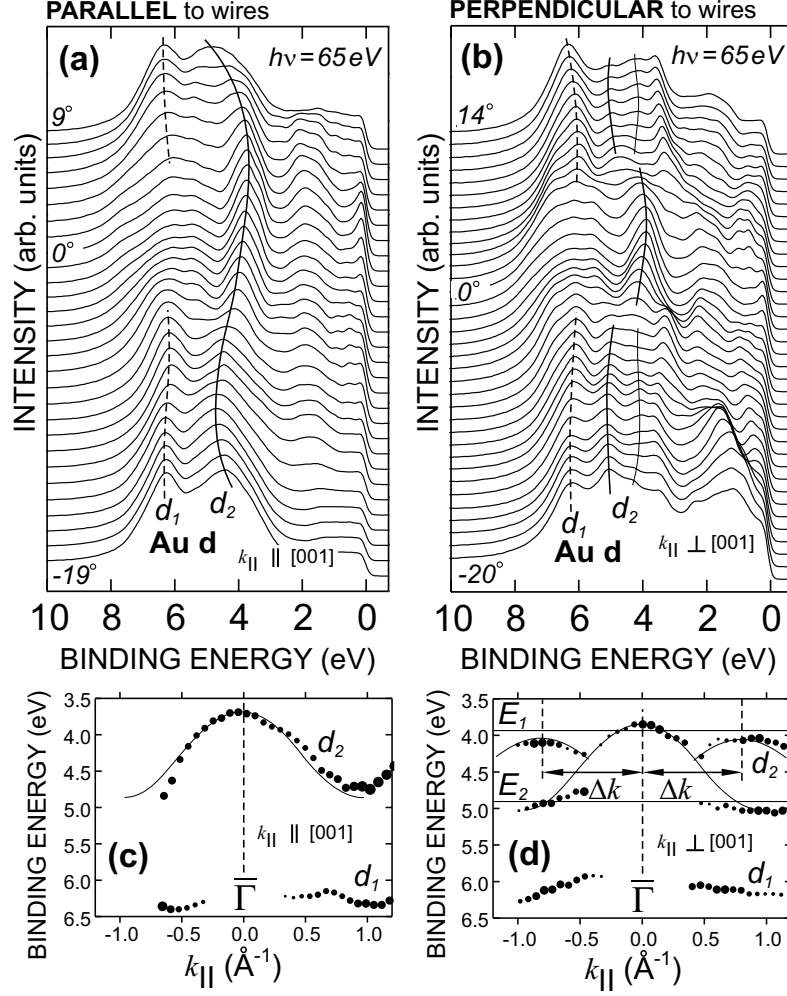
Figure 4.11: Angle-resolved photoemission of the Au nanowire array. Au d states show a dispersion for $\mathbf{k}_\parallel$ vectors along the nanowires (a) and size quantization perpendicular (b). $E(\mathbf{k}_\parallel)$ dispersions extracted from the spectra are shown as well (c,d).

D=$2\pi/\Delta k$ is ~ 8 Å. It does not fit to the expectations of 30 Å(since the nanowires are paired and the periodicity of their superlattice along the [001] direction of W is given by the double width of the wire plus the lateral interwire separation). This supports the proposed interpretation as lateral quantization effect in the initial state. The intensity behavior in Fig. 4.11(d) with the intensity of E_2 missing for $k_\parallel$=0 is explained by the probability density distribution of the wave functions (the N=2 quantum-well state has a node for $k_\parallel$=0) [169]. Understanding the origin of the d_1 state, one can assume that this may be a quantum well state formed in the isotropic elements of the second nanowire, which consists of periodically arranged Au clusters (Fig. 4.10(b) and 4.10(e)) and therefore d_1 would not disperse. However, the band d_1 is also distinct for the bulk Au [118], therefore this assumption is a speculation.
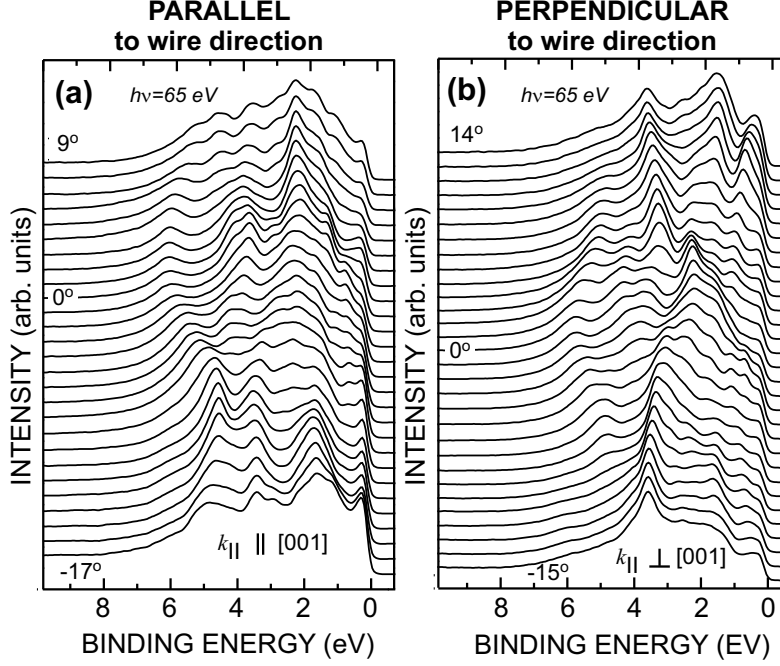
Figure 4.12: Angle-resolved photoemission from a surface carbide W(110)/C-R(15×3) without Au measured along the direction in which the nanowires will grow (a) and perpendicular to it (b).

In order to ensure that the self-assembly effect is in fact determined by the R(15×3) interface superstructure, a comparative study on clean W(110) has been performed as well. In particular, 0.7ML of Au were deposited on a completely cleaned W(110) surface and annealed exactly at the same temperature 550°C at which the self-organization of Au on W(110)/C-R(15×3) takes place. Neither LEED nor STM indicate a one-dimensional character of the surface after the annealing. Instead, a complicated reconstruction forms over Au islands as shown in Fig. 4.10(c) with atomic resolution. Dimensions of the surface unit cell of this superstructure were found be (39 ± 2) Å $\times$ (31 ± 2) Å (the comparatively large error bar is due to a drift effect). The origin of this reconstruction is likely atomic stress in the Au film. The stress is already substantial for Au on clean W(110) due to the two-fold anisotropy of the (110) face of W as pointed out in Ref [180].

Returning to the Au nanowires, we will consider the origin of the self-organization and discuss the possible role of surface alloying between Au and W. While an alloy between these two elements does not exist in the bulk, it was shown in several studies that it can appear at interfaces [181]. It is possible to probe surface alloying on the basis of photoelectron spectra of the W$4f_{\frac{7}{2}}$ core level. The four line fit components [247] shown in Fig. 4.13 correspond to: (a) clean W(110) (with perfectly resolved and intense surface component [161]), (c) carbidized W(110)/C-R(15×3), (d) 0.7ML Au/W(110)/C-R(15×3) (after annealing and with fully developed nanowires) and (b) 0.7ML Au on clean W(110) from the comparative study. The appearance of two spectral components at 31.6 and 31.85 eV for annealed Au
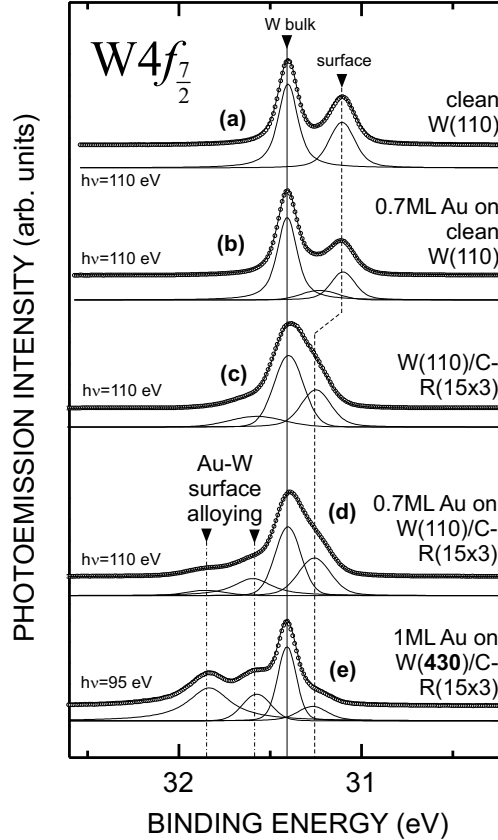
Figure 4.13: Comparison of the chemically sensitive W4f spectra taken from W(110) (a), W(110)/C-R(15×3) (c), Au/W(110)/C-R(15×3) (d) and Au on the clean W(110) (b) shows that Au-W surface alloying is likely involved in the process of nanopatterning. Because alloying-related components of core levels in the photoemission from Au/W(110)/C-R(15×3) are not intense, the spectrum of faceted Au/W(430)/C-R(15×3) is additionally given (e) in order to highlight the chemical shifts.

on W(110)/C-R(15×3) manifests a chemical interaction between Au and W. These components are, however, not intense. This can likely be explained by the short escape depth of the photoelectron for the employed photon energy (at hν=110 eV it is about 2 Å) The point is that alloyed areas must be buried under the Au nanowires which are *at least* 1 monolayer thick. In order to highlight these chemical shifts, the W4f spectrum of 1ML Au annealed on W(430)/C-R(15×3) is given for reference (Fig. 4.13(e)). Vicinal W(430) becomes strongly faceted upon carbidization [182] causing an increase of the photoemission signal from the interface layer at the edges of facets.

Surface alloying presumably takes place on the carbon-free areas of W(110) i.e. between the zig-zag carbon chains (see Fig. 4.2(c,d) and Fig. 4.7(a)). As it has already been stated in the previous Section, the carbon atoms upon their embedding in the first layer of tungsten cause a strong lateral deformation of the W(110) surface lattice. Such stressed W areas may alloy with Au in order to
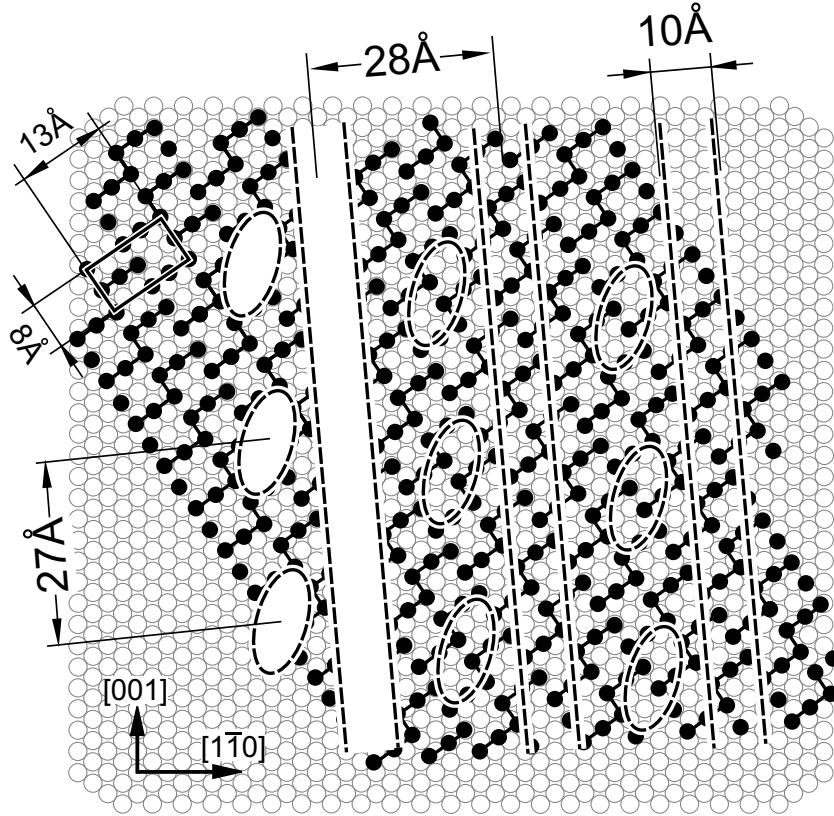
Figure 4.14: Structural model of self-organized Au nanostructures on W(110)/C-R(15×3). The carbide template (filled circles) consists of atomic C rows interconnected by zigzag chains on the W(110) surface (open circles). The Au arrangement is shown as dashed lines where ellipses mark the cluster structure observed for every second nanowire.

minimize their surface energy. Presence of two different chemical shifts 31.6 and 31.85 eV may suggest that alloying involves at least two atomic layers of tungsten. In the next turn, the buckling caused by W-Au atomic exchange at the surface lead to a patterning of the Au film and formation of nanowires. The absence of any chemical shifts in W4f for annealed Au on flat relaxed W(110) (Fig. 4.13(e)) proves the crucial role of the R(15×3) interlayer in the observed effect of self-organization.

Careful analysis of the LEED and STM data leads to a simple model which intends to relate the Au nanostructures to the W(110)/C-R(15×3) substrate. The model is illustrated in Fig. 4.14. One can expect that adsorption of gold adatoms takes place between the zig-zag chains of the carbon overlayer. Positions of predominant growth of Au (continuous wires and cluster assembly) are marked with dashed lines. As Fig. 4.14 shows, the Au nanoclusters must be separated from each other as well as from the next nanowire by one unit cell of the surface carbide superstructure, in order to lead to the observed dimensions. The wire orientation is by 4° off relative to the [001]-direction of W. This value is determined precisely (±0.5°) since the STM image of Au/W(110)/C-R(15×3) (Fig. 4.10(a)) contains

open areas of the carbon superstructure providing an absolute reference for angular orientation.

Although the model agrees well with the experimentally measured geometry and dimensions, it does not answer the question why the first nanowire in each pair has a continuous structure and the other one is separated into clusters. Presumably, this can happen because of the proposed one-dimensional buckling of W(110)/C-R(15×3) in the direction $V_\perp$ (Fig. 4.7(b)), which was employed in the previous Section to explain the surface state quantization (Fig. 4.5(b")). The apparent clusters can in fact be a beating pattern between the modulation of W(110)/C-R(15×3) and the grid of the nanowires defined by alloying.

In summary, it has been shown that the large-scale W(110)/C-R(15×3) reconstruction formed by carbidization of W(110) can be used as template for the growth of Au wires of nanometer width. The electronic structure of the system measured with photoelectron spectroscopy has demonstrated a one-dimensional band structure and the first appearance of distinct lateral quantum-well states in nanowires. The observation of chemical shifts in W4f photoelectron spectra allows to suggest that W-Au surface alloying at the open stressed areas of the W substrate induces the observed one-dimensional self-organization.

4.3 Self-organized nanoclusters of fullerene molecules

4.3.1 Introduction

For a very long time allotropes and compounds of carbon have been in the focus of frontier research activities [183]. Having the electronic configuration $1s^2 2s^2 2p^2$ for the free atom, carbon may gain in compounds and non-amorphous allotropic forms one of three possible hybridization states: sp(carbine), sp^2(graphite) and sp^3(diamond). Hybridized orbitals are responsible for electrical and mechanical properties of carbon solids.

In 1985 a new allotrope form of carbon, the fullerenes, has been discovered [184]. This discovery has opened up a new area of nanostructure research solely based on carbon, which features unique electronic properties like nanomagnetism and superconductivity. Fullerenes are secluded molecules with a sphere-like shape and hollow core. The most stable molecule is C_{60}. It has the highest symmetry (I_h) in the class and gains a form of truncated icosahedron. This molecule is also known as buckyball or archetype fullerene. Its structure is represented in Fig. 4.15. The molecule contains 20 hexagons and 12 pentagons, which give rise to the curvature enabling the closed spherical structure of C_{60}. Stability and non-reactivity of this molecule is provided by the rule of isolated pentagons, which means that pentagons cannot be neighbors but are always separated by a hexagon. Note that this rule cannot be satisfied in fullerenes of smaller dimensions. In fact, smaller carbon cages like, for instance, C_{20} have been successfully produced [185], but studies of their properties were only possible in the gas phase or in polymerized forms.

Because fullerene is practically a sheet of graphite secluded in a sphere, the predominant type of hybridization in the interatomic chemical bonding (σ-bonds) is sp^2. The word "predominant" means that there are actually two types of bonding, which are marked in Fig. 4.15(a) with single and double lines, respectively. Single lines represent so-called single bonds, which are majority bonds shared by one hexagon and one pentagon. In the single bonds carbon atoms participate which exhibit graphitic hybridization of sp^2-type. The length of a single bond is 1.46Å. However, there exist so called double bonds, shared by two hexagons and represented by double lines in Fig. 4.15(a). They come from the atoms in the sp^3 hybridization state of diamond and have a characteristic length of 1.40Å. Their angle in the pentagon is 108° being very close to the one in the diamond crystal (109°28"). The atomic diameter of the C_{60} cage is 7.1Å. Since the majority of C atoms is of sp^2 hybridization state, there will be dangling p_z orbitals of the $2p$ atomic shell, directed perpendicular to the buckyball's surface. Molecular electronic states derived from these orbitals (π-states), hold the main responsibility for electronic properties of the fullerenes and their conductivity. Because of the π-states, the effective diameter of C_{60} will be different from the atomic one. It is defined as the diameter of charge localization which is equal to 10Å.

Regarding electronic properties of the fullerenes in more detail, one can refer

to many theoretical and experimental works [186, 187]. The closed-shell electronic structure of C_{60} results in a π-derived fivefold degenerate highest occupied molecular orbital (HOMO) and a threefold degenerate lowest unoccupied orbital (LUMO). Occupied states are mainly localized on single bonds in the fullerene cage, while unoccupied states are predominantly situated on the double bonds. The electronic structure of occupied and empty states in C_{60} measured with photoelectron spectroscopy (PES) and inverse photoelectron spectroscopy (IPES), respectively, is shown in Fig. 4.15(b) (the figure was taken from Ref. [187]). The electronic configuration of the π-states (HOMO) and π^*-states (LUMO) appears in the valence band spectra as sharp peaks. Above 7 eV and below -6 eV binding energy the σ-states also start to contribute to the signal [186, 183].
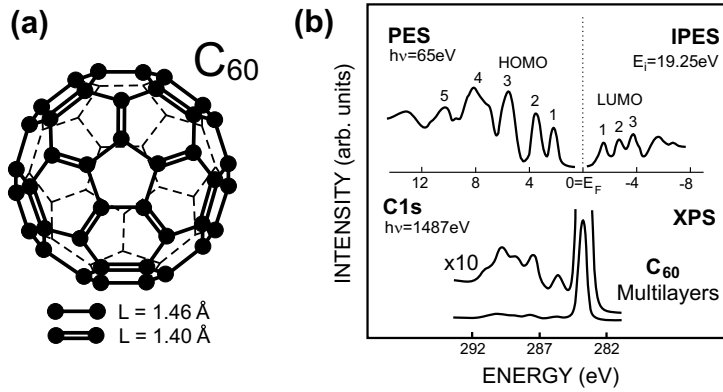

Figure 4.15: (a) atomic structure of archetype fullerene C_{60}. The molecule has the geometry of a secluded graphite sheet, but involves two types of C-C bonds, which correspond to different hybridization states of carbon atoms. The length of the single bond is 1.46Å, for the double bond this value is less - 1.40Å. The absolute diameter of the atomic cage is 7.1Å, while the one of the effective charge cage is known to be 10Å; (b) electronic structure of C_{60} valence band below and above Fermi level, as well as a π-π^* shake-up structure of the C1s core level in the fullerene molecule. The figure was taken from Ref. [187]

Fullerenes can also exist in a solid phase forming face-centered cubic (f.c.c.) crystals with lattice constant a_0=14.2Å under ambient conditions [188]. Although, the interaction in these crystals, which are known as fullerite, is very weak due its van der Waals nature, overlapping of π-states results in the appearance of a distinct dispersing bulk electronic structure [186, 189]. The fullerene solid state has recently attracted huge attention because of unexpected electronic properties. In normal conditions fullerite is an insulator because the energy bands of archetype C_{60} are either completely filled or completely empty, introducing a large energy gap between HOMO and LUMO ($\sim$ 3 eV). To induce metallicity in the fullerene either the conduction band has to be partially filled by electron doping, or the valence band must be partially emptied through doping of holes. Electron doping can be realized by intercalation of alkali metals (A) into the fullerene cage [190]. Such compounds of the type A_3C_{60} become metallic and even superconducting at low

temperature [191, 192].

Fullerenes in the solid state may exhibit another interesting phenomenon - the polymerization effect [194, 195, 196]. Under the influence of light or high pressure and high temperature, individual fullerene molecules in the solid may become joint to their neighbors through covalent bonding. As a result, a strongly anisotropic electronic structure of reduced dimensionality may appear in such molecular crystals. In addition to the aforementioned superconductivity, another fascinating effect was discovered: ferromagnetism of polymerized fullerite. Appearance of magnetic ordering has been recently demonstrated in the anisotropic rhombohedral fullerene polymer Rh-C_{60} [193].
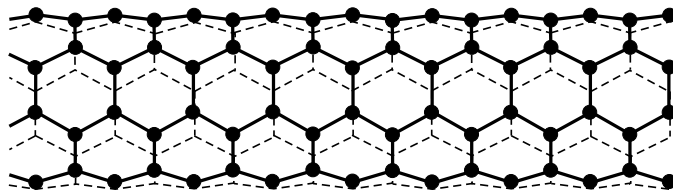

Figure 4.16: Structure of the single wall carbon nanotube (SWNT), side view.

The fullerene family includes another exciting example of carbon nanostructures - the nanotubes. They are cylindrical molecules with diameters ranging from several to tens of Ångström and length of up to hundreds of micrometers. The nanotubes, discovered in 1991 [197], appear to be the most perfect realization of a physical object with distinct one-dimensional atomic and electronic properties. The structure of a nanotube can be understood as a cylindrically wrapped graphite sheet. Fig. 4.16 gives an idea of the nanotube structure. Basic molecules, which are built of only one convoluted graphite layer are called single wall nanotubes (SWNT), while tubes which have the structure of a "russian-doll" involving several nanotubes taken up inside of each other are named multi wall carbon nanotubes (MWNT). MWNT's are especially interesting because of their shell selected conductance and dependence of the electronic properties on the number of shells [198]. In the last years the nanotubes have attracted a colossal interest, because they have successfully been applied in nanotechnology [199, 200, 201]. In particular, fabrication of a voltage invertor, which is in fact an elementary computer circuit, has been achieved by realization of two field effect transistors (FET) on a single nanotube [202].

At the same time, experiments with nanotubes as well as their industrial application experience significant difficulties. The nanotubes, as opposed to the simple fullerenes (like archetype C_{60}), cannot be placed and arranged on the substrate in an accurate and chemically "clean" way - their deposition in most cases is performed from organic solutions. Just recently a novel dry-contact method of *in situ* deposition has been developed [203]. With respect to that, phenomena of low-dimensional self-organization between the simple fullerenes like C_{60} became highly interesting. If one succeeds in producing one- or two-dimensional ordered nanostructures of C_{60} (which might be suggested under vacuum conditions on

a well characterized periodic substrates) and achieve polymerization, fascinating low-dimensional objects can be produced. Likewise, formation of molecular nanostructures of archetype fullerenes is interesting by its own with respect to their joint electronic properties or their nanomagnetism. For example, self-organization of fullerenes, intercalated with magnetic materials may provide unique effects of magnetic ordering between the incorporated atoms which reside in the structural matrix of the molecular cluster being separated by carbon shells.

Another important aspect of fullerene transport and self assembly is related to cluster engineering. In a number of works the phenomenon of fullerene defragmentation under the influence of temperature, photon, ion or electron beam has been demonstrated [204, 205]. This effect is very important for nanoapplications, because it makes possible to fabricate atomic clusters of carbon in different allotropic forms (i.e. carbine, graphite) on a variety of substrates with strictly pre-determined atomic count and dimensions.

In the forthcoming part of the present Thesis a fairly new phenomenon of template-induced self-organization of archetype fullerene molecules C_{60} into "magic" (perfectly uniform) van der Waals clusters and aligned cluster chains will be reported. As a substrate for C_{60} deposition the two-dimensional surface carbide W(110)/C-R(15×3), has been used. It has dimensions of the unit cell (8Å×13Å) comparable to the 10Å-shell of C_{60}. Electronic structure and surface geometry of the surface carbide are well understood and have already been described in detail in the previous Section.

The appearance of "magic numbers" is among the most intriguing issues of self-organization phenomena. Their existence has been revealed in many systems of different nature. Actually, fullerene themselves are a very prominent example of such self-organization : the number of carbon atoms in the molecule n is a typical "magic number" since in stable clusters only particular values like 26, 28, 60, 70 etc. are allowed [183]. Magic numbers have also been observed for many metal cluster systems and were recently observed for gases. It has been show that He atoms tend to produce He_n clusters with n=0, 14, 22, 44 [219]. Similar phenomena were observed also in two-dimensional systems, where the formation of perfectly uniform metallic nanoclusters on a Si(111)-(7×7) template was achieved [220, 221]. So far, such effects on atoms are widely studied and generally understood, only a few reports on self-organization of fullerenes has been published [213] and no study at all on two-dimensional clustering. The first observation of such system is presented in this Thesis.

In the forthcoming Section, an STM study of C_{60} self-organized on the tungsten surface carbide into molecular clusters with 4 and 7 molecules is reported. For higher coverages an alignment of these clusters to the template and formation of cluster chains occurs. Furthermore, the thickness-dependent electronic structure of C_{60} on the surface carbide studied with photoemission is compared with C_{60} on clean W(110). Since PES displays no effect of charge transfer, formation of clusters [210, 211, 212, 213] will be considered as self-organization effect in a two-dimensional molecular gas in terms of the van der Waals formalism [214, 215, 216, 217, 218].

In order to describe the observed phenomena, a model calculation of the total cluster potential will be performed in the framework of the Girifalco approach [214] with Lennard-Jones interatomic potential [215] for static cluster configurations. The geometry provided by the calculations agrees well with the structures observed experimentally.

4.3.2   Experimental details

Experiments have been done at a base pressure below 1×10^{-10} mbar. Self-organization of the clusters has been systematically studied in dependence of the coverage by STM. Photoelectron spectroscopy has been used in order to check the electronic structure of clusters and the interaction between adsorbed fullerenes and the substrate.

The surface-carbide W(110)/C-R(15×3) was used as template. It has been prepared in the standard way [224] described in the preceding Sections of this work. Sub-monolayer amounts of C_{60} were evaporated *in situ* from a heated quartz crucible at a low deposition rate of $2-40 \times 10^{-3}$ ML/min. The amount of deposited C_{60} has been carefully controlled with an oscillating quartz microbalance, calibrated by the STM and PES. After deposition, STM measurements were started typically within 10-15 minutes. Clustering of C_{60} has been found to take place at room temperature along with the deposition. All measurements have been performed at 300K.

The preparation procedure of the STM tip must be emphasized. Electrochemically etched polycrystalline W tips were initially cleaned *in situ* by Ar^{+} sputtering, annealed at nearly 2000°C and reformed by autoemission at 4kV [232]. For imaging of C_{60} nanoclusters they were, however, modified. In particular, a single fullerene molecule was "caught" at the apex and used as a tip itself. In multiple experiments it was revealed that sub-ML films of C_{60} *cannot* be realistically imaged with clean W tips on a surface carbide. Corrugations measured in this way by STM exhibit a chaotic topography [233], which can be attributed to the chemical interaction which is stronger between the tip and adsorbed C_{60} than between C_{60} and the template. Note that similar problems were reported before for "as deposited" fullerenes on a Si substrate [234]. The only way to obtain a physically justified STM characterization in the present experiment was to "passivate" the tip apex with one (or several) C_{60} molecules which can be picked up from the surface by voltage impulses of about ± 500 mV. Fig. 4.17 illustrates this technique.

PES measurements were done at the BESSY beamlines U125/1-PGM [235] and U56/1-PGM [236] using the hemispherical analyser VG ESCAlab at 80 meV energy and 1° angle resolutions (see Chapter 1).
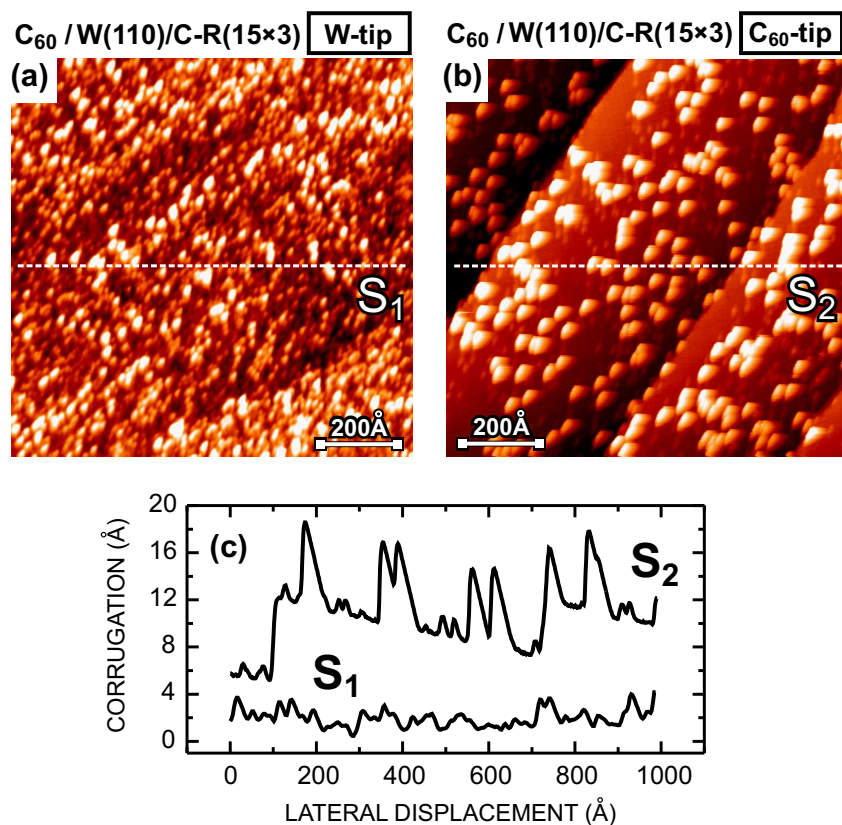
(a) C_{60} / W(110)/C-R(15×3) | W-tip

S₁ S_1

200Å

(b) C_{60} / W(110)/C-R(15×3) | C_{60}-tip

S_2

200Å

(c) CORRUGATION (Å)

S_1

S_2

LATERAL DISPLACEMENT (Å)

Figure 4.17: STM imaging of the self-assembled C_{60} nanoclusters on the surface carbide using two different types of tips; (a) clean polycrystalline W tip gives an unstructured scan S_1 with low corrugation profile (c); (b) C_{60} caught at the tip apex now works as a tip itself. The topography of the image is drastically improved becoming now more physical and resolving even the substrate. The scan profile S_2 also gives significantly increased corrugation (c).

105

4.3.3 Results

STM characterization of self-assembled fullerene nanoclusters

STM images of C_{60} on the surface carbide are presented in Fig. 4.18. The topography signal Z has been recorded in mixed Z/I mode with a single fullerene molecule at the tip. Images in Fig. 4.18 represent a spatial distribution of the unoccupied LDOS near the Fermi level E_F, as tunneling through the barrier has been set from the tip to the sample at a positive sample bias of about +200 mV . Characteristic corrugation profiles S_{1-4} of the clusters are given below (Fig. 4.18(e)). The vector basis $(V_{\parallel},V_{\perp})$ of the surface carbide was introduced earlier (Fig. 4.2) and will be used also here for description of the cluster geometry. These vectors are marked in each scan in Fig. 4.18. Because dimensions of the template surface cell are unambiguously known, an absolute calibration for the STM is possible. To remind the reader, the STM measurements of the surface carbide reveal the periodicity of the R(15×3) superstructure as 8Å along $V_{\parallel}$ and 13Å in the direction $V_{\perp}$ (Fig. 4.3).

Structural configuration and dimensions of the self-assembled clusters depend strongly on the amount of deposited C_{60}. At low coverage ($\leq$0.2 ML) only small and slightly elongated clusters with distinct diameter of 25 Å (Fig. 4.18(a), mark "K_{low}") have been observed. Increasing the deposited amount of fullerenes (0.3-4 ML) leads to the appearance of large clusters with dimensions of $\sim$ 50 Å (Fig. 4.18(b), mark "K_{high}"). No other shapes and dimensions of individual clusters have been observed, therefore one can claim these two phases as basic which will be referred to further as *low-* and *high*-configuration (K_{low} and K_{high}) of small and large clusters, respectively.

Further increase of C_{60} deposition causes a rather unexpected phenomenon, which can be named cooperative self-assembly. Fig. 4.18(c) shows an example of this effect on the K_{low} clusters. Here, at a total coverage 0.4 ML and low deposition rate the low-configuration clusters gain a complicated macro configuration through the junction of two extra C_{60} molecules to their opposite sides, which starts to look like a short cluster chain. Note that this chain is oriented along [001] of W and is not correlated to the $V_{\parallel,\perp}$ directions of the carbide template.

The same effect of cooperative self-organization was observed for K_{high}-clusters at 0.5 ML coverage. It reveals a distinctly different grouping of the self-assembled clusters (shown in Fig. 4.18(d)). Four fullerene clusters form now chains of identical length. Each of them incorporates one K_{high}-cluster as well as three K_{low} on the sides. The chain gains a total length of $\sim$ 120Å being, as opposed to Fig. 4.18(e), now aligned to the carbide stripes i.e. to the $V_{\parallel}$ direction of the template.

From the STM data in Fig. 4.18 it is easy to see that bigger clusters always appear much brighter in the topography. Analysing the absolute amplitude of corrugation in the characteristic profiles S_{1-4} from Fig. 4.18(h), one finds that the detected topography height of the K_{high}-cluster is about 8 Å, while for K_{low} this value is smaller: $\sim$ 6 Å. The corrugation from the single C_{60} molecule observed in Fig. 4.18(e) is even less: $\sim$ 3-4Å.
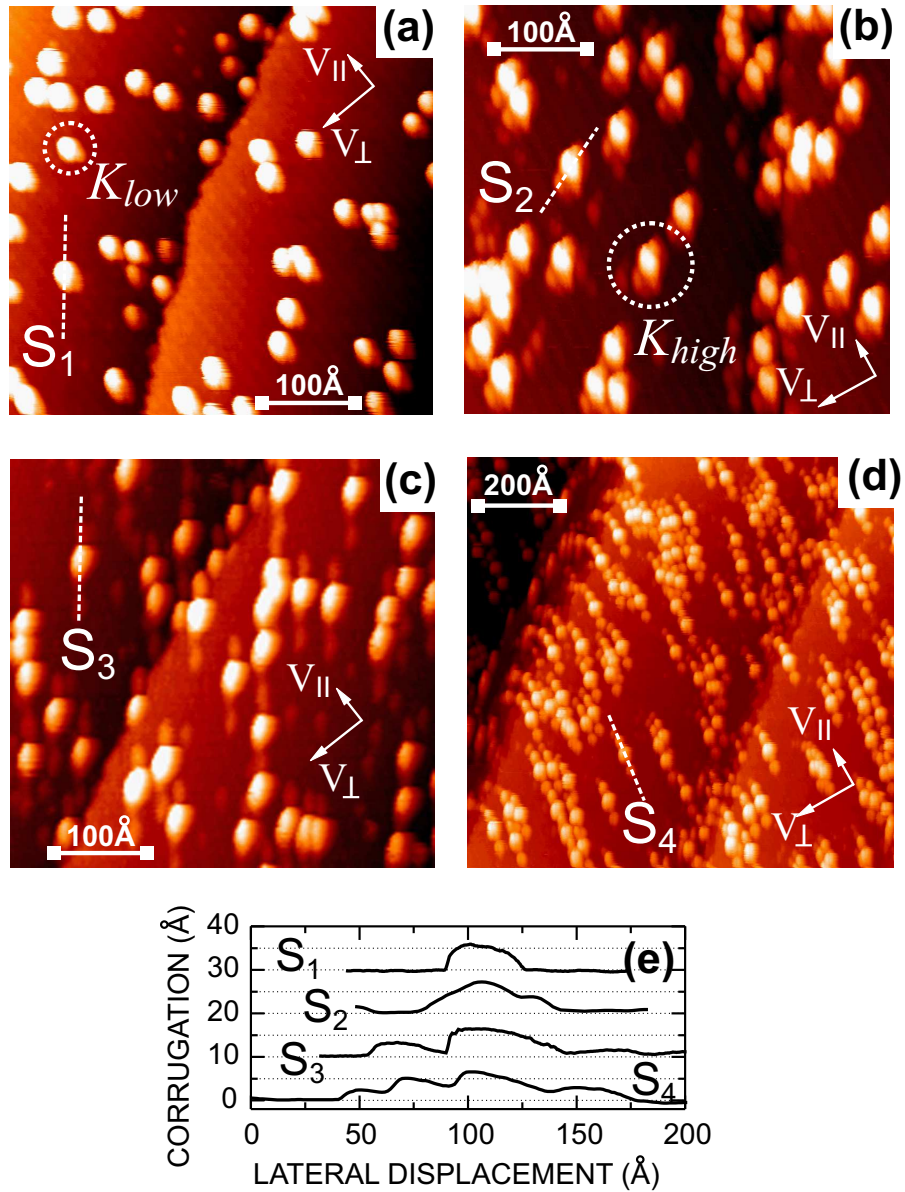
Figure 4.18: STM study of the self-organized fullerene nanostructures on the template W(110)/C-R(15×3) at low positive sample bias +200 mV; (a) K_{low} cluster configuration appears at low coverage ($\leq$0.2 ML); (b) larger clusters K_{high} are formed at increased coverage (0.3 - 0.4ML); (c) cooperative self-organization of K_{low}-clusters; (d) cooperative self-assembly of K_{high}-clusters leads to formation of cluster chains; (e) characteristic profiles of corrugation over the clusters from figures (a)-(d).

107

Indeed, the changes in the STM corrugation can happen because of two reasons; (a) "real" topographical variation of the potential relief, and (b) increasing of tunneling current as a result of changes in the local density of states (LDOS). In some previous STM reports it has been shown, that the fullerene can appear "bright" and "dark" [237, 238] and even exhibit a geometrically deformed cage [239] which depends on the particular environment of the adsorption site. In the current experiment the observed corrugations are related to differences in the electronic structure of the single C_{60}, K_{low} and K_{high} clusters. From the data presented in Fig. 4.18 where the unoccupied LDOS in the nanoclusters is mapped, it is possible to conclude that decrease of the LDOS at E_F is collective and larger in the big clusters than in the small ones and individual adsorbed C_{60}. In order to prove unambiguously, that the apparent height of the clusters is a pure effect of the electronic structure, in Fig. 4.19(a) the topography of the *occupied* LDOS is demonstrated, which has been recorded at reverse sample bias of –200 mV. The characteristic profile S_5 is shown in Fig. 4.19(b) compared with the corrugation S_4 along the cluster chain from Fig. 4.18(d). While the maximum of the tunneling signal recorded at positive bias +200 mV belongs to the central cluster, the maximal corrugation for reversed polarity falls on the end of the chain. This clearly proves the assumption that real topographic relief has less to do with the detected heights of the clusters. Such anisotropy in the occupied LDOS along the cluster chain is an interesting point and will be discussed later.

In addition it is important to remark a comparative STM measurement of C_{60} on *clean* W(110). The performed studies (not reported here) did not reveal any appearance of the uniform clusters, but rather the formation of arbitrary large islands of the fullerene film. One can be absolutely confident that the effects of self-assembly, internal structure as well as electronic properties of the C_{60} nanoclusters are explicitly determined by the R(15×3) template of the surface carbide.

Photoemission study of C_{60} on the surface carbide

Fig. 4.20 demonstrates photoelectron spectra of fullerenes on a surface carbide for different amounts (from 0.3ML to 2ML) of deposition. Photoemission was measured in a direction nearly normal to the substrate. For comparison, spectra from the same amounts of C_{60} deposited onto the *clean* W(110) are shown in the diagram by dotted lines. Note that the whole electronic structure of fullerenes on the clean tungsten shows a remarkable energy shift $\delta E=0.45$ eV towards higher binding energies. This effect has been already understood on a variety of metallic substrates [208, 240] and attributed to charge transfer from the metallic surface to C_{60}. For clarity of the analysis, the dotted spectra of 1ML and 2ML C_{60} in the diagram are referred to the binding energies of HOMO-3 and HOMO-2 molecular orbitals.

One can see in Fig. 4.20, that HOMO-2 of C_{60} on clean W(110) (dotted line) has the same binding energies for 1ML and 2ML coverage. However, the electronic structure of ≤1ML C_{60} on the surface carbide (solid line) is obviously different than that of 2ML. For 1ML HOMO-2 has a shift $\delta H=0.46$ eV towards *lower* binding
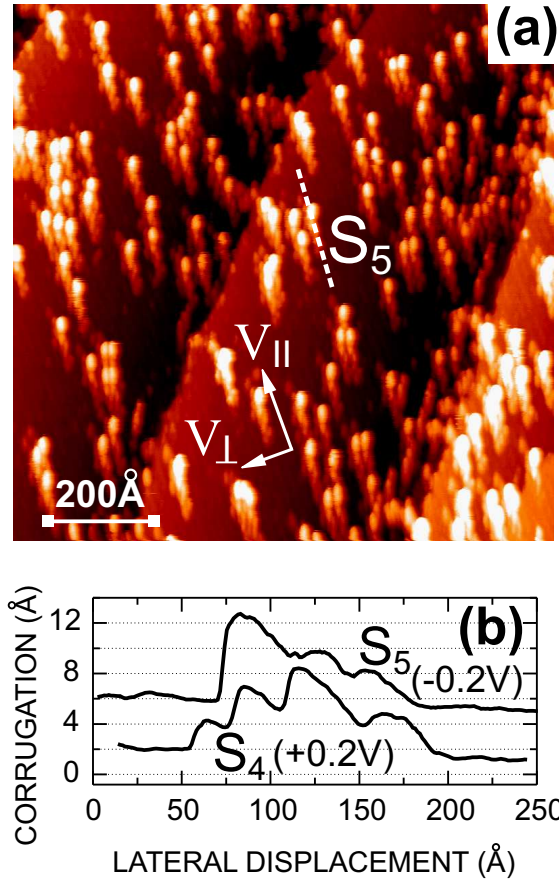
Figure 4.19: (a) STM imaging of the cluster chains shown in Fig. 4.18(d) performed at negative sample bias –200 mV reveals the maximum of the *occupied* LDOS concentrated at the end of the chain. This proves that corrugation differences are purely determined by the electronic structure of the clusters, but not by the potential relief; (b) quantitative comparison of a profile section measured along the chain at the sample bias –200 mV (S_5) with a profile of the chain form Fig. 4.18(d) taken at +200 mV (S_4).
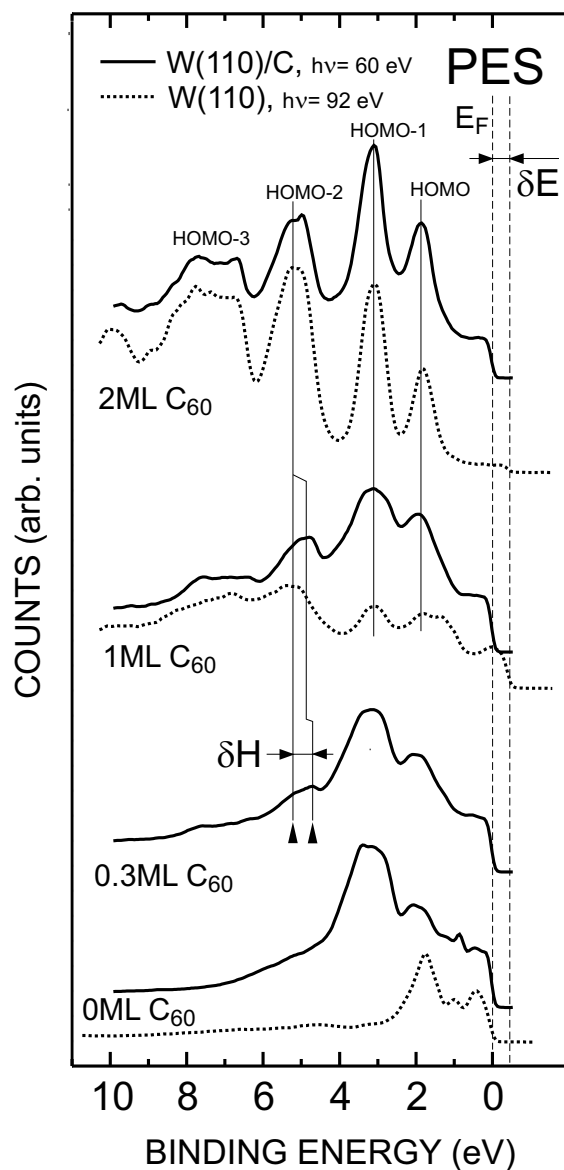
Figure 4.20: PES study of C_{60} nanoclusters. The comparative study shows that 1ML and 2ML of C_{60} on *clean* W(110) have the same electronic structure (dotted spectra) and reveal common charge transfer W $\rightarrow C_{60}$ which appears as energy shift δE. As opposed to that, photoemission from sub-ML amounts of C_{60} (solid line) exhibits an internal modification of the C_{60} electronic structure which appears as shifted (and apparently split) peak HOMO-2.

energies. At the sub-ML amounts of fullerenes this shift is even larger, reaching 0.52 eV and the peak appears split, which manifests a partial depopulation of the HOMO accompanied by local pinning of the Fermi level. This point is presumably related to the formation of basic cluster configurations observed by the STM.

4.3.4 Discussion

What is the driving force of self-organization?

First of all, the question to be answered is: what is the driving force of the observed self-organization? The observed self-assembly suggests a high mobility of the individual fullerenes on the R(15×3) template at 300K due to the low-energy of molecule-substrate interaction. Since the photoemission study of C_{60} on the surface carbide reveals no effects of charge transfer (Fig. 4.20) no strong chemical bonding takes place between adsorbed fullerenes and the carbon-passivated W(110). The only bonding which involves no electron exchange is van der Waals [216] dipole interaction between slightly polarized molecules or atomic clusters. Referring back to the distance-dependent STM study of W(110)/C-R(15×3) (Fig. 4.3), the dangling bonds of p-orbitals over the zigzag chains of carbon and ionic polarization of the carbide overlayer as well [241, 243] may cause an induced polarization of adsorbed fullerenes [244, 245, 246]. In order to evaluate the energy of interaction between the single C_{60} and the substrate, the same approach used for characterization of fullerenes on graphite sheets has been used. Since photoemission detected no drastic influence of the W substrate on the electronic structure of C_{60}, and STM revealed dangling bonds over carbon atoms in W(110)/C-R(15×3) (similar to p_z-orbitals in graphite) the carbide overlayer can be considered as graphite sheet with particularly different arrangement of atoms.

Model calculations

A Ruoff-Hickman potential adopted by Girifalco [216, 214] was used for model calculations. Girifalco considers C_{60} as a hollow sphere of radius R_{mol} =0.355 nm with carbon atoms uniformly distributed over the surface (Fig. 4.21(a)). Such model representation is fully justified for room temperature, when fullerene molecules are freely rotating either on a substrate or in a van der Waals lattice. The C-C interaction is described by the Lennard-Jones potential [215] which has a form [216]:

(4.2)
$$U_{cc}(r) = \frac{C_{12}}{r^{12}} - \frac{C_6}{r^6}$$

where r denotes the distance between two carbon atoms, C_{12}=3.4812×10^{-8} [eV·(nm)^{12}] and C_6=1.997×10^{-5} [eV·(nm)^6] [214, 217]. The interaction potential between the hollow C_{60} and a single carbon atom of substrate, is then evaluated as:
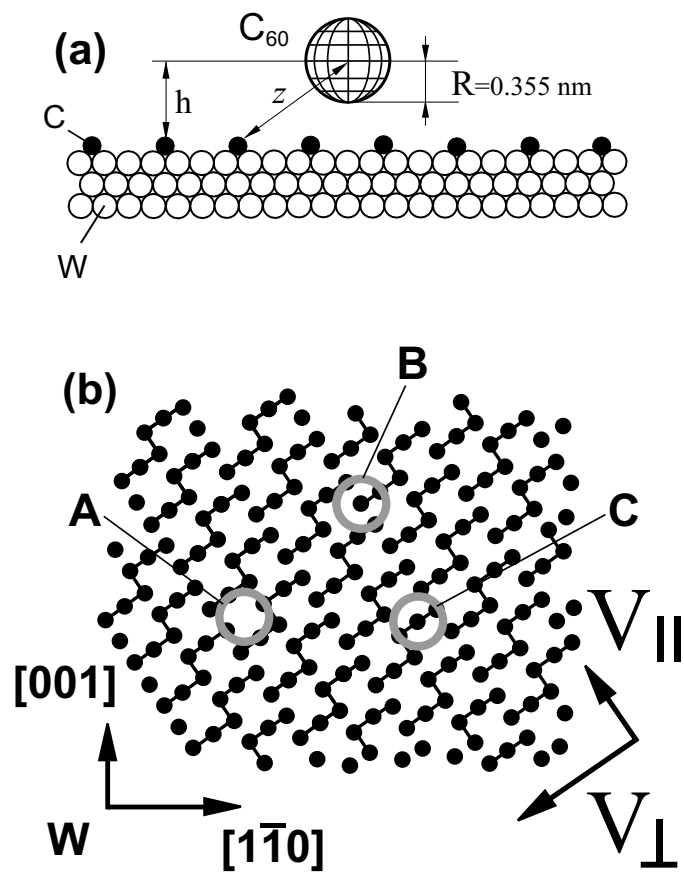
Figure 4.21: Modeling C_{60} adsorption on a surface carbide W(110)/C-R(15×3); (a) in van der Waals formalism the adsorption distance h=7 Å is assumed to be twice as large as the radius of the fullerene cage R_{mol}=3.55 Å; (b) A, B, C - possible adsorption sites with increased symmetry.

Table 4.2: Energy of van der Waals interaction between C_{60} and the R(15×3) matrix of carbon atoms calculated for different adsorption sites in dependence of the molecule elevation h over the template.

h[Å]	U_{subst} in A [eV]	U_{subst} in B[eV]	U_{subst} in C[eV]
5	+0.635	+63.6	+62.5
6	-0.101	+0.161	+0.152
7	-0.0735	-0.0727	-0.0732

(4.3)
$$U_{mol}(Z) = V_{12}(Z) - V_6(Z)$$

where

(4.4) $$V_n(z) = \frac{C_N}{2(n-2)} \frac{N}{(R_{mol} \cdot Z)} \times [\frac{1}{(Z - R_{mol})^{n-2}} - \frac{1}{(Z + R_{mol})^{n-2}}]$$

Here N is the number of carbon atoms in a hollow sphere (N=60), R_{mol}=0.355 nm denotes the radius of the fullerene atomic cage, and Z means the distance between the molecule and a carbon atom of the substrate (see Fig. 4.21(a)). The total interaction energy between the molecule and the plane of carbon atoms U_{subst} is then obtained by integrating $V(Z)$ over all atoms in the plane. In the present report this has been done numerically for a (30×30) matrix of carbide surface lattice. The interaction energy has been evaluated for three possible adsorption sites with high-symmetry environment, which are A, B and C as shown in Fig. 4.21. The values of the adsorption energy calculated for different elevations h of the molecule over the surface of the template are summarized in Table 4.2.

It is evident from Table 4.2 that site A is predominant for adsorption, since the interaction energy there is always minimal. Moreover, the absolute values of U_{subst} demonstrate that the most probable elevation h is about 7 Å. While the lower elevations give physically meaningless values of the interaction potential, the energies, calculated for $h = 7$ are about -0.1 eV being always negative. This is fully justified for van der Waals interactions. In addition, $h = 7$ is exactly the elevation of C_{60} adsorbed on a graphite sheet [217, 218]. Thus, this value will be used in the following. So far it was evidently shown that different heights of the clusters detected by STM are purely an electronic effect (Figs. 4.18 and 4.19). Therefore, the fullerene clusters will be considered as flat, i.e. two-dimensional assemblies of C_{60} which are 1 ML thick. With respect to this, the observed clusters can be interpreted as self-organized with "magic numbers" in a *two-dimensional molecular gas* using the simplified method of static cluster configuration instead of a molecular dynamics approach [222] (which is the subject for further analysis, not in the frame of this work). In particular, the static method suggests the analysis of the

most probable cluster configurations selected from symmetry considerations and calculation of the total energies of intermolecular interactions. Then the energies of the most favorable configuration must be analyzed as a function of N (where N denotes the number of fullerenes in the cluster) and the energetically profitable N can be revealed from the behavior of the second finite difference of the total energy [210].

Since the problem of potential determination has a probabilistic character due to the rotational freedom of C_{60}, all calculations were performed using an approach of the Monte-Carlo method i.e. calculating and averaging the energy of interaction between the molecules for up to 1000 randomly selected orientations of the molecular cages.

Calculations of cluster energy have been performed using the same Lennard-Jones pairwise additive atom-atom potential U_{cc} given in Eq. (4.2). To obtain the interaction energy between two different fullerenes (denoted as α and β), this atomic potential must be integrated over all mutual pairs of carbon atoms:

$$(4.5) \qquad U_{\alpha\beta} = \sum_{i=1}^{60} \sum_{j=1}^{60} \left(\frac{C_{12}}{(r_{ij}^{\alpha\beta})^{12}} - \frac{C_6}{(r_{ij}^{\alpha\beta})^6} \right)$$

Summarizing $U_{\alpha\beta}$ over the pairs of C_{60} in the cluster one gains the total potential of interaction:

$$(4.6) \qquad U_{total} = \frac{1}{N} \cdot \sum_{\alpha=1}^{N-1} \sum_{\beta=\alpha+1}^{N} U_{\alpha\beta}$$

After the molecule elevation h is established, another important question must be answered. How big is the lateral separation between molecules in the cluster and what is the influence of the R(15×3) template? Fig. 4.22 demonstrates the modulation of the tunneling current recorded simultaneously with the STM image presented in Fig. 4.18(b). Since the current channel is more sensitive to the corrugation amplitude it gives an idea about the internal structure of the cluster K_{high}. One can evidently see that the cluster consists of fullerene chains aligned to the $V_\parallel$ direction of the substrate. The measured separation between the chains coincides with the periodicity of the surface carbide unit cell in the $V_\perp$-direction being equal to 13 Å. As for the molecule separation along $V_\parallel$ (i.e. periodicity inside the chain) the situation is more complicated, since it was not resolved by STM. This value should be evaluated from interaction energy calculations. Neither a separation which is equal to the periodicity of the R(15×3) template along $V_\parallel$ (8 Å) nor the double periodicity (16 Å) provides a reasonable energy of the molecule interaction. At a separation of 8 Å the van der Waals formalism is not usable at all, since electron cages of C_{60} (~ 10 Å) should already be overlapping. On the
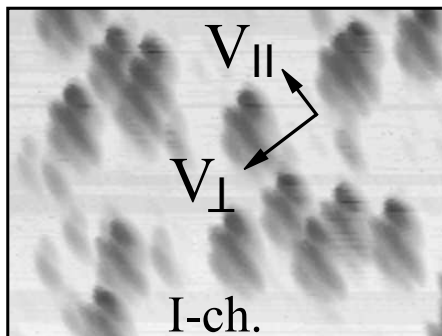
Figure 4.22: Modulation of the STM current recorded simultaneously with Fig. 4.18(b). The internal anisotropic structure of clusters is perfectly resolved - they consist of fullerene chains aligned to the $V_\parallel$ direction of surface carbide.

other hand, the distance of 16 Å appears to be too large: the C_{60}-C_{60} interaction is then about one order of magnitude weaker than the interaction between the molecule and the substrate, which would fully disprove the principle idea of cluster existence.

Preliminary calculations revealed that a physically justified separation is 13.2 Å, which is 3/2 of the R(15×3) template periodicity in the $V_\parallel$-direction. This value also agrees with the separation along $V_\perp$, and appears to be very reasonable, since it is comparable with the lattice constant of the van der Waals face-centered cubic (f.c.c.) crystal of fullerite (14 Å). The fact that some fullerenes in the cluster appear to be adsorbed not at sites A but rather at sites C (Fig. 4.21) does not seriously affect the result of the calculations. The point is that the intermolecular interactions obtained for lateral separations of about 13 Å are 4-5 times stronger than the C_{60} interaction with the substrate. However, the environment of the template may slightly affect the electronic structure of fullerenes: this will be further discussed below.

A variety of geometrical configurations of clusters has been calculated. Selected results are reported in Fig. 4.23. The total energy of interaction (calculated per molecule) is plotted for different numbers of C_{60} (N=2-8) and different structure of clusters. Selected configurations (characterized with minimal and maximal values of the energy) are shown in the insets near the data points. Binding energies (total energies with opposite sign) of the most stable structures are plotted in Fig. 4.24(a) as a function of N. On can clearly see that the binding energies which correspond to "magic numbers" N=4 and N=7 are increased. This effect is more evident in Fig. 4.24(b), where the plotted second finite difference of the total energy $\Delta_2 E = E(N+1)+E(N-1)-2\cdot E(N)$ exhibits two evident peaks. Thus, the theoretical evaluation suggests that the cluster configuration K_{low} incorporates 4 C_{60} molecules, while K_{high} has 7 molecules in its structure. Molecule layouts of "magic" clusters used in calculations for $N = 4$ and N=7 are shown in detail in Fig. 4.25(a). Note that also the layouts are in good agreement with experiment. Unfortunately, it is difficult to establish from STM data the exact inner layout, since individual

molecules cannot be resolved. This can be hardly related to the tip quality which was actually a single fullerene molecule (Fig. 4.17). Two explanations are offered. Firstly, the charge cage of C_{60} arranged in rows along the direction $V_\parallel$ can be deformed [239] by the anisotropic potential of W(110)/C-R(15×3), which leads to a decrease of the detectable separation. Another reason is method-related. Since the lateral separation between molecules inside the rows is 3/2 of the R(15×3) lattice constant, it comes out that every second C_{60} will be adsorbed on the template at the energetically non-favorable site C (Fig. 4.21(b), Fig. 4.25(a) and Table 4.2). This, in particular, means that such molecules are less stable and can be brought to lateral movement along $V_\parallel$ by the STM tip. In such case the STM image of rows will obviously be blurred. The way to improve the resolution is to measure C_{60} on a surface carbide at low temperatures. This is a forthcoming task, however one should be aware that self-organization of fullerenes may be affected since the heat factor kT seems to be very important for the mobility of C_{60} on the template. Nevertheless, although molecular resolution is not achieved (likely because of the physical properties of the investigated object) the assumed dimensions and the shape of the clusters are well correlated with those observed by STM (Fig. 4.18(a) and (b)).

One more question to answer is what the reason is for the variations in the electronic structure of clusters detected by STM and PES. Depopulation of the LDOS at Fermi level resulting in the split and shifted peak HOMO-2 (Fig. 4.20) can be explained as being a result of different environment of the adsorption site. So far almost one half of the molecules in the clusters are adsorbed at sites A (Fig. 4.21), another half is placed at sites C i.e. over zigzag chains of the carbide template where dangling bonds were detected (Fig. 4.3). This causes different polarization of molecules resulting in local changes of the electronic structure. Such situation is very similar to the case of graphite, where STM shows a three-fold symmetry of the image instead of a six-fold one (Fig. 1.11). The fact is that only three atoms out of six in the graphitic hexagon have neighbors with a dangling bond p_z in the underlying plane. This causes localization of occupied LDOS on these atoms while empty states are distinct to the other three [223]. A very similar influence of dangling bonds on the electronic structure of the C_{60} cluster can be present in our case. In particular, the local electronic structure can change from one molecule to another, but it is always a question how the STM tip will detect these variations.

Self-organization of cluster chains

The observed effects of cooperative self-organization of the clusters (Fig. 4.18(c,d)) which takes control over the cluster arrangement are more complicated but likely have the same electrostatic nature. It is possible to assume the appearance an *inter-cluster* interaction at higher C_{60} coverages. At some point, the mean lateral distance between the clusters becomes short enough to allow for intercluster van der Waals forces to play a role. As a result, formation of every next cluster becomes energetically more efficient in the direct neighborhood to the existing one. Substantial clustering appears to be linearly arranged. Although cooperative
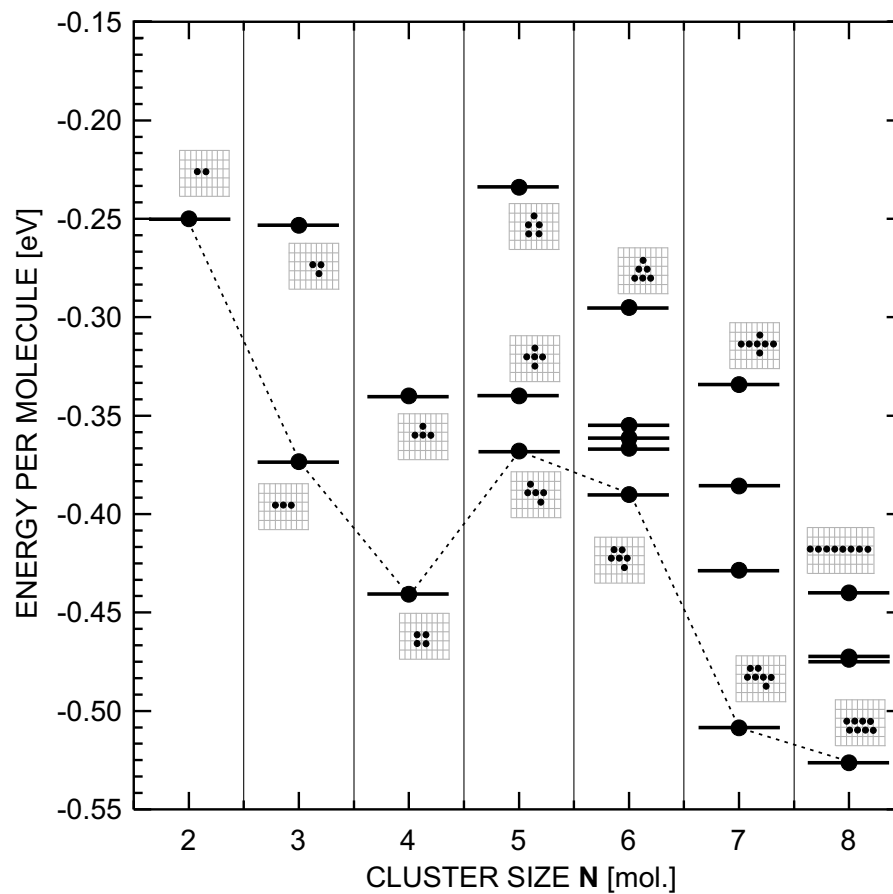
116

Figure 4.23: Static method: total energies (per molecule) of van der Waals interaction calculated for different configurations of clusters using Girifalco's spherical potential.
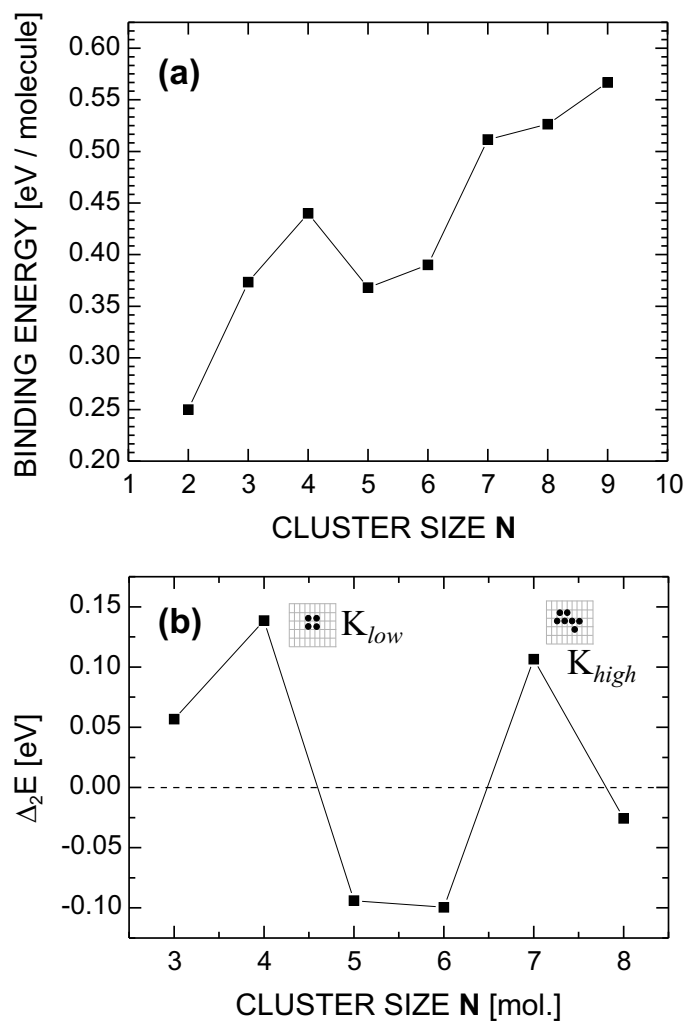
Figure 4.24: Binding energies (a) and second finite differences of total energies (b) of $(C_{60})_N$ clusters with energetically favorable configurations.

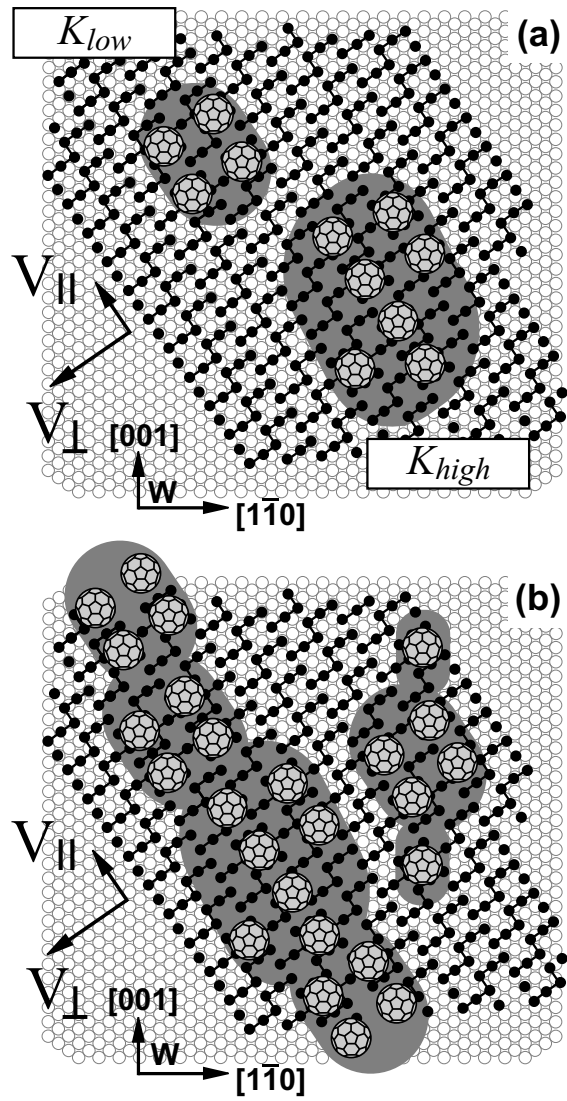Figure 4.25: (a) molecule arrangements in the basic clusters K_{low} and K_{high} given by calculations and confirmed by experiment. Buckyballs C_{60} are shown in gray; (b) proposed structure for cluster chains observed in Fig. 4.18(c) and (d).

self-organization can be described in the same van der Waals formalism as used above, a more sophisticated non-static model is desired which is not the topic of this Thesis. Nevertheless, the structure of cluster chains extracted from a careful analysis of STM data is given in Fig. 4.25(b)

In summary, a study of template-induced self-organization of C_{60} on a surface carbide W(110)/C-R(15×3) has been performed. STM measurements have revealed that deposited fullerenes exhibit self-assembly into perfectly uniform van der Waals molecular nanoclusters. For description of this phenomenon a formalism of two-dimensional fullerene gas was proposed. The existence of basic cluster configurations with "magic numbers" has been proved by model calculations of total interaction energy in Girifalco's approach. At increased coverage a cooperative effect of macro self-organization leading to formation of aligned uniform cluster chains has been observed.

4.4   Summary of conclusions

Summarizing, the following conclusions were made in this Chapter. Firstly, an advanced structural model of two-dimensional tungsten carbide W(110)/C-R(15×3) is developed: the superstructure of carbon atoms, which has dimensions (13 Å × 8 Å), is embedded into the first monolayer of W. It leads to a non-diffuse bulk termination and provides a specifically new surface state at 0.7 eV binding energy, which was detected by photoemission. This surface state at 0.7 eV is laterally quantized in the direction parallel to the long side of the surface carbide unit cell. This is a clear evidence of one-dimensional buckling of W(110)/C-R(15×3) which imparts the substrate a quasi-stepped character.

Combined STM and PES studies have demonstrated that the W(110)/C-R(15×3) is a promising template for self-organization of nanostructures. At elevated temperature it provides self-organization of Au clusters and nanowires which are 1 nm wide. These self-assembled Au nanowires have distinct one-dimensional electronic structure featuring lateral quantum well states in d-bands. Such quantization is well described in terms of a one-dimensional particle-in-a-box approach.

Beyond this, W(110)/C-R(15×3) controls the self-organization of archetype fullerenes C_{60} into uniform molecular nanoclusters with "magic numbers". Since the distance-dependent STM has revealed that tungsten surface carbide W(110)/C-R(15×3) is ionically polarized featuring dangling bonds over carbon atoms, and no effects of charge transfer between adsorbed molecules and the substrate were found in PES, van der Waals interaction has been assumed as driving force of the self-organization. Static model calculations with Lennard-Jones potential of C-C interaction reveal two stable cluster configurations with 4 and 7 molecules. These results are in good agreement with the experimental data.

Summary

The Thesis is focused on the properties of self-organized nanostructures. Atomic and electronic properties of different systems have been investigated using methods of electron diffraction, scanning tunneling microscopy and photoelectron spectroscopy. Implementation of the STM technique (including design, construction, and tuning of the UHV experimental set-up) has been done in the framework of present work. This time-consuming work is reported to greater detail in the experimental part of this Thesis.

The scientific part starts from the study of quantum-size effects in the electronic structure of a two-dimensional Ag film on the supporting substrate Ni(111). Distinct quantum well states in the sp-band of Ag were observed in photoelectron spectra. Analysis of thickness- and angle-dependent photoemission supplies novel information on the properties of the interface. For the first time the Ni(111) relative band gap was indirectly probed in the ground-state through the electronic structure of quantum well states in the adlayer. This is particularly important for Ni where valence electrons are strongly correlated. Comparison of the experiment with calculations performed in the formalism of the extended phase accumulation model gives the substrate gap which is fully consistent with the one obtained by ab-initio LDA calculations. It is, however, in controversy to the band structure of Ni measured directly by photoemission. These results lend credit to the simplest view of photoemission from Ni, assigning early observed contradictions between theory and experiments to electron correlation effects in the final state of photoemission.

Further, nanosystems of lower dimensionality have been studied. Stepped surfaces W(331) and W(551) were used as one-dimensional model systems and as templates for self-organization of Au nanoclusters. Photon energy dependent photoemission revealed a surface resonance which was never observed before on W(110) which is the base plane of the terrace microsurfaces. The dispersion E($\mathbf{k}$) of this state measured on stepped W(331) and W(551) with angle-resolved photoelectron spectroscopy is modified by a strong umklapp effect. It appears as two parabolas shifted symmetrically relative to the microsurface normal by half of the Brillouin zone of the step superlattice. The reported results are very important for understanding of the electronic properties of low-dimensional nanostructures.

It was also established that W(331) and W(551) can serve as templates for self-organization of metallic nanostructures. A combined study of electronic and atomic properties of sub-monolayer amounts of gold deposited on these templates have shown that if the substrate is slightly pre-oxidized and the temperature is elevated, then Au can alloy with the first monolayer of W. As a result, a nanostructure of uniform clusters of a surface alloy is produced all over the steps. Such clusters feature a novel sp-band in the vicinity of the Fermi level, which appears split into constant energy levels due to effects of lateral quantization.

The last and main part of this work is devoted to large-scale reconstructions

on surfaces and nanostructures self-assembled on top. The two-dimensional surface carbide W(110)/C-R(15×3) has been extensively investigated. Photoemission studies of quantum size effects in the electronic structure of this reconstruction, combined with an investigation of its surface geometry, lead to an advanced structural model of the carbide overlayer.

It was discovered that W(110)/C-R(15×3) can control self-organization of adlayers into nanostructures with extremely different electronic and structural properties. Thus, it was established that at elevated temperature the R(15×3) superstructure controls the self-assembly of sub-monolayer amounts of Au into nm-wide nanostripes. Based on the results of core level photoemission, the R(15×3)-induced surface alloying which takes place between Au and W can be claimed as driving force of self-organization. The observed stripes exhibit a characteristic one-dimensional electronic structure with laterally quantized d-bands. Obviously, these are very important for applications, since dimensions of electronic devices have already stepped into the nm-range, where quantum-size phenomena must undoubtedly be considered.

Moreover, formation of perfectly uniform molecular clusters of C_{60} was demonstrated and described in terms of the van der Waals formalism. It is the first experimental observation of two-dimensional fullerene nanoclusters with "magic numbers". Calculations of the cluster potentials using the static approach have revealed characteristic minima in the interaction energy. They are achieved for 4 and 7 molecules per cluster. The obtained "magic numbers" and the corresponding cluster structures are fully consistent with the results of the STM measurements.

Bibliography

[1] N. W. Ashcroft, N. D. Mermin, *Solid State Physics*, Saunders, 1975.

[2] C. Kittel, *Introduction to Solid State Physics*, 7Wiley, 1996.

[3] W. A. Harisson, *Electronic Structure and the Properties of Solids: the Physics of the Chemical Bond*, Freeman, 1980.

[4] J. Singleton, *Band Theory and Electronic Properties of Solids*, Oxford, 2001.

[5] A. Messiah, *Quantum Machnaics*, Amsterdam : North Holland, 1962.

[6] A. R. West, *Basic Solid State Chemistry*, Wiley, 1999.

[7] V. L. Moruzzi, J. F. Janak, A. R. Williams, *Calculated Electronic properties of Metals*, New York, Pergamon, 1978.

[8] A. Hofmann, T. Ericson, P. Y. Landshoff (ed.), *The Physics of Synchrotron Radiation*, Cambridge, 2004.

[9] R. C. Jaklevic, J. Lambe, Phys. Rev. B 12, 4146 (1975).

[10] P. D. Loly, J. B. Pendry, J. Phys. C 16, 423 (1983).

[11] A. L. Wachs, A. P. Shapiro, T. C. Hseih, T.-C. Chiang, Phys. Rev. B 33, 1460, 1986.

[12] E. W. Plummer, R. Gomer (ed.), *Topics in Applied Physics*, v. 4, Springer, 1975.

[13] E. Beauripaire, F. Scheurer, G. Krill, J.-P. Kappler (Eds.), *Magnetism and Synchrotron Radiation*, Springer, 2001.

[14] S. E. Thompson, M. Armstrong, C. Auth et al., IEEE Transact. Elec. Dev. 51, 1790 (2004).

[15] T. Mizuno, N. Sugiyama, T. Tezuka, T. Numata, T. Maeda, S. Takagi, IEEE Transact. Elec. Dev. 51, 1114 (2004).

[16] Y. Takao, S. Nakai, N. Horiguchi, Fujitsu Sci. Tech, Journ. 39, 32 (2003).

[17] L. Vitali, M. G. Ramsey, F. P. Netzer, Phys. Rev. Lett. 83, 316 (1999).

[18] M. Hupalo, M. C. Tringides, Phys. Rev. B 65, 205406 (2002).

[19] H. H. Chang, M. Y. Lai, J. H. Wei, C. M. Wei, Y. L. Wang, Phys. Rev. Lett. 92, 066103 (2004) Magic clusters (In) on Si(111)-7x7

[20] S. Hüfner, *Photoelectron Spectroscopy: Principles and Applications*, Springer, 1995.

[21] S. D. Kevan (ed.), *Angle-Resolved Photoemission*, Elsevier, 1992.

[22] A. Liebsch and W. Gudat (ed.), *Synchrotronstrahlung in der Festkörperforschung*, Jülich, 1987.

[23] M. P. Seah, W. A. Dench, Surf. Interface. Anal. 1, 2 (1979).

[24] J. M. Ziman, *Electrons and Phonons: The Theory of Transport Phenomena in Solids*, Oxford, 2001.

[25] J. F. Watts, J. Wolstenholme, *An Introduction to Surface Analysis by XPS and AES*, Wiley, 2003.

[26] E. Burstein and Lundquist (ed.), *Tunneling Phenomena in Solids*, Plenum, 1969.

[27] G. Binnig, H. Rohrer, Helv. Phys. Acta 55, 726 (1982).

[28] G. Binnig, H. Rohrer, Ch. Gerber, E. Weibel, Phys. Rev. Lett. 49, 57 (1982).

[29] G. Binnig, H. Rohrer, Rev. Mod. Phys. 59, 615 (1987).

[30] R. Wiesendanger, *Scanning Probe Microscopy: Analytical Methods*, Springer, 1998.

[31] C. J. Chen, Phys. Rev. B 42, 8841 (1990).

[32] C. J. Chen, Phys. Rev. Lett. 65, 448 (1990).

[33] G. Binnig, H. Rohrer, IBM J. Res. Dev. 30, 355 (1986).

[34] J. Tersoff, D. R. Hamman, Phys. Rev. Lett. 50, 1998 (1983).

[35] J. Tersoff, D. R. Hamman, Phys. Rev. B 31, 805 (1985).

[36] J. Bardeen, Phys. Rev. Lett. 6, 57 9 (1961).

[37] N. D. Lang, Phys. Rev. Lett. 58, 45 (1987).

[38] V. M. Hallmark, S. Chiang, J. F. Rabolt, J. D. Swalen, R. J. Wilson, Phys. Rev. Lett. 59, 2879 (1987).

[39] G. Binnig, H. Rohrer, Ch. Gerber, E. Stoll, Surf. Sci. 144, 321, 1984.

[40] A. Selloni, P. Carnevali, E. Tossatti, C. D. Chen, Phys. Rev. B 31, 2602 (1985).

[41] R. M. Feenstra, A. J. A. Stroscio, J. Tersoff, A. P. Fein, Phys. Rev. Lett. 58, 1192 (1987).

[42] L. J. Clarke, *Surface Crystallography: An Introduction to Low Energy Electron Diffraction*, Wiley, 1985.

[43] L. L. Beranek, I. L. Vér, *Noise and Vibration Control Engineering*, Wiley, 1992.

[44] Internet page: www.bessy.de

[45] Internet page: www.elettra.trieste.it

[46] Omicron VT SPM User's Manual; Internet page: www.omicron.de

[47] Internet page: www.vacgen.com

[48] Newport I-2000 User's Manual; Internet page: www.newport.com

[49] P. Thiry, D. Chandesris, J. Lecante, C. Guillot, R. Pinchaux and Y. Pétroff, Phys. Rev. Lett. 43, 82 (1979).

[50] J. A. Knapp, F. J. Himpsel, D. E. Eastman, Phys. Rev. B 19, 4952 (1979).

[51] S. Hüfner, G. K. Wertheim, Phys. Rev. Lett. 35, 53 (1975).

[52] C. Guillot, Y. Ballu, J. Paigné, J. Lecante, K. P. Jain, P. Thiry, R. Pinchaux, Y. Pétroff, L. M. Falicov, Phys. Rev. Lett. 39, 1632 (1977).

[53] R. Clauberg, W. Gudat, E. Kisker, E. Kuhlmann, G. M. Rothberg, Phys. Rev. Lett. 47, 1314 (1981).

[54] S. Hüfner, G. K. Wertheim, N. V. Smith, M. M. Traum, Solid State Commun. 11, 323 (1972).

[55] D. E. Eastman, F. J. Himpsel, J. A. Knapp, Phys. Rev. Lett. 40, 1514 (1978).

[56] F. J. Himpsel, J. A. Knapp, D. E. Eastman, Phys. Rev. B 19, 2919 (1979).

[57] W. Eberhardt, E. W. Plummer, Phys. Rev. B 21, 3245 (1980).

[58] D. R. Penn, Phys. Rev. Lett. 42, 921 (1979).

[59] A. Liebsch, Phys. Rev. Lett. 43, 1431 (1979).

[60] L. C. Davis, L. A. Feldkamp, Solid State Commun. 43, 141 (1980).

[61] W. Nolting, W. Borgiel, V. Dose, and Th. Fauster, Phys. Rev. B 40, 5015 (1989).

[62] F. Aryasetiawan, Phys. Rev. B 46, 13051 (1992).

[63] N. Martensson, B. Johansson,Phys. Rev. Lett. 45, 482 (1980).

[64] M. Iwan, F. J. Himpsel, D. E. Eastman, Phys. Rev. Lett. 43, 1829 (1979).

[65] G. G. Tibbetts, W. F. Egelhoff, Jr., Phys. Rev. Lett. 41, 188 (1978).

[66] Y. Sakisaka, T. Komeda, M. Onchi, H. Kato, S. Masuda, K. Yagi, Phys. Rev. Lett. 58, 733 (1987).

[67] A. Kakizaki, J. Fujii, K. Shimada, A. Kamata, K. Ono, K.-H. Park, T. Kinoshita, T. Ishii, and H. Fukutani, Phys. Rev. Lett. 72, 2781 (1994).

[68] M. Weinelt, A. Nilsson, M. Magnuson, T. Wiell, N. Wassdahl, O. Karis, A. Fhlisch, and N. Martensson, J. Stöhr, M. Samant, Phys. Rev. Lett. 78, 967 (1997).

[69] L. A. Feldkamp, L. C. Davis, Phys. Rev. Lett. 43, 151 (1979).

[70] L. C. Davis, L. A. Feldkamp, Phys. Rev. Lett. 44, 673 (1980).

[71] R. H. Victora, L. M. Falicov, Phys. Rev. Lett. 55, 1140 (1985).

[72] M. Springer, F. Aryasetiawan, K. Karlsson, Phys. Rev. Lett. 80, 2389 (1998).

[73] V. N. Strokov, Phys. Stat. Sol. (b) 169, 115 (1992))

[74] M. A. Mueller, A. Samsavar, T. Miller, and T.-C. Chiang, Phys. Rev. B 40, 5845 (1989).

[75] L. Aballe, C. Rogero, P. Kratzer, S. Gokhale, and K. Horn,Phys. Rev. Lett. 87, 156801 (2001).

[76] I. Matsuda, T. Ohta, H. W. Yeom,Phys. Rev. B 65, 085327 (2002).

[77] T.-C. Chiang, Surf. Sci. Rep. 39, 181 (2000).

[78] T. Miller, A. Samsavar and T.-C. Chiang,Phys. Rev. B. 50, 17686 (1994).

[79] C. S. Wang, J. Callaway, Phys. Rev. B 15, 298 (1977).

[80] Landolt-Börnstein, Springer, www.landolt-boernstein.com

[81] A. M. Shikin, O. Rader, G. V. Prudnikova, V. K. Adamchuk, and W. Gudat, Phys. Rev. B 65, 075403 (2002).

[82] N. V. Smith, N. B. Brooks, Y.Chang and P. D. Johnson, Phys. Rev. B 49, 332 (1994).

[83] A. M. Shikin, O. Rader, G. V. Prudnikova, V. K. Adamchuk, W. Gudat, Phys. Low. Dim. Struct. 11, 61 (2001).

[84] S. I. Fedoseenko, I. E. Iossifov, S. A. Gorovikov, J.-S. Schmidt, R. Follath, S. L. Molodtsov, V. K. Adamchuk, and G. Kaindl, Nucl. Instr. Meth. Phys. Res. A 470, 84 (2001).

[85] S. A. Gorovikov, R. Follath, S. L. Molodtsov, and G. Kaindl, Nucl. Instr. Meth. Phys. Res. A 467-468, 565 (2001).

[86] N. V. Smith, Phys. Rev. B 32, 3549 (1985).

[87] M. Grüne, J. Peltzer, K. Wandelt, and I. J. Steinberger, J. Electron Spectrosc. Relat. Phenomen. 98-99, 121 (1999).

[88] J. Henk and B. Johanson, J. Electron Spectrosc. Relat. Phenomen. 105, 187 (1999).

[89] M. A. Müller, T. Miller, and T.-C. Chiang, Phys. Rev. B 41, 5214 (1990).

[90] C. Carbone, Private communication.

[91] T. Valla, P. Pervan, M. Milun, A. B. Hayden, and D. P. Woodruff, Phys. Rev. B 54, 11786 (1990).

[92] J. E. Ortega and F. J. Himpsel, Phys. Rev. Lett. 69, 844 (1992);

[93] A. M. Shikin, D. V. Vyalikh, G. V. Prudnikova, and V. K. Adamchuk, Surf. Sci. 487, 135 (2001).

[94] A. Zangwill, *Physics at Surfaces*, Cambridge, 1988.

[95] R. Notzel, Z. C. Niu, M. R. Ramsteiner, H. P. Schönherr, A. Tranpert, L. Däweritz, and K. H. Ploog, Nature (London) 392, 56 (1998).

[96] J. Hauschild, U. Gradmann, and H.-J. Elmers, Appl. Phys. Lett. 72, 3211 (1998).

[97] O. Pietzsch, A. Kubetzka, M. Bode, and R. Wiesendanger, Phys. Rev. Lett. 84, 5212 (2000).

[98] L. Bürgi, O. Jeandupeux, A. Hirstein, H. Brune, and K. Kern, Phys. Rev. Lett. 81, 5370 (1998).

[99] A. P. Shapiro, T. Miller, and T.-C. Chiang, Phys. Rev. B 38, 1779 (1988).

[100] X. Y. Wang, X. J. Shen, and R. M. Osgood, Jr., Phys. Rev. B 56, 7665 (1997).

[101] J. E. Ortega, S. Speller, A. R. Bachmann, A. Mascaraque, E. G. Michel, A. Närmann, A. Mugarza, A. Rubio, and F. J. Himpsel, Phys. Rev. Lett. 84, 6110 (2000).

[102] F. Baumberger, T. Greber, and J. Osterwalder, Phys. Rev. B 64, 195411 (2001).

[103] F. Baumberger, M. Hengsberger, M. Muntwiler, M. Shi, J. Krempasky, L. Patthey, J. Osterwalder, and T. Greber, Phys. Rev. Lett. 92, 16803 (2004).

[104] F. Baumberger, M. Hengsberger, M. Muntwiler, M. Shi, J. Krempasky, L. Patthey, J. Osterwalder, and T. Greber, Phys. Rev. Lett. 92, 196805 (2004).

[105] K. Ogawa, K. Nakanishi, and H. Namba, Solid State Commun. 125, 517 (2003).

[106] E. O. Kane, Phys. Rev. Lett. 12, 97 (1964).

[107] J. Anderson, G. J. Lapeyre, Phys. Rev. Lett. 36, 376 (1976).

[108] D. Westphal, A. Goldmann, Surf. Sci. 126, 253 (1983).

[109] N. E. Christensen and B. Feuerbacher, Phys. Rev. B 10, 2349 (1974).

[110] K. W. Kwak, M. Y. Chou, and N. Troullier, Phys. Rev. B 53, 13734 (1996).

[111] M. Henzler, Appl. Phys. 9, 11 (1976).

[112] M. Henzler, W. Göpel, Oberflächenphysik des Festkörpers, Teubner, Stuttgart (1991).

[113] J. J. Paggel, T. Miller, T.-C. Chiang, Science 283, 1709 (1999).

[114] D.-A. Luh, J. J. Paggel, T. Miller, and T.-C. Chiang, Phys. Rev. Lett. 84, 3410 (2000).

[115] S. J. Tang, L. Basile, T. Miller, T.-C. Chiang, Phys. Rev. Lett. 93, 216804 (2004).

[116] M. Kralj, M. Milun, P. Pervan, Surf. Sci. 557, 208 (2004).

[117] M. Milun, P. Pervan, B. Gumhalter, D. P. Woodruff, Phys. Rev. B 59, 5170 (1999).

[118] Eckhardt, L. Fritsche, J. Noffke, J. Phys. F: Met. Phys. 14, 97 (1984).

[119] T. Nautiyal, S. J. Youn, and K. S. Kim, Phys. Rev. B 68, 033407 (2003).

[120] D. W. Kim, H. Y. Lee, M. C. Yoo, G. Y. Yeom, App. Phys. Lett. 86, 052108 (2005).

[121] A. K. Petford-Long, D. J. Larson, A. Cerezo, X. Portier, P. Shang, D. Ozkaya, T. Long, P. H. Clifton, Microscopy and Microanalysis 10, 366 (2004).

[122] Adam Li, Feng Liu, D. Y. Petrovykh, J.-L. Lin, J. Viernow, F. J. Himpsel, and M. G. Lagally, Phys. Rev. Lett. 85, 5380 (2000).

[123] A. M. Shikin, A. Varykhalov, V. K. Adamchuk, A. Ionov, S. N. Bozko, W. Gudat and O. Rader, J. Elec. Spectr. Rel. Phen., *Proceeding of VUV-14*, accepted.

[124] A. M. Shikin, A. Varykhalov, S. A. Gorovikov, G. V. Prudnikova, V. K. Adamchuk, K.-H. Rieder, W. Gudat and O. Rader, J. Elec. Spectr. Rel. Phen., *Proceeding of VUV-14*, accepted.

[125] F. J. Himpsel, K. N. Altman, J. N. Krain, A. Kirakosian, J. L. Lin, A. Liebsch, J. Electr. Spec. Rel. Phenom. 126, 88 (2002).

[126] I. K. Robinson, P. A. Bennet, F. J. Himpsel, Phys. Rev. Lett. 88, 096104 (2002).

[127] F. J. Himpsel, J. L. McChesney, J. N. Crain, A. Kirakosian, V. Perez-Dieste, N. L. Abbott, Y. Y. Luck, P. F. Nealey, D. Y. Petrovykh, J. Phys. Chem B 108, 14484 (2004).

[128] J. L. McChesney, A. Kirakosian, R. Bennewitz, J. N. Crain, J. L. Lin, F. J. Himpsel, Nanotechnology 13, 545 (2002).

[129] J. N. Crain, A. Kirakosian, K. N. Altman, C. Bromberger, S. C. Erwin, J. L. McChesney, J. L. Lin, F. J. Himpsel, Phys. Rev. Lett. 90, 176805 (2003).

[130] J. N. Crain, J. L. McChesney, F. Zheng, M. C. Gallagher, P. C. Snijders, M. Bissen, C. Gundelach, S. C. Erwin, F. J. Himpsel, Phys. Rev. B 69, 125401 (2004).

[131] R. Bennewitz, J. N. Crain, A. Kirakosian, J. L. Lin, J. L. McChesney, D. Y. Petrovykh, F. J. Himpsel, Nanotechnology 13, 499 (2002).

[132] F. J. Himpsel, A. Kirakosian, J. N. Crain, J. L. Lin, D. Y. Petrovykh, Solid. State. Comm. 117, 149 (2001).

[133] F. J. Himpsel, K. N. Altmann, G. J. Mankey, J. E. Ortega and D. Y. Petrovykh, J. Magn. Magn. Mater. 200, 126 (1999).

[134] M. Pratzer, H. J. Elmers, Phys. Rev. B 67, 094416 (2003).

[135] X. Ma, H. L. Meyerheim, J. Barthel, J. Kirschner, S. Schmidt, E. Umbach, Appl. Phys. Lett. 84, 4038 (2004).

[136] P. O. Jubert, O. Fruchart, C. Meyer, J. Magn. Magn. Mater. 242, 565 (2002).

[137] G. Brown, H. K. Lee, T. C. Schulthess, B. Ujfalussy, G. M. Stocks, W. H. Butler, D. P. Landau, J. P. Pierce, J. Kirschner, J. Appl. Phys. 91, 7056 (2002).

[138] D. Q. Li, B. R. Cuenya, J. Pearson, S. D. Bader, W. Keune, Phys. Rev. B 64, 144410 (2001).

[139] P. Gambardella, A. Dallmeyer, K. Maiti, M. C. Malagoli, W. Eberhardt, K. Kern and C. Carbone, Nature 416, 301 (2002).

[140] M. Bode, A. Kubetzka, O. Pietzsch, R. Wiesendanger, Surf. Sci. 514, 135 (2002).

[141] D. M. Riffe, G. K. Wertheim, Surf. Sci. 399, 248 (1998).

[142] J. Gustafson, M. Borg, A. Mikkelsen, S. Gorovikov, E. Lundgren, and J. N. Andersen, Phys. Rev. Lett. 91, 056102 (2003).

[143] N. Sieber, Th. Seyller, L. Ley, D. James, J. D. Riley, R. C. G. Leckey, and M. Polcik, Phys. Rev. B 67, 205304 (2003).

[144] N. Sieber, Th. Seyller, R. Graupner, L. Ley, R. Mikalo, P. Hoffmann, D. R. Batchelor and D. Schmeisser App. Surf. Sci. 184, 278 (2001).

[145] W. Xu, J. B. Adams, T. L. Einstein, Phys. Rev. B 54, 2910 (1996).

[146] P. Elliot, *Constitution of binary Alloys*, McCrow-Hill, 1965.

[147] U. Bardi, Rep. Prog. Phys. 57, 939 (1994).

[148] H. Wolter, M. Schmidt, K. Wandelt, Surf. Sci. 298, 173 (1993).

[149] S. Esch, M. Hohage, Th. Michely, G. Cosma, Phys. Rev. Lett. 72, 518 (1994).

[150] M. Nohlen, M. Schmidt, K. Wandelt, Surf. Sci. 331-333, 902 (1995).

[151] K. Meinel, Ch. Ammer, M. Mitte, H. Wolter, H. Neddermeyer, Progr. Surf. Sci. 67, 183 (2001).

[152] R. X. Ynzunza, R. Denecke, F. J. Palomares, J. Morais, E. D. Tober, Z. Wang, F. J. G. de Abajo, J. Liesegang, Z. Hussain, M. A. Van Hove, C. S. Fadley, Surf. Sci. 459, 69 (2000).

[153] M. A. Van Hove and S. Y. Tong, Phys. Rev. Lett. 35, 1092 (1975).

[154] A. H. Cottrell, Mater. Sci. Techn., 11 , 209 (1995).

[155] L. H. Bennett, J. R. Cuthill, A. J. McAliste, N. E. Erickson, R. E. Watson, Science 184, 563 (1974).

[156] A. M. Shikin, O. Rader, W. Gudat, G. V. Prudnikova, V. K. Adamchuk, Surf. Rev. Lett. 9, 1375 (2002).

[157] D. V. Vyalikh, E. Weschke, Yu. S. Dedkov, G. Kaindl, A. M. Shikin, V. K. Adamchuk, Surface Science 540, L638 (2003)

[158] R. M. Stern, Appl. Phys. Lett. 5, 218 (1964).

[159] R. Baudoing, R. M. Stern, Surf. Sci. 10, 392 (1968).

[160] E. Bauer, Surf. Sci. 7, 351 (1967).

[161] E. D. Tober, R. X. Ynzunza, F. J. Palomares, Z. Wang, Z. Hussain, M. A. Van Hove, and C. S. Fadley, Phys. Rev. Lett. 79, 2085 (1997).

[162] W.-H. Soe, K.-H. Rieder, A. M. Shikin, V. Mozhaiskii, A. Varykhalov, and O. Rader, Phys. Rev. B 70, 115421 (2004).

[163] G. Doyen, D. Drakova, and M. Scheffler, Phys. Rev. B 47, 9778 (1993).

[164] R. H. Gaylord, and S. D. Kevan, Phys. Rev. B 36, 9337 (1987).

[165] J. Feydt, A. Elbe, H. Engelhard, G. Meister, Ch. Jung, A. Goldmann, Phys. Rev. B 58, 14007 (1998).

[166] T.-W. Pi, I.-H. Hong, and C.-P. Cheng, Phys. Rev. B 58, 4149 (1998)

[167] A. Mugarza, A. Mascaraque, V. Pérez-Dieste, V. Repain, S. Rousset, F. J. García de Abajo, J. E. Ortega, Phys. Rev. Lett. 87, 107601 (2001).

[168] A. Mugarza, A. Mascaraque, V. Repain, S. Rousset, K. N. Altmann, F. J. Himpsel, Yu. M. Koroteev, E. V. Chulkov, F. J. García de Abajo, and J. E. Ortega, Phys. Rev. B 66, 245419 (2002).

[169] J. E. Ortega, A. Mugarza, V. Repain, S. Rousset, V. Pérez-Dieste, and A. Mascaraque, Phys. Rev. B 65, 165413 (2002).

[170] A. M. Shikin, S. A. Gorovikov, V. K. Adamchuk, W. Gudat, and O. Rader, Phys. Rev. Lett. 90, 256803 (2003).

[171] A. M. Shikin, A. Varykhalov, G. V. Prudnikova, V. K. Adamchuk, W. Gudat, and O. Rader, Phys. Rev. Lett. 93, 146802 (2004).

[172] G. Hörmandinger and J. B. Pendry, Phys. Rev. B 50, 18607 (1994).

[173] B. R. Cooper, H. Ehrenreich, and H. R. Philipp, Phys. Rev. 138, A494 (1965).

[174] C. M. Fang, G. A. de Wijs and R. A. de Groot, J. Appl. Phys. 91, 8340 (2002).

[175] P. Segovia, D. Purdie, M. Hengsberger, and Y. Baer, Nature (London) 402, 504 (1999).

[176] R. Losio, K. N. Altmann, A. Kirakosian, J.-L. Lin, D.Y. Petrovykh, and F. J. Himpsel, Phys. Rev. Lett. 86, 4632 (2001).

[177] K. N. Altmann, J. N. Crain, A. Kirakosian, J.-L. Lin, D. Y. Petrovykh, and F. J. Himpsel, R. Losio, Phys. Rev. B. 64, 035406 (2001).

[178] J. R. Ahn, H.W. Yeom, H. S. Yoon and I.-W. Lyo, Phys. Rev. Lett. 91, 196403 (2003).

[179] C. Pampuch, O. Rader, T. Kachel, W. Gudat, C. Carbone, R. Kläsges, G. Bihlmayer, S. Blügel, and W. Eberhardt, Phys. Rev. Lett. 85, 2561 (2000).

[180] M. L. Hildner, K. E. Johnson, and R. J. Wilson, Surf. Sci. 388, 110 (1997).

[181] X. K. Shu, P. Jiang, and J. G. Che, Surf. Sci. 545, 199 (2003).

[182] A. Varykhalov et al., unpublished.

[183] M. Knupfer, Surface Science Reports 42, 1 (2001).

[184] H. W. Kroto, J. R. Heath, S. C. O'Brien, R. F. Curl, R. E. Smiley, Nature 318, 162 (1985).

[185] H. Prinzberg, A. Weiler, P. Landenberger, F. Wahl, J. Wörth, L. T. Scott, M. Gelmont, D. Olevano, B. v. Issendorrf, Nature 407, 60 (2000).

[186] S. Saito and A. Oshiyama, Phys. Rev. Lett. 66, 2637 (1991).

[187] T. R. Ohno, Y. Chen, S. E. Harvey, G. H. Kroll, J. H. Weaver, R. E. Haufler, R. E. Smalley, Phys. Rev. B. 44, 13747 (1991).

[188] P. A. Heiney, J. A. Fischer, A. R. McGhie, W. J. Romanov, A. M. Denenstein, J. P. McCauley, A. B. Smith, D. E. Cox, Phys. Rev. Lett. 66, 2911 (1991).

[189] P. J. Benning, C. G. Olson, D. W. Lynch, J. H. Weaver, Phys. Rev. B 50, 11239 (1994).

[190] R. C. Haddon, A. F. Hebard, M. J. Rosseinsky, D. W. Murphy, S. J. Duclos, K. B. Lyons, B. Miller, J. M. Rosamilia, R. M. Fleming, A. R. Kortan, S. H. Glarum, A. V. Makhija, A. J. Muller, R. H. Eick, S. M. Zahurak, R. Tycko, G. Dabbagh and F. A. Thiel, Nature 350, 320 (1991).

[191] A. F. Hebard, M. J. Rosseinsky, R. C. Haddon, D. W. Murphy, S. H. Glarum, T. T. M. Palstra, A. P. Ramirez and A. R. Kortan, Nature 350, 600, (1991).

[192] K. Tanigaki, T. W. Ebbesen, S. Saito, J. Mizuki, J. S. Tsai, Y. Kubo and S. Kuroshima, Nature 352, 222 (1991).

[193] T. L. Makarova, B. Sundquist, R. Höhne, P. Esquinazi, Y. Kopelevich, P. Scharf, V. A. Davydov, L. S. Kashevarova, A. V. Rakhmanina, Nature 413, 716 (2001).

[194] J. P. Long, S. J. Chase, M. N. Kabler, Chem. Phys. Lett. 347, 29 (2001).

[195] B. S. Itchkawitz, J. P. Long, T. Schedelniedrig, M. N. Kabler, A. M. Bradshaw, R. Schlogl, W. R. Hunter, Chem. Phys. Lett. 243, 211 (1995).

[196] B. Narymbetov, V. Agafonov, V. A. Davydov, L. S. Kashevarova, A. V. Rakhmanina, A. V. Dzyabchenko, V. I. Kulakov, Rene Ceolin, Chem. Phys. Lett. 367, 157 (2003).

[197] S. Iijima, Nature 354, 56 (1991)

[198] B. Bourlon, C. Miko, L. Forro , D.C. Glattli, and A. Bachtold, Phys. Rev. Lett. 93, 176806 (2004).

[199] R. Martel, T. Schmidt, H. R. Shea, T. Hertel and Ph. Avouris, Appl. Phys. Lett. 73, 2447 (1998).

[200] Ph. Avouris, T. Hertel, R. Martel, T. Schmidt, H. R. Shea and R. E. Walkup, Appl. Surf. Sci. 141, 201 (1998).

[201] S.-B. Lee, K. B. K. Teo, G. A. J. Amaratunga, W. I. Milne, M. Chhowalla, D. G. Hasko and H. Ahmed, J. Vac. Sci. Tech. B, 21, 996 (2003).

[202] V. Derycke, R. Martel, J. Appenzeller, Ph. Avouris, Nano Lett. 1, 453 (2001).

[203] P. M. Albrecht, Proceedings of the International Vacuum Congress IVC-16/ICSS-12/NANO-8/AIV-17, Venice, Italy (2004).

[204] M. Sakai, M. Ichida, A. Nakamura, Fuller. Sci. Tech. 9, 351 (2001).

[205] V. M. Mikushkin, V. V. Shnitov, Phys. Solid State 39, 164 (1997).

[206] J. H. Weaver, J. L. Martins, T. Komeda, Y. Chen, T. R. Ohno, G. H. Kroll, and N. Troullier, Phys. Rev. Lett. 66, 1741 (1991).

[207] R. Saito, G. Dresselhaus, M. S. Dresselhaus, Phys. Rev. B 46, 9906 (1992).

[208] G. K. Wertheim, D. N. E. Buchanan, Solid State Comm. 88, 97 (1993).

[209] S. Suto, K. Sakamoto, D. Kondo, T. Wakita, A. Kimura, A. Kakizaki, C.-W. Hu, A. Kasuya, Surf. Sci. 438, 242 (1999).

[210] J. García-Rideja, C. Rey, L. J. Galleo, Phys. Rev. B 56, 6466 (1997).

[211] C. Rey, J. García-Rodeja, L. J. Gallego, Z. Phys. D 40, 395 (1997).

[212] L. J. Galleo, J. García-Rodeja, M. M. G. Alemany, C. Rey, Phys. Rev. Lett. 83, 5258 (1999),

[213] T. P. Martin, U. Näher, H. Schaber, U. Zimmermann, Phys. Rev. Lett. 70, 3079 (1993).

[214] L. A. Girifalco, J. Phys. Chem. 96, 858 (1992).

[215] J. Jellinek, T. L. Beck, R. S. Berry, J. Chem. Phys. 84, 2783 (1986).

[216] H. Rafii-Tabar, G. A. Mansoori, H. S. Nalwa (ed.), *Encyclopedia of Nanoscience and Nanotechnology*, v. 1, American Scientific, 2004.

[217] H. Rafii-Tabar, K. Ghafoori-Tabrizi, Prog. Surf. Sci. 67, 217 (2001).

[218] Ch. Girard, Ph. Lambin, A. Dereux, A. A. Lucas, Phys. Rev. B 49, 11425 (1994).

[219] R. Brühl, R. Guardiola, A. Kalinin, O. Kornilov, J. Navarro, T. Savas, J. P. Toennies, Phys. Rev. Lett. 92, 185301 (2004).

[220] S.-C. Li, J.-F. Jia, R.-F. Dou, Q.-K. Xue, I. G. Batyrev, S. B. Zhang, Phys. Rev. Lett. 93, 116103 (2004).

[221] J.-L. Li, J.-F. Jia, X.-J. Liang, X. Liu, J.-Z. Wang, Q.-K. Xue, Z.-Q. Li, J. S. Tse, Z. Zhang, S. B. Zhang, Phys. Rev. Lett. 88, 066101 (2002).

[222] F. H. Stillinger, T. A. Weber, Phys. Rev. A 25, 978 (1982).

[223] S. Gwo, C. K. Shih, Phys. Rev. B 47, 13059 (1993).

[224] M. Bode, R. Pascal, R. Wiesendanger, Surf. Sci. 344, 185 (1995),

[225] M. Bode, R. Pascal, R. Wiesendanger, Z. Phys. B. Cond. Matt. 101, 103 (1996).

[226] M. Bode, R. Pascal, R. Wiesendanger, Z. Phys. B. Cond. Matt., 99, 143 (1996).

[227] L. H. Bennet, J .R. Cuthill, A. J. McAlister, N. E. Erickson, and R. E. Watson, Science 184, 563 (1974).

[228] R. J. Colton and J. W. Rabalais, Inorg. Chem. 15, 136 (1976).

[229] K. L. Håkansson, H. I. P. Johansson, L. J. Johansson, Phys. Rev. B 49, 2035 (1994).

[230] A. Varykhalov et. al, "Quantum-size effect is a surface carbide: W(110)/C-R(15×3)", submitted.

[231] A. Varykhalov et al., "Self-organization of one-dimensional Au nanowires on a surface carbide and lateral electron quantization", submitted.

[232] Inger Ekvall, Erik Wahlström, Dan Claesson, Hakan Olin, and Eva Olsson, Meas. Sci. Technol. 10, 11 (1999).

[233] A. Varykhalov et al., "Simulation of the tip-molecule interaction for C_{60} on weakly supporting substrate", to be published.

[234] X. Yao, T. G. Ruskell, R. Workman, D. Sarid, D. Chen, Surf. Sci. 366, L743 (1996).

[235] R. Follath R, F. Senf F, W. Gudat W, J. Synch. Rad. 5, 769 (1998).

[236] K. J. S. Sawhney, F. Senf F, M. Scheer, F. Schafers, J. Bahrdt, A. Gaupp, W. Gudat W, Nucl. Instr. Meth. Phys. 390, 395 (1997).

[237] G. Costantini, S. Rusponi, E. Giudice, C. Boragno, U. Valbusa, Carbon 37, 727 (1999).

[238] E. Giudice, E. Magnano, S. Rusponi, C. Boragno, U. Valbusa, Surf. Sci. 405, L561 (1998).

[239] Young Kuk, D. K. Kim, Y. D. Suh, K. H. Park, H. P. Noh, S. J. Oh and S. K. Kim, Phys. Rev. Lett. 70, 1948 (1993).

[240] M. R. C. Hunt, S. Modesti, P. Rudolf, R. E. Palmer, Phys. Rev. B 51, 10039 (1995).

[241] Amy Y. Liu, Renata M. Wentzcovitch, and Marvil L. Cohen, Phys. Rev. B. 38, 9483 (1988).

[242] P. M. Stefan, M. L. Shek, I. Lindau, W. E. Spicer, L. I. Johansson, F. Herman, R. V. Kasowski, G. Brogen, Phys. Rev. B 29, 5423 (1984).

[243] L. F. Mattheiss and D. R. Hamann, Phys. Rev. B. 30, 1731 (1984).

[244] P. R. Antoniewicz, Surf. Sci. 52, 703 (1975).

[245] P. R. Antoniewicz, Phys. Rev. Lett. 32, 1424 (1974).

[246] P. A. Gravil, Ph. Lambin, G. Gensterblum, L. Henrard, P. Senet, A. A. Lucas, Surf. Sci. 329, 199 (1995).

[247] The most adequate description of the core level line shape is obtained by convoluting Gaussian and Lorentzian contributions. This convolution is called Voigt profile and defined as follows:

$$(4.7) \qquad f(E) = f(L \cdot G) = \int_{-\infty}^{+\infty} L(E') \cdot G(E - E')dE'$$

Application of Voigt functions is desired if the resolution is sufficient to derive physically meaningful peak shape parameters. Contribution of the Gaussian is especially important since it represents the instrumental part of the resolution.

Typical values of FWHM Δ_L (Lorentzian) and FWHM Δ_G (Gaussian) used in this work for deconvolution of $W4f_{\frac{7}{2}}$ and $Au4f_{\frac{7}{2}}$ spectra were Δ_L=0.05–0.10 eV and Δ_G=0.15–0.20 eV. In all cases the asymmetry (Doniach-Sunjic line shape) was found negligible and the corresponding parameter was neglected.

Publication List

Refereed Papers

1. A. M. Shikin, A. Varykhalov, G. V. Prudnikova, V. K. Adamchuk, W. Gudat, and O. Rader, "Photoemission from Stepped W(110): Initial or Final State Effect? ", Phys. Rev. Lett. 93, 146802 (2004).

2. W.-H. Soe, K.-H. Rieder, A. M. Shikin, V. Mozhaiskii, A. Varykhalov, and O. Rader, "Surface phonon and valence band dispersions in graphite overlayers formed by solid-state graphitization of 6H-SiC(0001) ", Phys. Rev. B 70, 115421 (2004).

3. A. M. Shikin, A. Varykhalov, V. K. Adamchuk, A. Ionov, S. N. Bozko, W. Gudat and O. Rader, "Quantum-well states and lateral superlattice effect in Ag and Au stripes on stepped W(145)", Proceedings VUV-14, J. Electron. Spectrosc. Relat. Phenom. 144-147, 341 (2005).

4. A. M. Shikin, A. Varykhalov, S. A. Gorovikov, G. V. Prudnikova, V. K. Adamchuk, K.-H. Rieder, W. Gudat and O. Rader, "Photoemission from surface-localized structures on vicinal surfaces: Initial- or final-state superlattice effect?", Proceedings VUV-14, J. Electron. Spectrosc. Relat. Phenom. 144-147, 625 (2005).

5. A. Yu. Varykhalov, M. V. Kuzmin, M. A. Mitsev, "Electronic structure and elemental composition of thin films of Europium deposited at room temperature on a Si(110)-2×1 surface", Techn. Phys. Lett. 31, 13 (2005).

6. V. A. Mozhayskiy, A. Yu. Varykhalov, A. G. Starodubov, A. M. Shikin, S. I. Fedoseenko, V. K. Adamchuk, "Two alternative ways for formation of mono-atomic carbon layer on Ni(111): Organic-gas cracking and thermal decomposition of fullerenes in thin film", Fullerenes, Nanotubes and Carbon Nanostructures 12, 385 (2004).

7. A. Varykhalov, O. Rader and W. Gudat, "Self-organization of one-dimensional Au nanowires on a surface carbide and lateral electron quantization", (submitted to Appl. Phys. Lett.)

8. A. Varykhalov, O. Rader and W. Gudat, "Structure and quantum-size effects in a surface carbide: W(110)/C-R(15×3)", (in press Phys. Rev. B)

9. A. Varykhalov, A. M. Shikin, W. Gudat, P. Moras, C. Grazioli, C. Carbone and O. Rader, "Probing the ground state electronic structure of a correlated electron system by quantum well states: Ag/Ni(111)", (submitted to Phys. Rev. Lett.)

Conferences

1. A. Varykhalov, O. Rader, W. Gudat, "Temperature-induced self-organization of metallic nanostructures on W(110)/C-R(15×3), IVC-16 / ICSS-12 / NANO-8 / AIV-17, Venice, 2004 [Poster].

2. A. Varykhalov, O. Rader, C. Di Giacomo, A. M. Shikin, W. Gudat, C. Grazioli and C. Carbone, "Behavior of quantum-well and surface states of Ag/Ni(111)" DPG Frühjahrstagung, Regensburg, 2004 [Talk].

3. A. Varykhalov, O. Rader and W. Gudat, "Self-organization of Au-nanowires on two-dimensional tungsten carbide" DPG Frühjahrstagung, Regensburg, 2004 [Talk].

4. A. Varykhalov, A. M. Shikin, G. V. Prudnikova, V. Mojaiskii, W. Gudat, and O. Rader, "Superlattice effects in angle-resolved photoemission from stepped W(331)", DPG Frühjahrstagung, Dresden, 2003 [Talk].

5. A. Varykhalov, A. M. Shikin, O. Rader, W. Gudat, A. Loza, M. Poigine, V. K. Adamchuk, and D. Vyalikh, "Stepped epitaxial graphite by transformation of vicinal SiC(0001)", DPG Frühjahrstagung, Dresden, 2003 [Talk].

Brief Reports

1. A. Varykhalov, O. Rader, V. K. Adamchuk, W. Gudat, "Magic numbers in self-assembled two-dimensional nanoclusters of C_{60}", BESSY Annual Report, 2004.

2. A. Varykhalov, O. Rader, W. Gudat, "Quantum-size effects in a surface carbide: W(110)/C-R(15×3)", BESSY Annual Report, 2004.

3. Th. Seyller, K. V. Emtsev, K. Gao, F. Speck, L. Ley, A. Tadich, L. Broekman, J. D. Reiley, R. C. G. Leckey, O. Rader, A. Varykhalov, A. M. Shikin, "Electron spectroscopy of graphite layers grown on SiC(0001) surfaces", BESSY Annual Report, 2004.

4. M. Veronese, P. Moras, P. Gambardella, H. Brune, O. Rader, A. Varykhalov, A. Vollmer, S. Gardonio, C. Carbone, "Photoemission of isolated V atoms on alkali surfaces", BESSY Annual Report, 2004.

5. A. Varykhalov, O. Rader, W. Gudat, "Self-assembled Au nanowires on two-dimensional surface carbide: W(110)/C-R(15×3)", BESSY Annual Report, 2003.

6. D. V. Buturovich, M. V. Kuzmin, M. A. Mitsev, A. Varykhalov, "Growth mechanism and electronic structure of Eu-Si(100) interface at various stages of its formation", BESSY Annual Report, 2003.

7. A. Shikin, O. Rader, A. Varykhalov, W. Gudat, "Quantum well states in Ag-stripes on stepped W(145)", BESSY Annual Report, 2003.

8. A. M. Shikin, A. Varykhalov, G. V. Prudnikova, V. Mozhaiskii, W. Gudat, O. Rader, "Valence band umklapp at the step superlattice of W(331)", BESSY Annual Report, 2002.

9. A. Varykhalov, A. M. Shikin, O. Rader, W. Gudat, A. Loza, M. Poiguine, V. K. Adamchuk, D. Vyalikh, "Stepped epitaxial graphite by transformation of vicinal SiC(0001)", BESSY Annual Report, 2002.

10. A. M. Shikin, O. Rader, A. Varykhalov, V. Mozhaiskii, G. V. Prudnikova, V. Adamchuk, and W. Gudat, "Effects of lateral quantization in a step-decoration system: Au/W(331)", BESSY Annual Report, 2001.

Curriculum Vitae

Name:	Andrei Varykhalov
Date of birth:	20 Jan. 1978
Place of birth:	Saint-Petersburg (Leningrad).
Mother:	Raisa Varykhalova, born 5 Mar. 1947
	in Saint-Petersburg (Leningrad)
Farther:	- - -
Address:	c/o BESSY G.m.b.H., Albert-Einstein-Str. 15,
	D-12489, Berlin
Sep. 1985 – May 1991	Public School of St.Petersburg, Nr. 190
Sep. 1991 – May 1993	Public School of St.Petersburg, Nr. 193
Sep. 1993 – May 1995	Phys.-Math. Lyceum (School Nr. 239)
May 1995	High-school exams
Sep. 1995 – Jun. 1997	St.-Petersburg State Institute of Fine Mechanics and Optics (Technical University), Faculty of Computer Science
Sep. 1995 – Jun. 2001	St.-Petersburg State University, Faculty of Physics
Jun. 1999	Bachelor degree in physics (w. Honor) at St.-Petersburg State University in the group of Prof. V. K. Adamchuk. Thesis: "Computer simulation of electron diffraction phenomena"
Jun. 2001	Master degree in physics (w. Honor) at St.-Petersburg State University in the group of Prof. V. K. Adamchuk. Thesis: "STM investigation of graphite based composites"
Sep. 1996 – Sep. 2001	Work at St.-Petersburg State Educational Center "Anichkov Palace". Teaching activities: lectures on Computer Science for students
Since Oct. 2001	Ph. D. Student of Prof. W. Gudat at Berliner Elektronenspeicherring -Gesellschaft für Synchrotronstrahlung m.b.H. (BESSY) and Universität Potsdam

Zusammenfassung

Die aktuelle Doktorarbeit ist auf die Eigenschaften von selbst-organisierten Nanostrukturen fokussiert. Die strukturellen und elektronischen Eigenschaften von verschiedenen Systemen wurden mit den Methoden Elektronenbeugung, Rastertunnelmikroskopie und Photoelektronenspektroskopie untersucht. Insbesondere wurde die für die Rastertunnelmikroskopie in situ präparierter Proben eingesetzte Apparatur im Rahmen dieser Arbeit konstruiert und aufgebaut. Einzelheiten hierzu sind im experimentellen Kapitel zu finden.

Der wissenschftliche Teil beginnt mit Untersuchungen von Quantentrogeffekten in der elektronischen Struktur einer Ag-Schicht auf Ni(111)-Substrat. Charakteristische Quantentrogzustände im Ag-sp-Band wurden in Photoelektronenspektren beobachtet. Die Analyse von schichtdicken- und winkelab-hängiger Photoemission hat neue und wesentliche Informationen über die Eigenschaften des Ag/Ni-Systems geliefert. Insbesondere konnte zum ersten Mal eine relative Bandlücke im Ni-Substrat durch das Verhalten der Quantentrogzustände indirekt vermessen werden. Das ist für Ni besonders wichtig, weil es sich bei Ni um ein stark korreliertes Elektronensystem handelt. Die Ergebnisse wurden mit Rechnungen auf der Basis des erweiterten Phasenmodelles verglichen. Der Vergleich ergibt eine Bandlücke, die sehr gut mit ab-initio-Rechnungen auf Basis der lokalen Elektronendichte-Nährung überein-stimmen. Dennoch widersprechen die Daten der Ni-Bandstruktur, die direkt mit Photoemission gemessen wird. Diese Kontroverse zeigt deutlich, daß der Unterschied zwischen Theorie und Experiment Korrelationeffekten im Endzustand der Photoemission zugeordnet werden kann.

Des weiteren wurden Nanosysteme von noch niedrigerer Dimensionalität untersucht. Gestufte Oberflächen W(331) und W(551) wurden als ein-dimensionale Modellsysteme für die Selbstorganisation von Au-Nanoclustern benutzt. Photonenenergieabhängige Photoemission hat eine neue Oberflächen-resonanz aufgedeckt, die auf der Basisebene der Terrassen dieser Systeme auftritt. Die Dispersion E(k) von diesem Zustand, die mit winkelaufge-löster Photoemission vermessen wurde, zeigt deutlich die Einwirkung von Umklapp-Effekten. Diese zeigen sich als zwei Parabeln, die relativ zu der Terrassennormale symmetrisch um die Hälfte der Oberflächen-Brillouinzone verschoben sind. Die erzielten Ergebnisse sind sehr wichtig für das Verständnis der elektronischen Eigenschaften von eindimensionalen Nanostrukturen.

Außerdem wurde gezeigt, daß W(331) und W(551) als Vorlage für selbstorganisierte metallische Nanostrukturen dienen können. Eine kombinierte Untersuchung von strukturellen und elektronischen Eigenschaften von unter-monolagen Mengen von Au auf diesen Substraten wurde durchgeführt. Es hat sich gezeigt, daß Au mit dem Substrat an der Oberfläche legieren kann, wenn die Oberfläche ein wenig oxidiert und die Temperatur erhört ist. Als Folge formiert sich auf den Stufen eine Nanostruktur von gleichen (aber nicht regelmässig verteilten) Nanoclustern aus dieser Au-W Legierung. Diese Oberflächenlegierung bildet ein neuartiges sp-Band in der Nähe der Fermi-Kante. Zudem spaltet dieser neue elektronische Zustand

in konstante Energieniveaus auf. Das beobachtete Phänomen wird als laterale Quantisierung interpretiert.

Das letzte Kapitel dieser Doktorarbeit bildet auch den Hauptteil. Es handelt von Selbstorganisierungsphänomenen auf einer Oberflächenrekonstruktion und den Eigenschaften von so hergestellten Nanostrukturen. Das zweidimensionale Oberflächen-Karbid W(110)/C-R(15×3) wurde intensiv untersucht. Beobachtete Quantentrogeffekte in der Photoemission in Kombination mit den Ergebnissen der Rastertunnelmikroskopuntersuchungen führen zu einem verbesserten Strukturmodell für das Oberflächenkarbid.

Es wurde auch gezeigt, daß W(110)/C-R(15×3) die Selbstorganisierung von Nanostrukturen mit sehr verschiedenen elektronischen und strukturellen Eigenschaften steuern kann. Es wurde gefunden, daß bei erhöhter Temperatur die R(15×3)-Überstruktur die Bildung von Nanostreifen aus unter-monolagiger Au Bedeckung, von denen jede 1 nm breit ist, kontrolliert. Die hergestellten Nanostreifen besitzen eine charakteristische eindimensionale elektronische Struktur mit lateral quantisierten d-Bändern. Basierend auf der Photoemission von Rumpfniveaus wird eine Kohlenstoff-induzierte Ober-flächenlegierung zwischen Au und W als Grund für die beobachtete Organisierung vorgeschlagen. Solche Phänomene sind sehr wichtig für Anwendungen, seit die Mikroelektronik in den nm-Maßstab eingetreten ist, in welchem mit Quantentrogeffekten zu rechnen ist.

Zusätzlich wurde die Bildung von perfekt uniformen molekularen Nanoclustern von C_{60} auf W(110)/C-R(15×3) demonstriert. Dieses Phänomen kann im van-der-Waals Formalismus beschrieben werden. Die berichteten Ergebnisse sind eine erstmalige experimentelle Beobachtung von zweidimensionalen Fulleren-Nanoclustern mit magischen Zahlen. Berechnungen der Clusterpotentiale in der statischen Näherung im Girifalco-Modell zeigen Minima der Wechselwirkungsenergie für Cluster aus 4 und 7 C_{60}-Molekülen. Diese magischen Zahlen sowie die entsprechenden Clusterkonfigurationen sind vollkommen konsistent mit den Ergebnissen des STM-Experiments.

Acknowledgements